

Thin-Film PZT Scanning Micro-actuators for Vertical Cross-sectional Imaging in Endomicroscopy

by

Jongsoo Choi

A dissertation submitted in partial fulfillment
of the requirements for the degree of
Doctor of Philosophy
(Mechanical Engineering)
in the University of Michigan
2017

Doctoral Committee:

Associate Professor Kenn R. Oldham, Chair
Professor Diann Brei
Professor Yogesh Gianchandani
Professor Karl Grosh

Copyright © 2017 by Jongsoo Choi

To my family for their boundless love and support.

ACKNOWLEDGEMENTS

When I first came to Michigan in 2007 from Korea for my undergraduate studies, I think I even didn't know what to expect, as I had never been to the US before. I certainly didn't know I would stay at Michigan this long, but my more than nine years in Ann Arbor has been life-changing. I'm grateful for all the learning experience, opportunities that led me to grow, and people that I have developed relationships with during my time here in Ann Arbor. I would like to take this space to thank many who helped me along this journey.

First, I would like to thank my advisor, Dr. Kenn Oldham, for his considerable guidance and support over the past eight years. I have been fortunate to have an opportunity to work with him from my undergraduate years. He provided an environment for me to comfortably learn and explore different things, and gave me many opportunities to teach and present my work, from which I benefited much. I also thank Professor Diann Brei, Professor Yogesh Gianchandani, and Professor Karl Grosh for serving on my dissertation committee and giving me valuable feedback on this dissertation work.

I thank Professor Thomas Wang and his research group for their excellent collaboration. Especially, I'm grateful for the friendships that I have with Dr. Zhen Qiu, Xiyu Duan, and Dr. Haijun Li. I also appreciate my lab mates, Dr. Chris (Choong-ho) Rhee, Dr. Jeong hoon Ryou, Jinhong Qu, Yi Chen, Kendall Teichert, Lu Wang, and Mayur, as well as Chuming Zhao from Professor Grosh's group. Helpful academic discussions with them as well as many fun ones made my PhD work

easier and more enjoyable. I particularly thank Dr. Chris Rhee for training and helping me with microfabrication processes.

I acknowledge the support from the staff from Lurie Nanofabrication Facility as well as fellow researchers at LNF. Their advice and help tremendously helped the microfabrication in this dissertation. I also acknowledge the National Institute of Health and National Science Foundation for providing financial support for this work.

I would like to express my gratitude to Dr. Judy Dyer who helped me with my writing during my first several years at Michigan. She supported me throughout this whole journey, and writing skills I learned from her helped me greatly during my graduate studies.

I also thank Harvest Mission Community Church, my church community here in Ann Arbor, for being a place of love and support for me for the past nine years. Especially, I'm very grateful for the brothers and sisters in the graduate student group, Impact, with whom I shared my life. I really enjoyed studying, eating, sharing, praying, and playing with them.

I'm so much thankful for my family, my mom and dad, and my brother and sister-in-law. Their endless and unconditional love and support have made me who and where I am now and immensely helped me finish this dissertation work. I would also like to thank Tammy and Phil Yi for their encouragement and prayers for me and my family.

Lastly, I praise and honor the Creator God, who made heaven and earth and everything in them through Jesus Christ and sustains all things by marvelous physical laws, for giving me this amazing experience and helping me through all.

TABLE OF CONTENTS

DEDICATION.....	ii
ACKNOWLEDGEMENTS.....	iii
LIST OF FIGURES.....	viii
LIST OF TABLES.....	xiv
LIST OF APPENDICES.....	xv
ABSTRACT.....	xvi
CHAPTER 1: INTRODUCTION.....	1
1. 1. Motivation.....	1
1. 1. 1. Need for In Vivo Vertical Cross-sectional Imaging.....	1
1. 1. 2. Optical Endomicroscopy for In Vivo Vertical Cross-sectional Imaging.....	3
1. 1. 3. Miniature Scanning Mechanisms for Endomicroscopy.....	10
1. 1. 4. Actuator Specifications Needed for Real-time Vertical Sectioning in Endomicroscopy.....	13
1. 2. Existing Actuator Technologies.....	15
1. 3. Piezoelectricity.....	17
1. 4. Research Goals and Thesis Overview.....	22
1. 5. References.....	24
CHAPTER 2: FIRST GENERATION PIEZOELECTRIC ACTUATOR.....	32

2. 2. Actuator Design and Static Modeling	32
2. 2. 1. Actuator Geometry and Working Principle.....	32
2. 2. 2. Static Modeling for Design	34
2. 2. 3. Design Trade-off Analysis.....	42
2. 3. Fabrication	47
2. 4. Performance Characterization	50
2. 4. 1. Characterization of Non-Differential-Drive Scanners	50
2. 4. 2. Characterization of Differential-Drive Scanners	52
2. 5. Imaging Using Low Frequency Actuation.....	55
2. 5. 1. Reflectance Mode Remote Scan	56
2. 5. 2. Two Photon Imaging	58
2. 6. Summary	60
2. 7. References.....	61
CHAPTER 3: SECOND GENERATION PIEZOELECTRIC ACTUATOR	63
3. 1. Problems with 1 st Generation Devices.....	63
3. 1. 1. Delamination of Gold Layer	63
3. 1. 2. Over-etching of Frame	65
3. 1. 3. Failure of SiO ₂ Encapsulation	68
3. 1. 4. Non-uniform XeF ₂ Etching Due to Teflon.....	70
3. 1. 5. Varying Outcome of Buried SiO ₂ Layer.....	71
3. 2. New Fabrication Process.....	72
3. 3. Device Characterization	82
3. 3. 1. DC Actuation	82
3. 3. 2. Isolation of Pure Vertical Motion Near Resonance	84

3. 4. Imaging Using Dynamic Balancing	87
3. 4. 1. 2 nd Generation Actuator	87
3. 4. 2. 1 st Generation Actuator with Attached Mirror	90
3. 5. Summary	92
3. 6. Reference	93
CHAPTER 4: MODELING	94
4. 1. Calibrated Static and Transient Model	94
4. 1. 1. Background	94
4. 1. 2. Model perturbation	97
4. 1. 3. Parameter fitting results	103
4. 1. 4. Summary	111
4. 2. Dynamics Over Large Vertical Stroke.....	112
4. 2. 1. Background	112
4. 2. 2. Modeling of Multi-Axis Motion of Stage.....	115
4. 2. 3. Simulation Studies.....	124
4. 2. 4. Comparison with Experimental Results	126
4. 2. 5. Summary	129
4. 3. References.....	130
CHAPTER 5: CONCLUSIONS & FUTURE WORK	134
5. 1. Summary	134
5. 2. Contributions	135
5. 3. Future Work	137
APPENDICES	141

LIST OF FIGURES

Figure 1.1. Progression from normal mucosa of hallow organs to carcinoma [1.4]	2
Figure 1.2. Left: conventional single axis confocal configuration; Right: dual axes confocal configuration [1.7]	5
Figure 1.3. Scanning geometries (left: pre-objective scanning, right: post-objective scanning) [1.4]	6
Figure 1.4. Vertical cross sectional image of colonic dysplasia (top: targeted imaging with Cy5.5 labeled peptide, down: corresponding histology stained with H&E) [1.13]	7
Figure 1.5. Left: photograph of handheld dual axes system with bulky PZT based PI actuator (circled) used in [1.13] (Photo credit: Dr. Zhen Qiu), Right: therapeutic endoscope.....	7
Figure 1.6. Schematic diagram of optical coherence tomography system [1.14]	8
Figure 1.7. Schematic of a time domain OCT system based on a Michelson interferometer [1.31]	12
Figure 1.8. Schematic of miniaturized scanning probe based on dual axes confocal microscopy	13
Figure 1.9. Crystal structure for a piezoelectric ceramic: (1) cubic above Curie temperature; (2) tetragonal below Curie temperature [1.53]	18
Figure 1.10. Externally and internally leveraged bulk piezoelectric actuator structures, figures from [1.70, 1.71]	21
Figure 1.11. Schematics of cross-section of thin-film piezoelectric unimorph (a), bimorph with common electrode in the middle (b), bimorph with elastic layer (c).....	22
Figure 1.12. Cross-sectional schematics of d_{31} actuation mode (a) and d_{33} actuation mode (b)	22

Figure 2.1. Left: piezoelectrically actuated vertical stage (top view); Right: schematic cross-section of a vertical translational stage [2.1]	33
Figure 2.2. Proposed 3DOF micro-scanner design (actuatable directions in blue font)	34
Figure 2.3. Schematic drawing of a unimorph bending in an S-shape	34
Figure 2.4. Notation for Beams and Legs.....	35
Figure 2.5. Free body diagram of Beam 1.....	36
Figure 2.6. Free body diagram of a Leg.....	38
Figure 2.7 Free body diagram of the stage.....	39
Figure 2.8. Definitions of angles and displacements	40
Figure 2.9. Predicted displacement and frequency of the center of the stage in Z direction at 15V (all the legs actuated) as (a) the beam length changes, (b) the Au coverage on each beam changes while its length is fixed, (c) the thickness of the Au layer changes, or (d) the thickness of the PZT layer changes; (e) stage displacement vs generative force.....	45
Figure 2.10. Experimentally extracted effective electro-active piezoelectric strain coefficient from previous generation batch [2.1]	46
Figure 2.11. Fabrication process.....	49
Figure 2.12. Experimental static displacements of the stage.....	51
Figure 2.13. Microscope images of prototype scanners showing vertical motion	51
Figure 2.14. Transient response to a 5V impulse wave	52
Figure 2.15. DC Testing setup for characterizing differential-drive scanners	53
Figure 2.16. Static displacements of the stage when different combinations of legs are actuated	54
Figure 2.17. Reflectance mode remote scan setup (left: schematic from [2.7], right: tabletop setup made by collaborator Xiyu Duan, UM)	56
Figure 2.18. Sample scanner integrated into the imaging system in Figure 2.17	57
Figure 2.19. Actuator behavior with 5Hz triangular wave ($12V_{pp}$ $8V_{off}$).....	57
Figure 2.20. Images of beads taken at different focal plane (Photo credit: Xiyu Duan, Biomedical Engineering, UM)	58
Figure 2.21. Schematic of 3D multiphoton imaging system.....	59

Figure 2.22. Fluorescent bead imaging with remote axial scanning in multiphoton microscopy	60
Figure 3.1. Delamination of gold bonding pads.....	64
Figure 3.2. Delamination of gold layer on Legs	64
Figure 3.3. Concept aluminum jumper on a patch of parylene.....	65
Figure 3.4. Bending of a 10 μ m-thick stage (left) is noticeably more than that of a 30 μ m-thick stage (right)	66
Figure 3.5. Microscope image of the backside of a sample scanner with 10 μ m device layer after final release, focused on the handle layer of SOI	66
Figure 3.6. Microscope image of the backside of a prototype scanner with 30 μ m device layer after final release, focused on the handle layer of SOI	67
Figure 3.7. Release by DRIE.....	68
Figure 3.8. Microscope images of sample actuators that show etched device Si layer through the pinholes or over-etched areas in top SiO ₂ layer	69
Figure 3.9. Etched silicon structure during XeF ₂ etching due to voids in the SiO ₂ -filled trenches.....	69
Figure 3.10. Microscope images showing non-uniform XeF ₂ etching of silicon due to remaining fluorocarbon layer on the sidewalls from Bosch process.....	70
Figure 3.11. SEM images showing fluorocarbon layer on the sidewalls	71
Figure 3.12. SEM images of different outcomes of buried SiO ₂ layer	72
Figure 3.13. Microscope images of 1 st generation device without embedded mirror surface (left) and 2 nd generation device with embedded mirror surface (right).....	73
Figure 3.14. New fabrication process	74
Figure 3.15. Electrical jumpers made from aluminum pads and parylene insulation layer.....	75
Figure 3.16. Microscope images of backside of sample devices after step (f) in Figure 3.15 completed	76
Figure 3.17. Microscope images of backside of sample devices after step (g) in Figure 3.15 completed	76
Figure 3.18. Microscope images of backside of sample devices that show moving parts still have silicon in the handle layer after step (h) in Figure 3.15 completed.....	77

Figure 3.19. Microscope images of backside of sample devices that show all the silicon in the handle layer is etched after step (h) in Figure 3.15 completed.....	77
Figure 3.20. SEM images that show micro-columns formed during the DRIE release.....	78
Figure 3.21. “DRIE dicing” unmounts the dies near the wafer edges first.....	79
Figure 3.22. Delaminated PZT stack during process.....	79
Figure 3.23. Left: sample device whose pads and legs are reinforced with parylene, Right: sample device with no reinforcement	80
Figure 3.24. Simulated vertical displacement as a function of parylene thickness added to the bending legs.....	81
Figure 3.25. Silver epoxy applied to fix the jumpers	82
Figure 3.26. Sample actuator generating more twisting motion than vertical motion due to residual stress	83
Figure 3.27. Tilt profile of the stage of a sample differential-drive actuator with large initial tilt (left: scanning laser line of the displacement sensor, center: bottom left leg actuated, right: 0V position).....	83
Figure 3.28. Stage height profile of a sample device when two diagonal legs were actuated with 14V	84
Figure 3.29. AC testing setup.....	85
Figure 3.30. Frequency sweeping of a sample actuator with $4V_{pp}$ $2V_{off}$ sinusoidal input: (a) 70~150 Hz; (b) zoomed-in: 110~118 Hz; (c) definition of the displacements.....	85
Figure 3.31. Stage motion at 114 Hz (a) and 122 Hz (b).....	86
Figure 3.32. Schematic of XZ plane multiphoton imaging system using remote scan architecture	88
Figure 3.33. Steps to mount PZT actuator to a fixture for handheld system.....	89
Figure 3.34. (a) 15 μ m-diameter fluorescent bead imaging; (b) ex vivo image of FITC dyed mouse colon.....	90
Figure 3.35. 1 st generation actuator with manually mounted mirror on the stage.....	91
Figure 3.36. Motion of 1 st generation PZT scanner with a manually mounted mirror	91
Figure 3.37. 15 μ m diameter fluorescent beads imaged with smoother mirror surface.....	92

Figure 3.38. Excised FITC dyed mouse colon imaged with smoother mirror surface	92
Figure 4.1. Variation in fabrication outcomes	94
Figure 4.2. Schematic methodology for model development.....	96
Figure 4.3. Optical microscope image of Leg labeled with allowed dimensional variation	97
Figure 4.4. Schematic drawing of cross-section of unimorph labeled with allowed thickness variation, where Gap refers to the thickness of silicon device layer that was etched.....	98
Figure 4.5. Different beam geometries used for FEA to obtain torsional stiffness of Beam	102
Figure 4.6. FEA results, where slopes represent torsional stiffness.....	102
Figure 4.7. Parameter fitting results of static displacements when Legs A & D (translational Z) are actuated	105
Figure 4.8. Parameter fitting results of static displacements when Legs A & B (rotational about Y; ϕ) are actuated	105
Figure 4.9. Parameter fitting results of static displacements when Legs B & D (rotational about x; θ) are actuated.....	106
Figure 4.10. Estimated effective electro-active piezoelectric strain coefficient, $d_{31,eff}$	106
Figure 4.11. Parameter fitting results of static displacements of non-differentia-drive scanner	109
Figure 4.12. Estimated effective electro-active piezoelectric strain coefficient, $d_{31,eff}$	110
Figure 4.13. Transient response of the stage (left: $d_{31,eff}$ unadjusted; right; $d_{31,eff}$ adjusted)	111
Figure 4.14. Optical Images of 2 nd generation PZT scanners, labelled with definitions of legs and beams.....	113
Figure 4.15. Definitions of the angles and displacements of a leg, and effective external forces and moments applied to its tip (not drawn to scale).	116
Figure 4.16. Free body diagram of the stage with definitions of reaction forces and moments (not drawn to scale).....	120
Figure 4.17. Simulated shift of resonant frequencies (F_{res}) as V_{off} changes in the ideal case (no residual stress & perfect symmetry).....	124
Figure 4.18. Simulated resonant frequency (F_{res}) shift as non-uniform residual stress increases initial stage tilt in θ direction ($z_0=160 \mu\text{m}$)	125

Figure 4.19. Simulated resonant frequency (F_{res}) shift as non-uniform residual stress increases initial stage tilt in ϕ direction ($z_0=160 \mu\text{m}$)	126
Figure 4.20. Experimental frequency response with constant $6V_{pp}$ and varying dc voltages, showing the measurements taken at the top left (TL), top right (TR), bottom left (BL), and bottom right (BR) corner of the stage	128
Figure 4.21. Model prediction of the experimental results with constant $6V_{pp}$ and varying dc voltages, showing the measurements taken at the top left (TL), top right (TR), bottom left (BL), and bottom right (BR) corner of the stage	129
Figure 5.1. Microscope image of embedded piezoresistive sensing element	139
Figure 5.2. Microscope image of on-chip piezoelectric sensing element	139
Figure 5.3. Scanner integration into handheld dual axes confocal instrument: (a) before closed with a cap with objective lens; (b) zoomed in microscope picture of integrated scanner; (c) beam test with assembled instrument	140

LIST OF TABLES

Table 1.1. Comparison of imaging modalities in endomicroscopy.....	4
Table 1.2. Capabilities of previously developed miniature imaging instruments	10
Table 1.3. Actuator specifications needed for early cancer detection in endomicroscopy	14
Table 1.4. Existing commercial actuators based on conventional technologies	15
Table 1.5. Existing actuators based on MEMS technologies	15
Table 1.6. Comparison of properties of thin-film piezoelectrics	18
Table 1.7. Comparison between thin-film and bulk piezoelectrics	20
Table 2.1. Material properties and dimensions used for design optimization	46
Table 2.2. Static displacement of the stage.....	53
Table 2.3. Transient response of stage when Legs A & D are actuated	55
Table 3.1. Issues with 1 st generation devices and proposed solutions	73
Table 4.1. Nominal values of geometrical properties and their constraints and material properties for differential-drive scanner.....	100
Table 4.2. Obtained torsional stiffness for each geometry (Au coverage=70%).....	102
Table 4.3. Errors in μm between the measured and computed displacements as the number of possible parameter variation is increased.....	104
Table 4.4. Transient response of the stage.....	107
Table 4.5. Nominal values of geometrical properties and their constraints and material properties for non-differential-drive scanner	108

LIST OF APPENDICES

Appendix A: Nominal Model.....	141
Appendix B: Perturbed Model	143

ABSTRACT

The advancement of optics and the development of microelectromechanical systems (MEMS) based scanners has enabled powerful optical imaging techniques that can perform optical sectioning with high resolution and contrast, large field of view, and long working distance to be realized in endoscope-compatible form factors. Optical endomicroscopes based on these imaging techniques can be used to obtain *in vivo* vertical cross-sectional images of dysplastic tissues in the hollow organs before they progress to mucosal diseases such as colorectal cancer. However, existing endomicroscopic systems that use imaging modalities compatible with the use of fluorescent biomarkers are not capable of deep vertical sectioning in real time. This work proposes a unique MEMS-based scanning mechanism to be incorporated into endoscopic microscopes for real-time *in vivo* deep into-tissue scanning for early cancer detection.

For this task, a class of novel multi-axis micro-scanners based on thin-film lead-zirconate-titanate (PZT) has been developed. Leveraging the large piezoelectric strain coefficient of PZT, the prototypes have demonstrated more than 400 μm of out-of-plane displacement with bandwidths on the order of 100-200 Hz in only a 3.2 mm-by-3.2 mm footprint, which meets the requirements for this application. The scanners have a central rectangular-shaped reflector, whose corners are supported by four symmetric PZT bending legs that generate vertical translation. This design gives the reflector a three-axis motion.

The challenges to fabricate high performance piezoelectric actuators are discussed with device failure mechanisms observed during the fabrication of the 1st generation scanners. Improved

fabrication steps are presented that solve the issues with the 1st generation devices and enhance the robustness of the scanners for instrument integration.

Remaining non-ideal fabrication outcomes cause MEMS devices to produce unwanted motions, which can degrade imaging quality. To overcome this problem, a method to drive MEMS actuators having multiple vibration modes with close frequencies to produce a desired motion pattern with a single input is presented, and was used to generate a pure vertical motion for imaging. Two-photon based vertical cross-sectional images of mouse colon was obtained in real time for the first time using a thin-film piezoelectric microscanner.

To understand the effects of fabrication non-idealities on the device behavior and produce more robust scanner performance, analytical models that describes large vertical and rotational motions including multi-axis coupling were developed. A static model that was initially developed for design optimization was calibrated, along with a transient model, using experimental data to incorporate the effects of dimensional variations and residual stress. This models can be used with future integrated sensors and feedback controllers for more precise and robust motion of the scanner. This calibration technique can be useful in developing analytic models for MEMS devices subject to fabrication uncertainty. In addition, nonlinear dynamic behavior due to large vertical stroke in the presence of fabrication non-idealities is captured by linearizing an expanded dynamic model about different static positions obtained by numerically solving the expanded nonlinear model.

CHAPTER 1: INTRODUCTION

1. 1. Motivation

1. 1. 1. Need for *In Vivo* Vertical Cross-sectional Imaging

Engineering advances in optical design, miniature scanning mechanisms, and packaging techniques have enabled many breakthroughs in the field of biomedical imaging, but novel methods of endoscopic detection and diagnosis of disease are still in great need. One technique needed is the ability to rapidly visualize morphological features of hollow organs across their full depth (400~500 μm) *in vivo* at high resolution for early cancer detection in the digestive tract.

According to American Cancer Society, colon and rectal cancers are expected to be the third leading cause of cancer-related death in American men and women in 2015. When the cancer has not spread regionally, the mortality rate is as low as 10%, but only 40% of colorectal cancers are detected at this early stage [1.1]. While this low detection rate is partially due to some of the patients not having been screened, it is also due to technical limitations of current screening methods.

Currently, mucosal cancers and their precursors are detected based on the histological analysis of biopsied tissues obtained during white-light endoscopy. A study conducted for a year in a hospital in the UK reported that 40% of screening colonoscopies detected polyps, and more than

90% of these polyps were smaller than 1 cm. Out of these 90%, 80% were less than 5 mm and as many as half of these were not cancerous [1.2]. Performing polypectomy on all of these polyps creates unnecessary burden as the histology process not only can take a long time, delaying assessment, but also can produce artifacts, causing variation in interpretation. It is also an invasive and uncomfortable procedure and can be costly. If real-time, *in vivo* assessment of these polyps can be made, the management of mucosal diseases can be more effective, efficient, and economical. In the case of colorectal cancer, the cost savings could be as much as 77% [1.2].

Meanwhile, in conventional white-light endoscopy, reflected light from the tissue surface is collected for imaging, and this method is sufficient for detecting large and elevated polyps on the mucosal surface. However, localization of tumors growing from flat and depressed lesions is challenging; the polyp miss rate of white-light endoscopy is reported to be 28% [1.3].

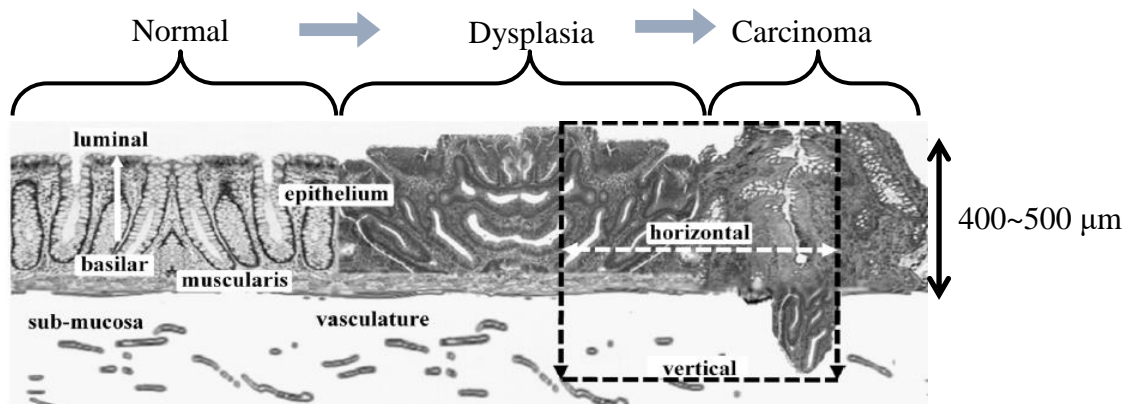


Figure 1.1. Progression from normal mucosa of hollow organs to carcinoma [1.4]

Figure 1.1 depicts how normal tissue progresses to a precancerous condition, called dysplasia, and then grows into malignant tumors (carcinomas) through cross-sectional images of the epithelium, the thin layer of tissue that forms the lining (mucosa) of hollow organs such as the colon and esophagus. Dysplasia can be diagnosed by current screening methods, but it is challenging to determine proper biopsy sites. Furthermore, because dysplasia in many medical conditions, including ulcerative colitis, Barrett’s esophagus, and gastric atrophy, is characterized by flat lesions, it is hard to detect by conventional white-light endoscopy even though its latency period is about 10 years.

The vertical cross-sectional view, in the direction perpendicular to the tissue surface as shown in the Figure 1.1, is the view that is conventionally evaluated by pathologists as it provides an overall picture of the condition. Many diseases that occur in hollow organs originate from the epithelium and change the morphology of the tissue. This morphological changes can be observed more clearly in the vertical cross-section than the horizontal cross-section, which tends to have a similar degree of differentiation and thus does not provide useful biological information. Dysplastic changes can be observed from the mucosal surface down to the muscularis, which is located about 400~500 μm below the tissue surface.

Thus, for an effective early detection of mucosal diseases in real time *in vivo*, a deep (400~500 μm) imaging depth is necessary, with a resolution of 5 μm to visualize abnormal morphological features of premalignant cells in the epithelium. In addition, a frame rate of at least 4 Hz is required to avoid motion artifacts caused by heartbeats and respiratory movement [1.4].

1. 1. 2. Optical Endomicroscopy for *In Vivo* Vertical Cross-sectional Imaging

Advanced non-invasive medical imaging techniques, such as x-ray computed tomography (CT) or magnetic resonance imaging (MRI), can detect far advanced carcinomas, but they do not have resolutions fine enough to detect dysplasia, let alone molecular changes developed well prior to morphological changes within the tissue. On the other hand, optical imaging techniques can provide sub-cellular resolution ($\sim 5 \mu\text{m}$) needed to image abnormal morphology of the cell nucleus. Also, rapid developments in light sources, optical fibers, and scanning mechanisms have allowed optical imaging systems to be portable and inexpensive. These make optical endomicroscopy well suited for obtaining *in vivo* vertical cross-sectional imaging with high

resolution in real time. Additionally, optical endomicroscopy can be used with biomarkers that specifically targets cancerous cells, which improves accuracy of early cancer detection.

Because of the aforementioned advantages of optical endomicroscopy, there has been much effort to develop miniaturized microscopes to make a significant contribution to clinical medicine. Endomicroscopes using various optical modalities, such as optical coherence tomography, two-photon microscopy, photoacoustic microscopy, and confocal microscopy, have been demonstrated with groundbreaking performance for a variety of applications, from *in vivo* animal studies to imaging human tissue and surgical guidance. Table 1.1 presents important characteristics of representative imaging modalities in endomicroscopy that can be used for early cancer detection.

Table 1.1. Comparison of imaging modalities in endomicroscopy

Imaging Modality	Deep Imaging	Sub-cellular Axial Resolution	Targeted Imaging	Comments
Single axis confocal		✓	✓	Commercialized
Dual axes confocal	✓	✓	✓	Challenging alignment of dual beam
Optical coherence tomography	✓	✓		Expensive detector
Two-photon	✓	✓	✓	Very expensive laser source and optics
Photoacoustic	✓		✓	Sub-cellular axial resolution achieved in larger systems
Desired	✓	✓	✓	For accurate early cancer detection

Existing commercial confocal endomicroscopes are based on the single axis confocal configuration, and they are not capable of achieving real-time *in vivo* deep (>400 μm) into-tissue imaging. They can perform very limited vertical cross-sectional imaging with very low speed [1.5] or shallow depth [1.6]. In single axis confocal microscopy, the fiber (pinhole) is located along the

optical axis of the objective (Figure 1.2). A high numerical aperture (NA) objective is used to maximize light collection and resolution, and this objective lens is used to both illuminate and collect light. Making the diameter of the objective small (< 5 mm) for endoscopic compatibility, both the working distance and field-of-view (FOV) are considerably sacrificed, making single axis confocal inadequate for deep into-tissue imaging *in vivo*.

On the contrary, in dual axes confocal configuration, two low NA objectives are used, where one is used for illumination and the other for collection, and their optical axes cross at an angle (Figure 1.2). The low NA objectives have a long working distance, allowing the scanner to be placed in the post-objective position, and thus providing a larger FOV than the pre-objective position used in single axis configuration (Figure 1.3). When the system is scaled down to millimeter dimensions, this location of the scanner allows the FOV and focal length to be limited only by the maximum scan angle of the scanner. By collecting light in the off-axis, the detection is minimally affected by the light scattered by tissue along the illumination path, and this uniquely allows for deep imaging.

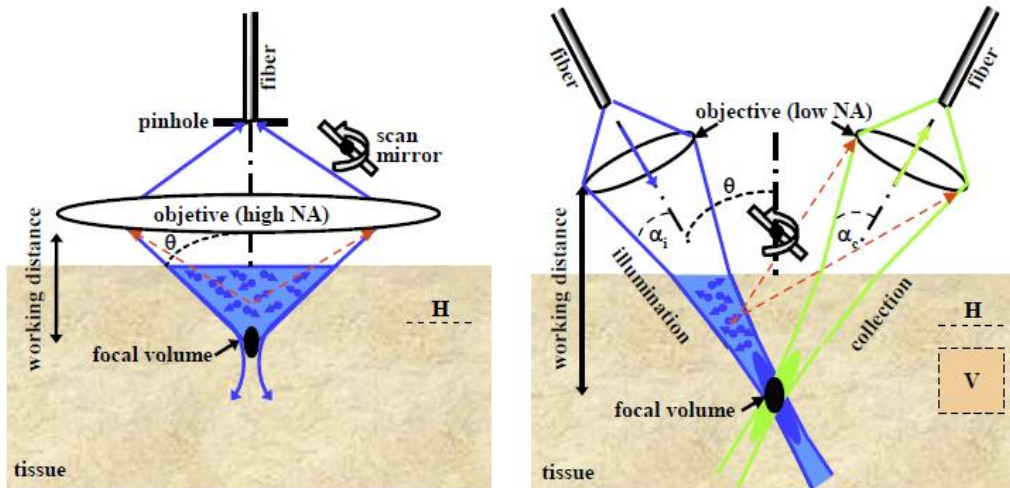


Figure 1.2. Left: conventional single axis confocal configuration; Right: dual axes confocal configuration [1.7]

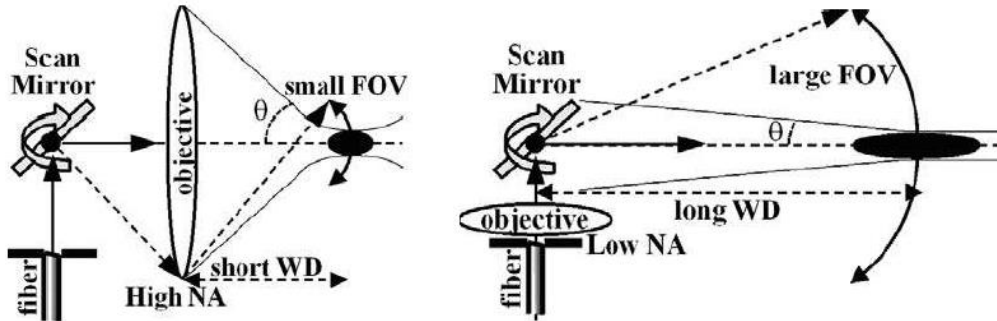


Figure 1.3. Scanning geometries (left: pre-objective scanning, right: post-objective scanning) [1.4]

Fluorescence imaging is another mode of imaging that can be deployed with dual axes confocal configuration. Compared to the reflectance imaging mode that uses backscattered light from within the tissue, this mode uses light generated by fluorescence contrast agents that highlights specific tissue and cellular targets. Targeted imaging of colonic dysplasia has been already demonstrated [1.8-1.10], and the capability to detect fluorescence adds another dimension to early diagnosis of mucosal diseases.

To capitalize on the advantages described above, much effort has been made to produce endomicroscopes based on the dual axes confocal architecture. In 2009, a miniature hand-held fluorescence dual axes confocal system was developed that could image horizontal cross-sections at an adjustable depth up to 300 μm at 5 Hz [1.11]. In 2012, a fluorescence endomicroscope with a 5.5mm outer diameter (OD) was built that was capable of scanning horizontal cross-sections, with variable imaging depth up to 140 μm [1.12]. In 2013, a deep (400 μm) vertical cross-sectional fluorescence imaging at 10Hz was demonstrated with a hand-held system as shown in Figure 1.4 [1.13]. In this system, the scanning in the tissue depth direction was realized by a relatively large actuator based on bulk PZT (Figure 1.5), and this is the component that needs to be miniaturized to achieve *in vivo* vertical cross-sectional images.

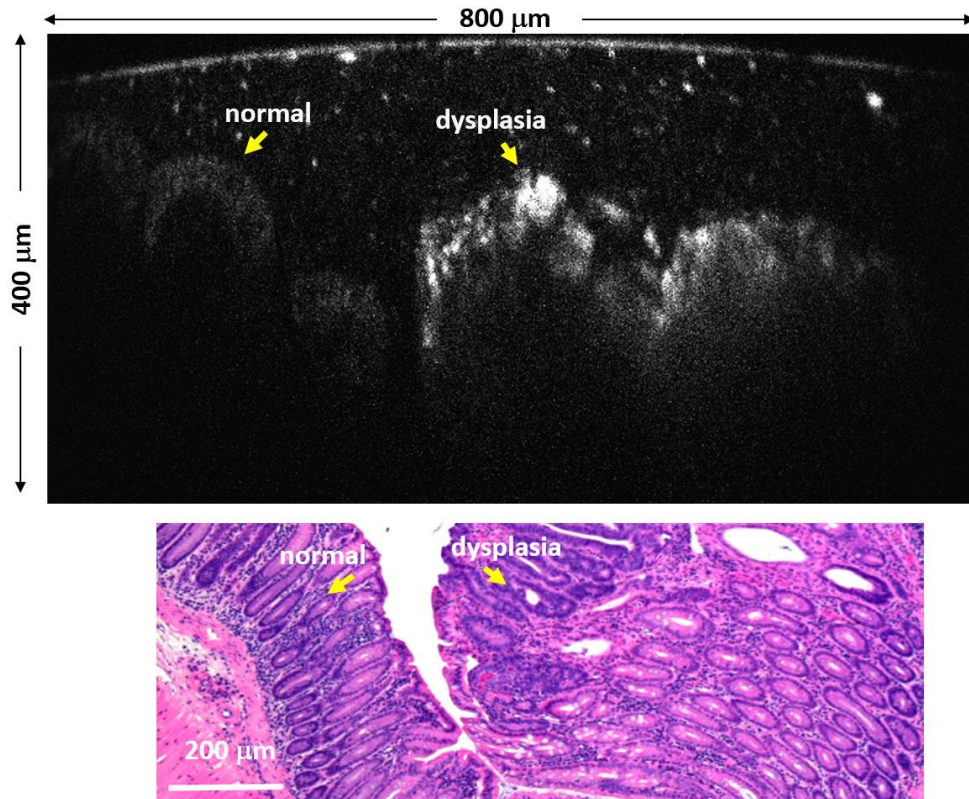


Figure 1.4. Vertical cross sectional image of colonic dysplasia (top: targeted imaging with Cy5.5 labeled peptide, down: corresponding histology stained with H&E) [1.13]

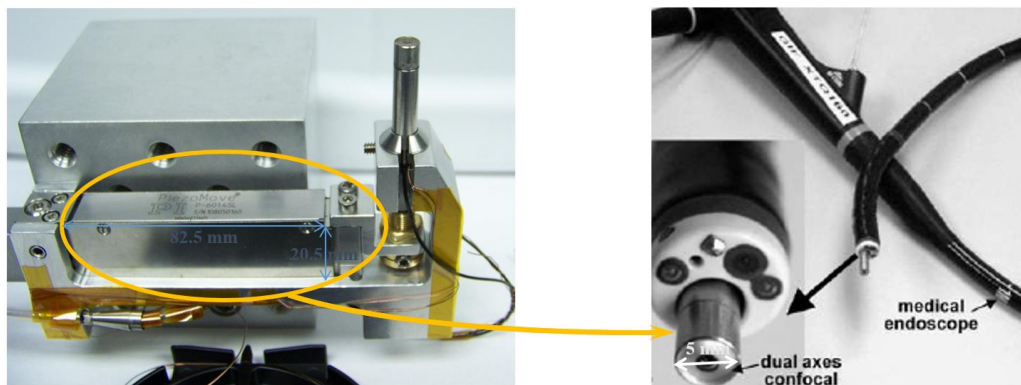


Figure 1.5. Left: photograph of handheld dual axes system with bulky PZT based PI actuator (circled) used in [1.13] (Photo credit: Dr. Zhen Qiu), Right: therapeutic endoscope

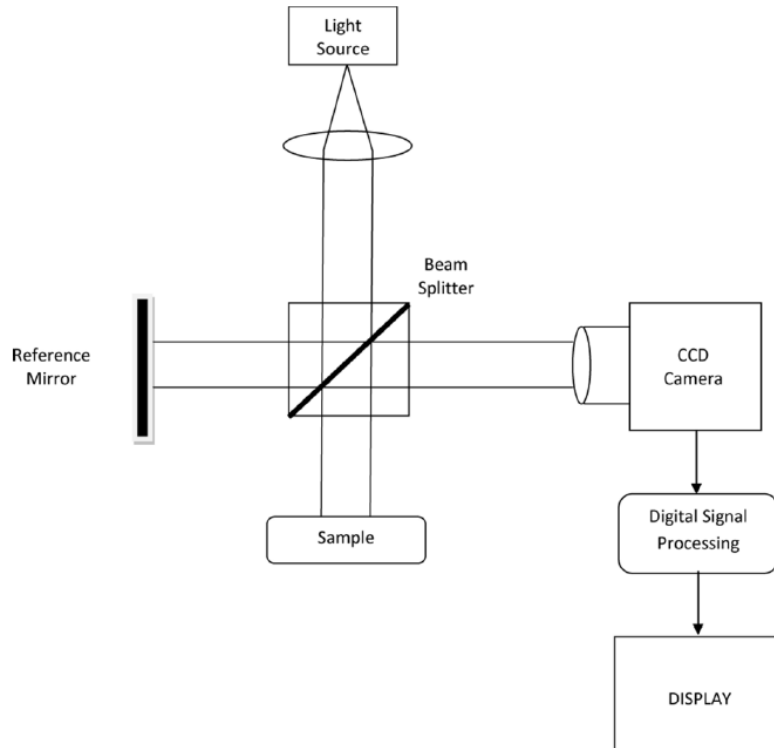


Figure 1.6. Schematic diagram of optical coherence tomography system [1.14]

Using the principle of interferometry, optical coherence tomography (OCT) has been much explored in endomicroscopy. In OCT, low-coherence light is split into two paths, where one is used as a reference and the other is directed into the tissue (Figure 1.6). Traveling in tissue, the light is reflected due to the difference in refractive index, and OCT uses the interference pattern of the reference beam and the reflected signal for rendering. Near-infrared light is used to deeply penetrate into tissue, and this can achieve an imaging depth as large as 1-3 mm. Coherent collection of backscattered light provides high resolution but cannot detect light generated by fluorescence, making OCT incompatible with fluorescence imaging (targeted imaging). Nonetheless, endomicroscopic systems with imaging probes that are smaller than 5 mm in outer diameter that can perform 3D imaging (focal volume $> 1\text{mm}^3$) have been developed [1.15-1.17]. Although their resolution ($\sim 10\ \mu\text{m}$) needs to be improved, their imaging speed and depth are sufficient for accurate early detection of mucosal diseases. OCT endomicroscopy was further developed into a swallowable tethered capsule to collect 3D reflectance images of esophagus [1.18].

In two-photon microscopy, fluorescence is generated when a biomolecule that fluoresces is excited by the simultaneous absorption of two lower energy photons. For deeper tissue penetration, near infrared radiation is used. To increase the probability of concurrent absorption of two photons, ultra-short, high peak-intensity pulses of light are necessary, which is a disadvantage as the price of femtosecond lasers is very high. Nevertheless, much progress has been made in this modality as well. Small endoscopic instruments (outer diameter < 5 mm) capable of imaging at different depths with an excellent lateral resolution were reported [1.19-1.21], but their vertical actuation mechanisms lack the speed required for vertical sectioning. Vertical cross sectional imaging based on endoscopic probes for early cancer detection has yet to be demonstrated.

In photoacoustic microscopy, short pulses of laser light are used to locally heat up tissue of interest and cause it to expand thermoelastically. The pressure transients due to the expansion produce ultrasonic waves that represent the absorbing structure. These waves are detected by an ultrasonic sensor to generate an image. Using photoacoustic microscopy, submicron lateral resolution with imaging depths on the order of millimeters has been reported [1.22, 1.23]. The axial resolution is usually worse than the lateral resolution, but using a broad bandwidth ultrasonic transducer an axial resolution of 7.6 μm has been achieved with a penetration depth of 1.2mm on biological samples using tabletop systems [1.24]. Also, combined with other effects, even submicron axial resolutions have been demonstrated [1.25, 1.26]. Catheter-based photoacoustic systems have been developed, but their resolutions (axial: 50 μm and lateral: 10 μm with imaging depth of 6.5mm) [1.27, 1.28] are not as high as tabletop setups or systems with all miniature components (lateral and axial resolutions of 8.8 μm and 19 μm , respectively with a field of view of 0.9mm x 0.9mm) [1.29]. Photoacoustic microscopy can be used with both endogenous and exogenous contrast agents.

In summary, dual axes confocal microscopy, OCT, two-photon, and photoacoustic microscopy are among the imaging modalities that can provide deep into-tissue imaging needed for early detection of mucosal diseases. The capabilities of previously developed miniature imaging

instruments based on these techniques are summarized as in Table 1.2. No dual axes confocal-based and two-photon-based endomicroscopes have yet demonstrated vertical sectioning, and OCT is not compatible with targeted imaging as mentioned earlier. Photoacoustic based catheter systems have demonstrated very large axial imaging depth but relatively poor axial resolution.

Table 1.2. Capabilities of previously developed miniature imaging instruments

Imaging Modality	Work	Real-time imaging	Horizontal sectioning	Vertical sectioning	Cellular resolution	Endoscope compatibility	Targeted imaging
Dual axes confocal	[1.12]	✓	✓		✓	✓	✓
	[1.13,1.32]	✓		✓	✓		✓
Optical coherence tomography	[1.15-1.17]	✓	✓	✓		✓	Not compatible
Two-photon	[1.19-1.21]	✓	✓			✓	
Photoacoustic	[1.30]	✓	✓	✓		✓	✓
Desired		✓		✓	✓	✓	✓

1. 1. 3. Miniature Scanning Mechanisms for Endomicroscopy

In realizing high-performance miniature imaging instruments such as those presented in Table 1.2, the beam scanning mechanism, besides the micro-optics, is very important. These instruments have scanning mechanisms that either direct a laser beam or mechanically scan an optical fiber. They are placed at the proximal end or distal end of the endoscope catheter, depending on their size and the optics. It is generally beneficial to position the scanning mechanism distally to have a greater control of the focal volume for advanced imaging, such as deep vertical sectioning. For fiber scanning, single-axis cantilever, spiral, and rotational actuators

have been used. For beam scanning, galvanometer mirror scanners that use electromagnetic transduction have been used traditionally, but their relatively large size limits their location at the proximal end of the endoscopic instrument. Recent microelectromechanical systems (MEMS) based micro-scanners have many advantages over conventional actuation mechanisms. They can provide large scan range, fast scanning and high dynamic bandwidth in a power-efficient manner and also at low cost. In addition, due to their small size, they can be placed at the distal end of the instrument with use of flexible optical fibers. It is the MEMS based scanning actuators that have allowed many of the listed instruments to have unprecedented capabilities in such a small scale.

As described in Table 1.2, not only vertical sectioning but large volumetric imaging has been achieved in OCT and photoacoustic endomicroscopy. Figure 1.7 shows a schematic of a fiber based time-domain OCT using a Michelson interferometer, where a depth scan can be achieved by scanning the reference arm, for instance, using a stepper motor. In Fourier-domain OCT, reflected light from the measurement head is Fourier-transformed to generate a depth-dependent reflection signal, making the depth scan unnecessary to realize vertical sectioning. Thus, the scanning probe of an OCT endomicroscope does not need to have the capability to scan in the tissue depth direction for vertical cross-sectional imaging or 3D imaging. Photoacoustic microscopy is another modality that could achieve 3D imaging without axial scanning as focused light is not necessary to produce photoacoustic signals and depth information can be extracted from acoustic travel time in pulsed excitation.

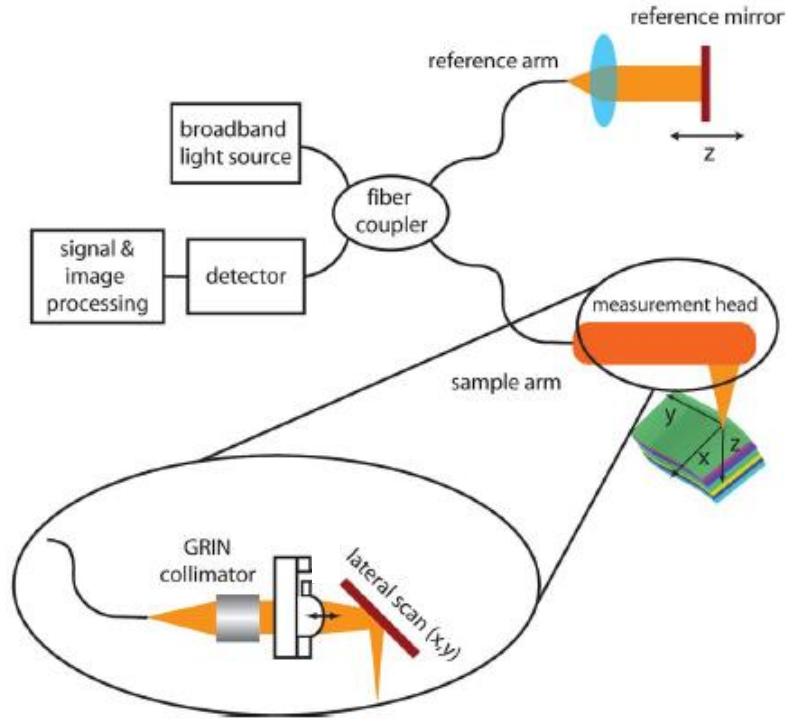


Figure 1.7. Schematic of a time domain OCT system based on a Michelson interferometer [1.31]

Other imaging modalities require an axial (*i.e.* the tissue depth direction) scanning capability in the miniature scanning probe for vertical cross-sectioning. This is the case if the scanning mechanism needs to be distally positioned and still move the focal point of the light axially, as it can be in dual axes confocal endomicroscopy and two-photon endomicroscopy. As an example, a possible optical configuration of a dual axes confocal endoscope is illustrated in Figure 1.8, and it shows that scanning in the z (axial) direction moves the focal point in the tissue depth direction. In order to use the endomicroscopic systems that utilizes optical configurations like this for vertical sectioning, a miniature mechanism to quickly scan a large axial range is necessary.

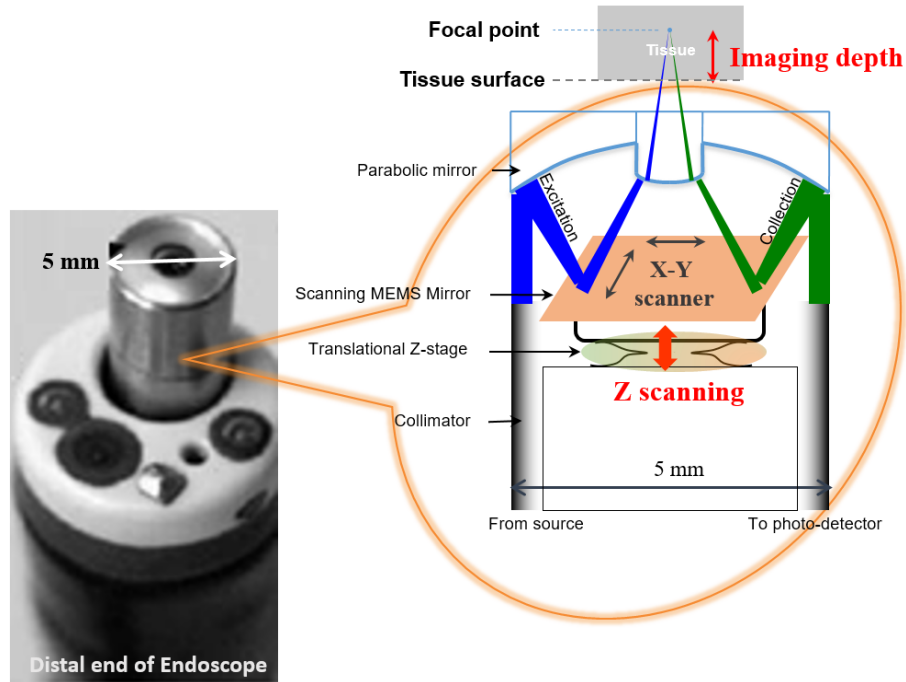


Figure 1.8. Schematic of miniaturized scanning probe based on dual axes confocal microscopy

Thus, the goal of this work is to develop a micro-scanner that can produce sufficient speed and displacement in a small form factor for real-time *in vivo* deep vertical cross-sectioning in endomicroscopy for early diagnosis of mucosal diseases.

1. 1. 4. Actuator Specifications Needed for Real-time Vertical Sectioning in Endomicroscopy

Current screening techniques for mucosal diseases such as colorectal cancer are not adequate to detect morphological changes occurring underneath the tissue surface in the pre-cancer stage. If vertical cross-sections of tissue, from the tissue surface down to 400~500 μm , can be visualized with a resolution of 5 μm *in vivo* in real time, then abnormal morphological features of precancerous cells can be detected and mortality rate for mucosal diseases may possibly be significantly decreased.

Contrary to other medical imaging techniques, such as magnetic resonance imaging (MRI), optical endomicroscopy can provide the required sub-cellular resolution *in vivo* in real time at a relatively low cost. Certain optical endomicroscopic techniques can also utilize fluorescent biomarkers that are specific to certain disease to further increase diagnosis accuracy.

However, existing endomicroscopic systems using imaging modalities that can also perform targeted imaging with biomarkers do not have the capability to image vertical cross-sections in real time. In order to achieve real-time *in vivo* deep into-tissue imaging with such systems, a miniature scanning mechanism compatible with medical endoscopes that can quickly scan a large range is needed (Table 1.3). With optical setups using unity magnification such as in [1.13], the scanning actuator needs to move the focal point 400-500 μm in the tissue depth direction to achieve an imaging depth of 400-500 μm . To avoid motion artifacts from respiratory motion and heartbeats, the scanner needs to have a minimum bandwidth of 10Hz. The scanner also needs to fit in an imaging probe that will be inserted into a 5mm diameter instrument channel of a standard medical endoscope shown in Figure 1.8. It is desirable to have pure vertical scanning motion, but it is possible to change the optical configuration to accommodate off-axis rotation of the scanner.

Table 1.3. Actuator specifications needed for early cancer detection in endomicroscopy

Desired capabilities	Specifications Needed
Deep into-tissue imaging	Stroke: 400-500 μm
Real time imaging	Bandwidth > 10 Hz
In vivo imaging	Footprint < 5mm in diameter
Minimal image distortion	Off-axis rotation < 0.5°

1. 2. Existing Actuator Technologies

There are conventional DC motors and bulk piezoelectric actuators that can produce a millimeter-scale displacement as presented in Table 1.4. They generate more than sufficient stroke length and speed needed for early cancer detection. However, each mechanism has its own limitation, and they all face serious limitations at the endoscopic scales. On the other hand, miniaturized scanning mechanisms based on micro-electromechanical systems (MEMS) can meet the size requirement while also providing high performance. These advantages of MEMS technology have led rapid development of scanning micro-mirrors for various optical applications. A number of vertical translational actuators with different actuation mechanisms have been developed for a footprint less than 5~6 mm in diameter, and some representative work is presented in Table 1.5. However, due to limited work density available by common MEMS transduction mechanisms, it is challenging to produce actuators with a high speed and large stroke length, and some mechanisms have intrinsic limitations in an endoscopic system.

Table 1.4. Existing commercial actuators based on conventional technologies

Actuation type	Stoke	Speed	Size (L x W x D)	Limitations
Linear DC motor (Faulhaber LM0830)	15 mm	1.8 m/s	8 x 8 x 80 mm	Undesirably long Significant backlash
Bulk Piezoelectric (PI P-602.5)	0.6 mm	230 Hz	8 x 26 x 9 mm	Undesirably long High voltage Significant hysteresis
Piezoelectric SQUIGGLE motor (Newscale RV)	6 mm	10 mm/s	1.8 x 1.8 x 6 mm	Undesirably long Large pre-load required Lateral vibration
Required	400~500 μ m	>10 Hz	< 3.5 x 3.5 (<5 mm in diameter)	

Table 1.5. Existing actuators based on MEMS technologies

Actuation type	Work	Stoke (μ m)	Speed (Hz)	Footprint (mm)	Limitation
Electrothermal	[1.33]	800	Not reported	3 x 3	High temperature Relatively slow
Electrostatic	[1.34]	510	>450	3.2 x 2.9	High voltage
Pneumatic	[1.36]	80	Not reported	7 x 1.8	External fluid
Electromagnetic	[1.37]	42	7.3k	> 1 x 1	Coil size

SMA	[1.38]	150	0.43	0.08 (diameter)	Heat & speed
Piezoelectric	[1.39-1.41]	<50	Order of 10^3	< 4.2 x 4.2	Large angular displacement
Thin-film PZT	This work	>400	100	3.2 x 3.2	Nonlinearity
Required		400~500	>10	< 3.5 x 3.5 (<5 mm in diameter)	

In general, electrostatic actuators have fast scanning speed and low power consumption, but usually their voltage requirement is high ($> 100V$), which is not desirable for an in vivo imaging device, even when producing small displacements ($\leq 150\mu m$) [1.35, 1.42, 1.43]. Recently, Li *et al* developed an electrostatic actuator that can generate very large displacement ($>500 \mu m$) using parametric excitation [1.34], but the voltage is still relatively high and the performance can be reduced as damping can increase when packaged in a small form factor. Although electromagnetic actuators have produced 9° of angle or more, their out-of-plane displacements are small ($< 50\mu m$) [1.37, 1.44, 1.45]. Electrothermal actuators can produce large displacements at a low voltage, e.g. $800\mu m$ [1.33] or $480\mu m$ in the z-axis and 30° about the x and y axes at 8V as reported in [1.46], but their high power consumption increases the device temperature, which can be undesirable in in vivo endoscopy. Also, their relatively large thermal time constant limits scanning speed. SMA actuators can generate large force and strain, but their potential limitations are similar to electrothermal actuators due to heating.

Piezoelectric actuators can overcome many of the aforementioned limitations of other types of actuators with their low voltage and power requirements, minimal heat dissipation, and large work density. Piezoelectric actuators with the desired degree-of-freedom have been previously developed, but so far they have been intended for other types of endoscopic imaging and have consequently not targeted sufficiently large vertical translation for dual axes confocal microscopy, although they produced large angular displacements ($\sim 10^\circ$ or even larger than 30°) [1.39-1.41, 1.47].

1. 3. Piezoelectricity

With the Greek prefix *piezo* meaning pressure, piezoelectricity refers to two linear electromechanical responses, the direct piezoelectric effect and the converse or inverse piezoelectric effect. Discovered by Pierre and Jacques Curie in 1880 [1.48-1.50], the direct piezoelectric effect describes a phenomenon of the generation of charge and thus electric polarization in a substance due to an applied stress, in which the polarization or the induced electric displacement is proportional to the applied stress. The converse piezoelectric effect was first mathematically predicted by G. Lippmann in 1881 [1.51], and it describes a phenomenon where a substance becomes strained when electrically polarized by an applied electric field, in which the induced strain is proportional to the applied electric field. Majority of crystallographic classes (20 out of 21) that have a non-centrosymmetric crystal structure exhibit these piezoelectric effects, although the number of piezoelectric materials found is only a few thousands out of several millions of all known materials [1.52].

Among the piezoelectric materials, there is a subset of materials called polar materials, or pyroelectrics, that naturally has permanent dipoles and thus spontaneously develops polarization without an applied electric field due to their crystalline structure. This intrinsic polarization changes with temperature. Among the pyroelectric materials, there is another subset called ferroelectric materials. These materials have permanent dipoles that can be reoriented by an applied electric field.

A common ferroelectric crystal structure is the perovskite structure, and it has a cubic lattice above the Curie temperature (Figure 1.9 (1)) that can be distorted, for example, to a tetragonal form below the Curie temperature (Figure 1.9 (2)). Distortions like this move the central cation, making the structure polarized, and this is usually how permanent dipoles are developed in ferroelectrics. If used for actuation, an electric field is applied to these polarized crystallites, and depending on the polarity of an applied electric field, the crystallites elongate or contract.

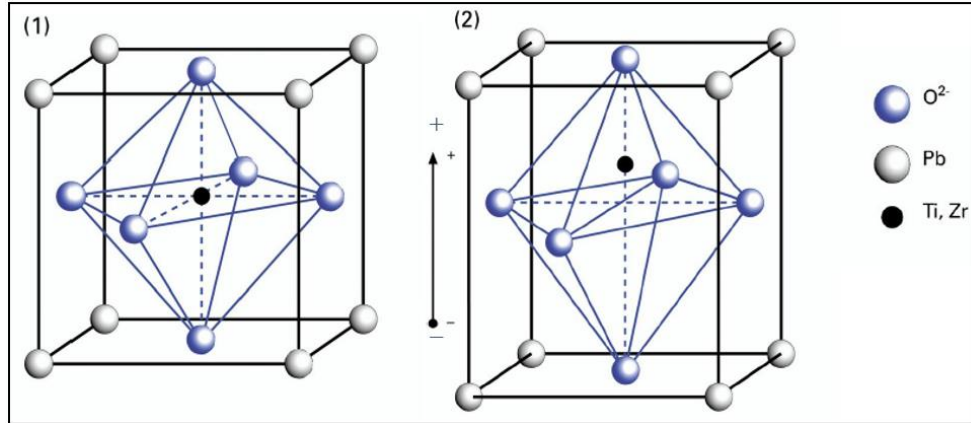


Figure 1.9. Crystal structure for a piezoelectric ceramic: (1) cubic above Curie temperature; (2) tetragonal below Curie temperature [1.53]

As ferroelectric ceramics are cooled down from the Curie temperature, regions with different orientations of the permanent dipoles, called domains, are formed to minimize their elastic and electric energy. When averaged over the entire sample, the domains cancel out the piezoelectric effects of the individual crystallites, generating a small ferroelectric effect on the macroscopic level. Ferroelectric ceramics can be transformed into polar materials by a process called poling, where a high static field is applied while the materials are heated up above the Curie temperature and cooled down to orient all the dipoles in the direction of the applied electric field. After being cooled down and the having electric field removed, most dipoles remain in their new orientation because of the pinning effect caused by microscopic defects in the crystalline lattice. Ferroelectrics can be de-poled if exposed to a high temperature ($>$ Curie temperature) or subjected to large stress or electric field.

Table 1.6. Comparison of properties of thin-film piezoelectrics

	ZnO	AlN	PZT	PNZT	PMN-PT
$-e_{31,f}$ (C/m ²)	1	1.02	12	25	23 ~ 27
$d_{33,f}$ (pC/N)	5.9	3.4	85	Not reported	265.5
ϵ_{33}	10.9	10.4	935	1209	1680 ~ 8200
$\tan \delta$	0.01 ~ 0.1	0.002	0.036	0.02	Not reported

$\left \frac{e_{31,f}}{\varepsilon_0 \varepsilon_{33}} \right $	1.04e10	1.11e10	1.45e9	2.34e9	3.16e8 ~ 1.81e9
$\left \frac{e_{31,f}}{\sqrt{\varepsilon_0 \varepsilon_{33} \tan \delta}} \right $	3.22e5 ~ 1.02e6	2.38e6	6.95e5	1.71e6	Not reported
Reference	[1.54, 1.55]	[1.56]	[1.57]	[1.58, 1.59]	[1.60, 1.61]

Table 1.6 lists piezoelectric and dielectric properties of representative thin-film piezoelectric materials used in MEMS devices, but these values can vary greatly depending on the film thickness, substrate materials and conditions, and deposition technique. As figures of merit $\left| \frac{e_{31,f}}{\varepsilon_0 \varepsilon_{33}} \right|$ for piezoelectric voltage in deflected piezoelectric composite and $\left| \frac{e_{31,f}}{\sqrt{\varepsilon_0 \varepsilon_{33} \tan \delta}} \right|$ for signal-to-noise ratio indicate, polar materials, such as ZnO and AlN, are better suited for sensing applications. Other advantages of AlN are its compatibility with conventional complex metal-oxide semiconductor (CMOS) processing and its large resistivity that gives a loss dielectric loss at low frequencies. The effective piezoelectric stress coefficient, $e_{31,f}$ is a figure of merit for deflection force or generated charge in deflected piezoelectric composites. Doped PZT films, such as PNZT, or single crystal ferroelectrics, such as PMN-PT, show very large piezoelectric coefficients, which makes them very attractive for actuators, but currently their processing cost is higher than that of pure PZT ceramics. Piezoelectric coefficients of single crystals are about 4~6 times larger than those of doped PZT [1.62], but they do not generate corresponding large stress due to their low stiffness. With less expensive processing cost, more researched behaviors, and comparable piezoelectric properties, pure thin-film lead zirconate titanate (PZT) has been more used in micro-actuator applications.

PZT ceramics are used in two forms, bulk and thin-film, and they are different in many ways (Table 1.7). While bulk piezoelectric are sintered at as high as 1400°C, sol-gel spin-coated thin-films are crystallized at much lower temperature. Thin-film piezoelectrics are usually used in a composite structure, thus their stiffness is greatly affected by other layers in the composite, such as elastic and electrode layers, whereas bulk piezoelectrics are usually much thicker than other layers in the structure. Due to their small thickness, thin-films are considerably affected by residual stress

and experience very large fields. One other important difference is that even very small negative voltages (as little as -2V for a 0.5 μm -thick PZT) can produce reverse coercive fields in PZT thin films, and that is why they are commonly used under unipolar positive voltages in contraction mode.

Table 1.7. Comparison between thin-film and bulk piezoelectrics

Properties	Thin-film	Bulk
Process temperature	Below 750°C	1100-1400°C
Thickness	<5 μm	>100 μm
Piezoelectric properties	Lower coefficient Higher field	Higher coefficient Lower field
Stiffness	Governed by elastic layers	Governed by piezoelectric material
Effect of residual stress	Considerable	Negligible

Because of their lower processing temperature, thin-film piezoelectrics are easier to be integrated in MEMS devices than bulk piezoelectric ceramics, although integration of bulk ceramics has been demonstrated [1.63-1.66]. Researchers bonded bulk piezoelectrics on silicon wafers and thinned them to a desired thickness (5~100 μm) to take advantage of more repeatable and higher piezoelectric coefficients of bulk piezoelectric materials for applications that could benefit from thicker films than what thin-film deposition techniques can offer. For applications where very large out-of-plane displacement is needed, such as the vertical cross-sectioning in endomicroscopy of this dissertation work, it is advantageous to use thin-film piezoelectric for more compliant structures.


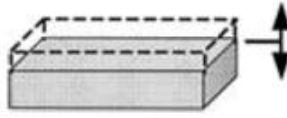
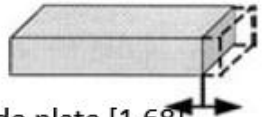
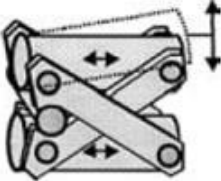
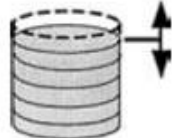
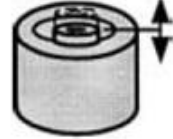
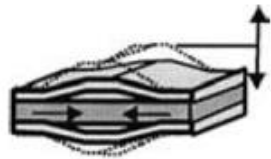

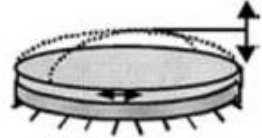

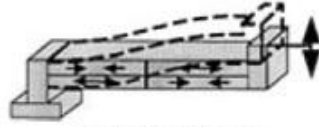
External Leverage	Internal Leverage	
 <p>Leverage stack [1.67]</p>	 <p>d_{33} mode plate [1.68]</p>	 <p>d_{31} mode plate [1.68]</p>
 <p>X-frame [1.69]</p>	 <p>Stack [1.69]</p>	 <p>Telescopic [1.70]</p>
 <p>Moonie [1.74, 1.75]</p>	 <p>C-Block [1.71]</p>	 <p>Rainbow [1.72, 1.73]</p>
	 <p>Bimorph Bender [1.76,1.77]</p>	 <p>Recurve [1.78]</p>

Figure 1.10. Externally and internally leveraged bulk piezoelectric actuator structures, figures from [1.70, 1.71]

Due to small strain that PZT ceramics produce, there have been developed many innovative amplification mechanisms to generate useful out-of-plane displacement using bulk piezoelectrics [1.62-1.73] as shown in Figure 1.10. They can be categorized into internal leverage mechanisms that use piezoelectric structure and external leverage mechanisms that use external mechanical components to amplify the generated displacement. However, regardless of their class, complicated amplification schemes are difficult to realize in a MEMS device due to the planar character of its structures. Also, piezoelectric MEMS devices do not utilize the induced strain directly as the bulk multilayer stack actuators because of their small magnitude. Thus, simple and planar leverage mechanisms, such as unimorphs and bimorphs (Figure 1.11) with flexural leverage, are implemented in MEMS devices. Again, because of their planar structures, electric field is most often applied through film thickness via parallel plate electrodes for the d_{33} mode

that uses induced strain in the film thickness direction or the d_{31} mode that uses induced in-plane strain, which is more commonly used (Figure 1.12).

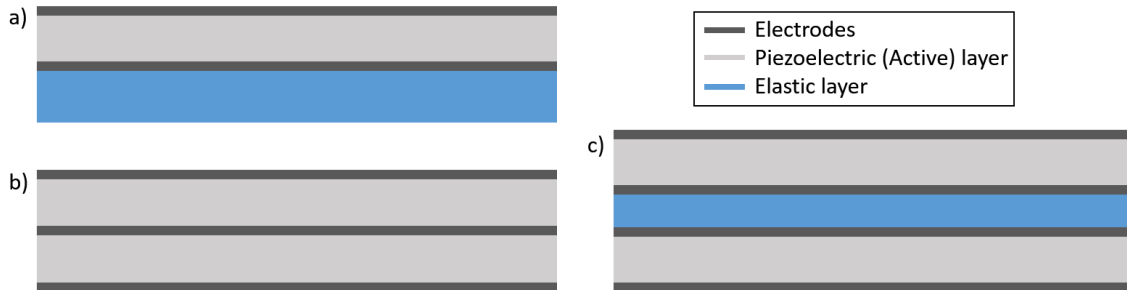


Figure 1.11. Schematics of cross-section of thin-film piezoelectric unimorph (a), bimorph with common electrode in the middle (b), bimorph with elastic layer (c)

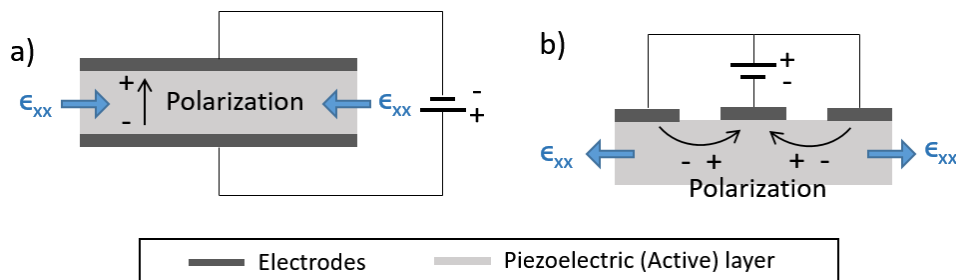


Figure 1.12. Cross-sectional schematics of d_{31} actuation mode (a) and d_{33} actuation mode (b)

1. 4. Research Goals and Thesis Overview

To meet the technical needs described earlier in this chapter, this dissertation presents the development work of a class of high performance micro-actuators based on thin-film PZT, one of most commonly used piezoelectric materials. The objective of this dissertation is to address primary challenges in developing large-deflection piezoelectric MEMS scanners to achieve real-time vertical cross-sectional imaging.

Specifically, the goals of this thesis are:

1. To design and fabricate a thin-film PZT micro-actuators that can generate a fast and large vertical motion in a small footprint to meet the specifications needed for early cancer detection in endomicroscopy
2. To characterize its performance and develop a model to understanding its behavior for successful imaging
3. To demonstrate real-time vertical cross-sectional imaging of biological tissue using the developed piezoelectric micro-actuators.

Driven by the motivation discussed in this chapter, Chapter 2 introduces the actuator geometry, its static model developed for design optimization, and fabrication of the 1st generation PZT actuators. Then, their performance and initial imaging testing results are presented.

Chapter 3 begins with the discussion of the problems of the 1st generation actuators observed during fabrication, testing, and imaging, followed by the fabrication of the 2nd generation actuators with improved fabrication processes. Along with the characterization results, a method to dynamically produce a pure out-of-plane stage motion is introduced. This method was then used to report the first vertical two-photon cross-sectional imaging of biological tissue by a thin-film piezoelectric micro-actuator.

Chapter 4 first introduces a technique to calibrate an ideal static and transient model by accounting for the effects of non-ideal MEMS fabrication outcomes such as dimensional variation and residual stress. This technique can be used for compensating unwanted motions of the scanner running at low frequency. Also, another model is developed that describes the influence of very large stroke translation of a vertical actuator on its resonant behavior, which is useful for high speed scanning.

Chapter 5 summarizes this thesis work and its contributions and proposes suggestions for future work.

1. 5. References

- [1.1] American Cancer Society. Cancer Facts & Figures 2015. Atlanta: American Cancer Society; 2015.
- [1.2] Ignjatovic, Ana, et al. Optical diagnosis of small colorectal polyps at routine colonoscopy (Detect InSpect ChAracterise Resect and Discard; DISCARD trial): a prospective cohort study." *The lancet oncology* 10.12 (2009): 1171-1178.
- [1.3] Heresbach, D., et al. Miss rate for colorectal neoplastic polyps: a prospective multicenter study of back-to-back video colonoscopies. *Endoscopy* 40.4 (2008): 284-290.
- [1.4] Handbook of Photonics for Biomedical Science. Handbook of Photonics for Biomedical Science, 1-810, doi:10.1201/9781439806296-f (2010).
- [1.5] R. Kiesslich, et al., Confocal laser endoscopy for diagnosing intraepithelial neoplasias and colorectal cancer in vivo, *Gastroenterology*, vol. 127, pp. 706-13, Sep 2004.
- [1.6] Mauna Kea, Cellvizio, <http://www.maunakeatech.com/en>
- [1.7] Piyawattanametha, Wibool, and Thomas D. Wang. MEMS-based dual-axes confocal microendoscopy. *Selected Topics in Quantum Electronics, IEEE Journal of* 16.4 (2010): 804-814.
- [1.8] Goetz, Martin, et al. In vivo molecular imaging of colorectal cancer with confocal endomicroscopy by targeting epidermal growth factor receptor. *Gastroenterology* 138.2 (2010): 435-446.
- [1.9] Hsiung, Pei-Lin, et al. Detection of colonic dysplasia in vivo using a targeted heptapeptide and confocal microendoscopy. *Nature medicine* 14.4 (2008): 454-458.
- [1.10] Goetz, Martin, and Thomas D. Wang. Molecular imaging in gastrointestinal endoscopy. *Gastroenterology* 138.3 (2010): 828-833.
- [1.11] W. Piyawattanametha, H. Ra, M.J. Mandella, K. Loewke, T.D. Wang, G.S. Kino, O. Solgaard, C.H. Contag, 3-D Near infrared fluorescence imaging using a MEMSbased miniature dual-axes confocal microscope, *IEEE J. Sel. Top. Quant. Electron.* 15 (5) (2009) 1344–1350.

- [1.12] W. Piyawattanametha, H. Ra, Z. Qiu, S. Friedland, J.T.C. Liu, K. Loewke, G.S. Kino, O. Solgaard, T.D. Wang, M.J. Mandella, C.H. Contag, In vivo near-infrared dualaxis confocal microendoscopy in the human lower gastrointestinal tract, *J. Biomed. Opt.* 17 (2) (2012) 0211021–0211024.
- [1.13] Z. Qiu, Z. Liu, X. Duan, S. Khondee, B. Joshi, M.J. Mandella, K. Oldham, K. Kurabayashi, T.D. Wang, Targeted vertical cross-sectional imaging with handheld near-infrared dual axes confocal fluorescence endomicroscope, *Biomed. Opt. Exp.* 4 (2) (2013) 322–330.
- [1.14] Dhawan, Atam P., Brian D'Alessandro, and Xiaolei Fu. Optical imaging modalities for biomedical applications. *Biomedical Engineering, IEEE Reviews in* 3 (2010): 69-92.
- [1.15] A.D. Aguirre, P.R. Hertz, Y. Chen, J.G. Fujimoto, W. Piyawattanameth, L. Fan, M.C. Wu, Two-axis MEMS scanning catheter for ultrahigh resolution threedimensional and en face imaging, *Opt. Exp.* 15 (5) (2007) 2445–2453.
- [1.16] W. Jung, D.T. McCormick, J. Zhang, L. Wang, N.C. Tien, Z. Chen, Three-dimensional endoscopic optical coherence tomography by use of a two-axis microelectromechanical scanning mirror, *Appl. Phys. Lett.* 88 (16) (2006) 163901–163903.
- [1.17] D. Wang, L. Fu, X. Wang, Z. Gong, S. Samuelson, C. Duan, H. Jia, J.S. Ma, H. Xie, Endoscopic swept-source optical coherence tomography based on a two-axis microelectromechanical system mirror, *J. Biomed. Opt.* 18 (8) (2013) 086005–086009.
- [1.18] Gora, Michalina J., et al. Tethered capsule endomicroscopy enables less invasive imaging of gastrointestinal tract microstructure. *Nature medicine* 19.2 (2013): 238-240.
- [1.19] Y. Wu, Y. Leng, J. Xi, X. Li, Scanning all-fiber-optic endomicroscopy system for 3D nonlinear optical imaging of biological tissues, *Opt. Exp.* 17 (10) (2009) 7907–7915.
- [1.20] Bao, Hongchun, et al. Fast handheld two-photon fluorescence microendoscope with a 475 $\mu\text{m} \times 475 \mu\text{m}$ field of view for in vivo imaging. *Optics letters* 33.12 (2008): 1333-1335.
- [1.21] Rivera, David R., et al. Multifocal multiphoton endoscope. *Optics letters* 37.8 (2012): 1349-1351.

- [1.22] Zhang, C., Maslov, K. and Wang, L.V., 2010. Subwavelength-resolution label-free photoacoustic microscopy of optical absorption in vivo. *Optics letters*, 35(19), pp.3195-3197.
- [1.23] Zhang, C., Maslov, K., Hu, S., Chen, R., Zhou, Q., Shung, K.K. and Wang, L.V., 2012. Reflection-mode submicron-resolution in vivo photoacoustic microscopy. *Journal of biomedical optics*, 17(2), pp.0205011-0205014.
- [1.24] Zhang, C., Maslov, K., Yao, J. and Wang, L.V., 2012. In vivo photoacoustic microscopy with 7.6- μm axial resolution using a commercial 125-MHz ultrasonic transducer. *Journal of biomedical optics*, 17(11), pp.116016-116016.
- [1.25] Nedosekin, D.A., Galanzha, E.I., Dervishi, E., Biris, A.S. and Zharov, V.P., 2014. Super-Resolution Nonlinear Photothermal Microscopy. *Small*, 10(1), pp.135-142.
- [1.26] Yao, J., Wang, L., Li, C., Zhang, C. and Wang, L.V., 2014. Photoimprint photoacoustic microscopy for three-dimensional label-free subdiffraction imaging. *Physical review letters*, 112(1), p.014302.
- [1.27] Yang, J.M., Li, C., Chen, R., Rao, B., Yao, J., Yeh, C.H., Danielli, A., Maslov, K., Zhou, Q., Shung, K.K. and Wang, L.V., 2015, March. Label-free optical-resolution photoacoustic endomicroscopy in vivo. In *SPIE BiOS* (pp. 932332-932332). International Society for Optics and Photonics.
- [1.28] Yang, J.M., Li, C., Chen, R., Rao, B., Yao, J., Yeh, C.H., Danielli, A., Maslov, K., Zhou, Q., Shung, K.K. and Wang, L.V., 2015. Optical-resolution photoacoustic endomicroscopy in vivo. *Biomedical optics express*, 6(3), pp.918-932.
- [1.29] Chen, S.L., Xie, Z., Guo, L.J. and Wang, X., 2013. A fiber-optic system for dual-modality photoacoustic microscopy and confocal fluorescence microscopy using miniature components. *Photoacoustics*, 1(2), pp.30-35.
- [1.30] Yang, J.M., Favazza, C., Chen, R., Yao, J., Cai, X., Maslov, K., Zhou, Q., Shung, K.K. and Wang, L.V., 2012. Simultaneous functional photoacoustic and ultrasonic endoscopy of internal organs in vivo. *Nature medicine*, 18(8), pp.1297-1302.
- [1.31] Aljaseem, Khaled, et al. Scanning and tunable micro-optics for endoscopic optical coherence tomography. *Microelectromechanical Systems, Journal of* 20.6 (2011): 1462-1472.

- [1.32] Z. Qiu, S. Khondee, X. Duan, H. Li, M.J. Mandella, B.P. Joshi, Q. Zhou, S.R. Owens, K. Kurabayashi, K.R. Oldham, T.D. Wang, Vertical cross-sectional imaging of colonic dysplasia in vivo with multi-spectral dual axes confocal endomicroscopy, *Gastroenterology* 146 (3) (2014) 615–617.
- [1.33] Zhang X, Duan C, Liu L, Li X, Xie H. A non-resonant fiber scanner based on an electrothermally-actuated MEMS stage. *Sensors and Actuators A: Physical*. 2015 Sep 1;233:239-45.
- [1.34] Li, H., Duan, X., Qiu, Z., Zhou, Q., Kurabayashi, K., Oldham, K.R. and Wang, T.D., 2016. Integrated monolithic 3D MEMS scanner for switchable real time vertical/horizontal cross-sectional imaging. *Optics express*, 24(3), pp.2145-2155.
- [1.35] Grade, J. D., Jerman, H. & Kenny, T. W. Design of large deflection electrostatic actuators. *Journal of Microelectromechanical Systems* 12, 335-343, doi:10.1109/jmems.2003.811750 (2003).
- [1.36] Werber, A. & Zappe, H. Thermo-pneumatically actuated, membrane-based micro-mirror devices. *Journal of Micromechanics and Microengineering* 16, 2524-2531, doi:10.1088/0960-1317/16/12/002 (2006).
- [1.37] Cho I-J and Yoon E 2009 A low-voltage three-axis electromagnetically actuated micromirror for fine alignment among optical devices *Journal of Micromechanics and Microengineering* 19 085007
- [1.38] Wu, Y., Zhang, Y., Xi, J., Li, M.J. and Li, X., 2010. Fiber-optic nonlinear endomicroscopy with focus scanning by using shape memory alloy actuation. *Journal of biomedical optics*, 15(6), pp.060506-060506.
- [1.39] Gilchrist K H, Dausch D E and Grego S 2012 Electromechanical performance of piezoelectric scanning mirrors for medical endoscopy *Sensors and Actuators a-Physical* 178 193-201
- [1.40] Qian R, Wen Z and Chen L 2011 A Piezoelectrically Actuated Scanning Micromirror Integrated with Angle Sensors *Mems/Nems Nano Technology* 483 437-42
- [1.41] Tani M, Akamatsu M, Yasuda Y, Toshiyoshi H and Lee 2007 A two-axis piezoelectric tilting micromirror with a newly developed PZT-Meandering actuator. In: 20th IEEE International Conference on Micro Electro Mechanical Systems (MEMS 2007), (Kobe, JAPAN) pp 140-3

- [1.42] Milanovic V, Matus G A and McCormick D T 2004 Gimbal-less monolithic silicon actuators for tip-tilt-piston micromirror applications *IEEE Journal of Selected Topics in Quantum Electronics* 10 462-71
- [1.43] He S, Ben Mrad R and Chong J 2011 Repulsive-force out-of-plane large stroke translation micro electrostatic actuator *Journal of Micromechanics and Microengineering* 21
- [1.44] Weber N, Hertkorn D, Zappe H and Seifert A 2012 Polymer/Silicon Hard Magnetic Micromirrors *Journal of Microelectromechanical Systems* 21 1098-106
- [1.45] Baba A, Okano H, Uetsuka H, Esashi M and Ieee 2003 2 axes optical switch with holding mechanism. In: 16th IEEE Annual International Conference on Micro Electro Mechanical Systems, (Kyoto, Japan) pp 251-4
- [1.46] Jia K, Pal S and Xie H 2009 An Electrothermal Tip-Tilt-Piston Micromirror Based on Folded Dual S-Shaped Bimorphs *Journal of Microelectromechanical Systems* 18 1004-15
- [1.47] Naono T, Fujii T, Esashi M and Tanaka S 2014 A large-scan-angle piezoelectric MEMS optical scanner actuated by a Nb-doped PZT thin film *Journal of Micromechanics and Microengineering* 24 015010
- [1.48] Curie J, Curie P. Développement, par pression, de l'électricité polaire dans les cristaux hémihédres à faces inclinées. (in French) *Comptes Rendus de l'Académie des Sciences*. 1880;91:294–5.
- [1.49] Curie J, Curie P. Sur l'électricité polaire dans les cristaux hémihédres à faces inclinées. (in French) *C R Acad Sci Gen*. 1880;91:383–6.
- [1.50] Curie J, Curie P. Contractions et dilatations produites par des tensions dans les cristaux hémihédres à faces inclinées. (in French) *C R Acad Sci Gen*. 1880;93:1137–40.
- [1.51] G. Lippman, "Principe de la conservation de l'électricité" (in French) *Annales de chimie et de physique*, Vol. 24, p. 145, 1881.
- [1.52] Kholkin, A.L., Pertsev, N.A. and Goltsev, A.V., 2008. Piezoelectricity and crystal symmetry. In *Piezoelectric and Acoustic Materials for Transducer Applications* (pp. 17-38). Springer US.
- [1.53] www.physikinstrumente.com, tutorial: fundamentals of piezoelectricity

- [1.54] Gualtieri, J.G., Kosinski, J.A. and Ballato, A., 1994. Piezoelectric materials for acoustic wave applications. *IEEE transactions on ultrasonics, ferroelectrics, and frequency control*, 41(1), pp.53-59.
- [1.55] Carlotti, G., et al. Elastic constants of sputtered ZnO films. *IEEE 1987 Ultrasonics Symposium*. IEEE, 1987.
- [1.56] Dubois, M.A. and Muralt, P., 1999. Properties of aluminum nitride thin films for piezoelectric transducers and microwave filter applications. *Applied Physics Letters*, 74(20), pp.3032-3034.
- [1.57] Ledermann, N., Muralt, P., Baborowski, J., Gentil, S., Mukati, K., Cantoni, M., Seifert, A. and Setter, N., 2003. {1 0 0}-textured, piezoelectric Pb (Zr x, Ti 1- x) O 3 thin films for MEMS: integration, deposition and properties. *Sensors and Actuators A: Physical*, 105(2), pp.162-170.
- [1.58] Hishinuma, Y., Fujii, T., Naono, T., Arakawa, T. and Li, Y., 2015, May. Recent progress on development of sputtered PZT film at FUJIFILM. In *2015 Joint IEEE International Symposium on the Applications of Ferroelectric (ISAF), International Symposium on Integrated Functionalities (ISIF), and Piezoelectric Force Microscopy Workshop (PFM)* (pp. 288-291). IEEE.
- [1.59] Fujii, T., Naono, T., Mukaiyama, A., Arakawa, T., Hishinuma, Y., Li, Y. and Birkmeyer, J., Preparation of Nb-doped PZT Thin Film with High Piezoelectric Performance and Its Application to MEMS Devices.
- [1.60] Baek, S.H., Park, J., Kim, D.M., Aksyuk, V.A., Das, R.R., Bu, S.D., Felker, D.A., Lettieri, J., Vaithyanathan, V., Bharadwaja, S.S.N. and Bassiri-Gharb, N., 2011. Giant piezoelectricity on Si for hyperactive MEMS. *Science*, 334(6058), pp.958-961.
- [1.61] Zhang, R., Jiang, B. and Cao, W., 2001. Elastic, piezoelectric, and dielectric properties of multidomain 0.67 Pb (Mg^{1/3}Nb^{2/3}) O₃-0.33 PbTiO₃ single crystals. *Journal of Applied Physics*, 90(7), pp.3471-3475.
- [1.62] Zhang, R., Jiang, B. and Cao, W., 2001. Elastic, piezoelectric, and dielectric properties of multidomain 0.67 Pb (Mg^{1/3}Nb^{2/3}) O₃-0.33 PbTiO₃ single crystals. *Journal of Applied Physics*, 90(7), pp.3471-3475.

- [1.63] Arai, S., Wilson, S.A., Corbett, J. and Whatmore, R.W., 2009. Ultra-precision grinding of PZT ceramics—Surface integrity control and tooling design. *International Journal of Machine Tools and Manufacture*, 49(12), pp.998-1007.
- [1.64] Aktakka, E.E., Peterson, R.L. and Najafi, K., 2011, June. Thinned-PZT on SOI process and design optimization for piezoelectric inertial energy harvesting. In 2011 16th International Solid-State Sensors, Actuators and Microsystems Conference (pp. 1649-1652). IEEE.
- [1.65] Aktakka, E.E., Kim, H. and Najafi, K., 2009, June. Wafer level fabrication of high performance MEMS using bonded and thinned bulk piezoelectric substrates. In TRANSDUCERS 2009-2009 International Solid-State Sensors, Actuators and Microsystems Conference (pp. 849-852). IEEE.
- [1.66] Aktakka, E.E., Peterson, R.L. and Najafi, K., 2013. Wafer-level integration of high-quality bulk piezoelectric ceramics on silicon. *IEEE Transactions on Electron Devices*, 60(6), pp.2022-2030.
- [1.67] Furukawa, E., Mizuno, M. and Doi, T., 1995. Development of a flexure-hinged translation mechanism driven by two piezoelectric stacks. *JSME international journal. Ser. C, Dynamics, control, robotics, design and manufacturing*, 38(4), pp.743-748.
- [1.68] EDO Corporation. *Piezoelectric Ceramics: Material Specifications, Typical Applications*. 2645 South 300 West, Salt Lake City, UT. No date
- [1.69] Prechtel, E.F. and Hall, S.R., 1997, June. Design of a high-efficiency discrete servo-flap actuator for helicopter rotor control. In *Smart Structures and Materials' 97* (pp. 158-182). International Society for Optics and Photonics.
- [1.70] Brei, D., Berner, N.T. and Alexander, P.W., 2001. Modeling and study of the quasi-static behavior of piezoceramic telescopic actuation architectures. *Journal of intelligent material systems and structures*, 12(5), pp.303-313.
- [1.71] Moskalik, A. and Brei, D., 1996. Force-Deflection Behavior of Individual Piezoceramic C-Block Actuators. In *Proceedings of the ASME 1996 International Mechanical Engineering Congress and Exposition*.
- [1.72] Wise, S.A., 1998. Displacement properties of RAINBOW and THUNDER piezoelectric actuators. *Sensors and Actuators A: Physical*, 69(1), pp.33-38.

- [1.73] Kugel, V.D., Chandran, S. and Cross, L.E., 1997, February. Comparative analysis of piezoelectric bending-mode actuators. In Smart Structures and Materials' 97 (pp. 70-80). International Society for Optics and Photonics.
- [1.74] Sugawara, Y., Onitsuka, K., Yoshikawa, S., Xu, Q., Newnham, R.E. and Uchino, K., 1992. Metal–ceramic composite actuators. *Journal of the American Ceramic Society*, 75(4), pp.996-998.
- [1.75] Onitsuka, K., Dogan, A., Tressler, J.F., Xu, Q., Yoshikawa, S. and Newnham, R.E., 1995. Metal-Ceramic Composite Transducer, the " Moonie". *Journal of Intelligent Material Systems and Structures*, 6(4), pp.447-455.
- [1.76] Kugel, V.D., Chandran, S. and Cross, L.E., 1997, February. Comparative analysis of piezoelectric bending-mode actuators. In Smart Structures and Materials' 97 (pp. 70-80). International Society for Optics and Photonics.
- [1.77] Near, C.D., 1996, May. Piezoelectric actuator technology. In 1996 Symposium on Smart Structures and Materials (pp. 246-258). International Society for Optics and Photonics.
- [1.78] Ervin, J.D. and Brei, D., 1998. Recurve piezoelectric-strain-amplifying actuator architecture. *IEEE/ASME transactions on mechatronics*, 3(4), pp.293-301.

CHAPTER 2: FIRST GENERATION PIEZOELECTRIC ACTUATOR

2. 2. Actuator Design and Static Modeling

2. 2. 1. Actuator Geometry and Working Principle

The proposed scanners are developed based on previous work [2.1], where four identical thin-film lead-zirconate-titanate (PZT) unimorphs were used for vertical actuation of the stage as shown in Figure 2.1. These previously developed scanners have shown a static out-of-plane displacement of as much as 120 μm with a natural frequency of about 200 Hz. In order to amplify the out-of-plane displacement to at least 400 μm , each leg of the scanners has been redesigned to have four symmetric thin-film PZT bending beams arranged in series, forming a folded-leg geometry, to actuate their central scanning stage (Figure 2.2). A scanning mirror or lens may be incorporated to the stage.

In this design, each leg consists of four unimorph beams connected in a serpentine pattern. An even number of beams in each leg minimizes possible lateral shift in the x-y plane due to the lateral motion generated at the end of each beam. Each unimorph has two segments; one with a gold layer on top and the other without it, as shown in Figure 2.3. The segment without the gold layer has its neutral bending axis below the mid-plane of the PZT layer, and thus it bends upwards when the PZT layer contracts under applied electric field. On the other hand, the segment with the gold layer, with its neutral bending axis above the mid-plane of the PZT layer,

bends downwards when the PZT layer contracts. Hence, each unimorph of a leg bends in an S-shape in reaction to the applied electric field.

The bending profile of this design is similar to that of the Recurve architecture developed for bulk piezoelectric materials [1.78]. The Recurve actuator uses bimorph elements whose electrical connections allow one piezoelectric layer to contract while the other to expand to produce bend-up and down segments. However, as mentioned earlier, this strategy is not as effective in thin-film piezoelectrics because small negative voltages can easily generate reverse coercive fields, imparting a very small range of voltages for the d_{31} expansion mode. Thus, relatively thick material is deposited on portions of the thin-film piezoelectric composites to shift the neutral bending axis and obtain a vertical motion without tilting of their tip in the d_{31} contraction mode.

When all the legs or two diagonal legs of the scanner are actuated together, the actuators produce vertical translational motion (in the z-axis direction). When two adjacent legs are actuated simultaneously, they produce tilting motions (about x-axis and y-axis). Because thin-film piezoelectrics operate in contraction except for a small range of negative voltages and are sensitive to re-poling if voltage directions are reversed, tilting motion using differential voltages between pairs of legs is not generally advantageous. The ability to produce relatively large static tilt angle in different directions can be very useful for surgical or biopsy guidance and for adjusting for optical misalignments in miniature imaging instruments.

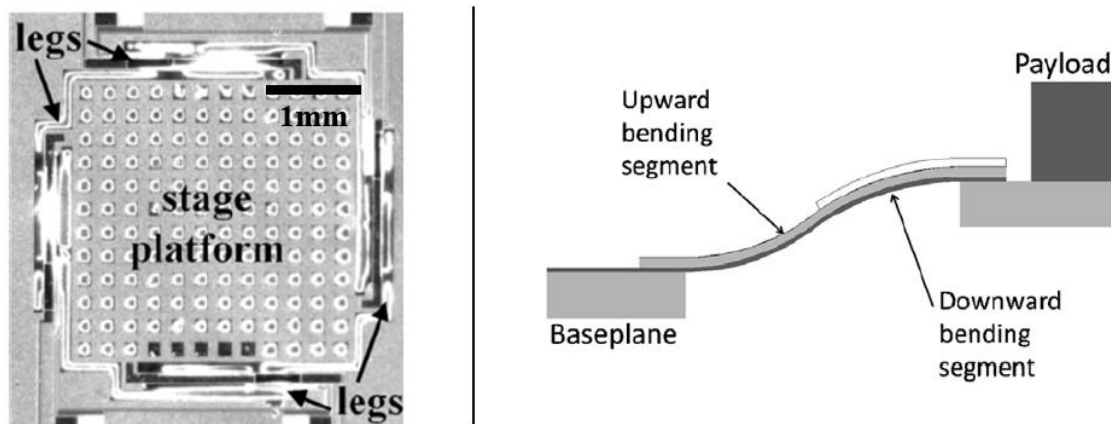


Figure 2.1. Left: piezoelectrically actuated vertical stage (top view); Right: schematic cross-section of a vertical translational stage [2.1]

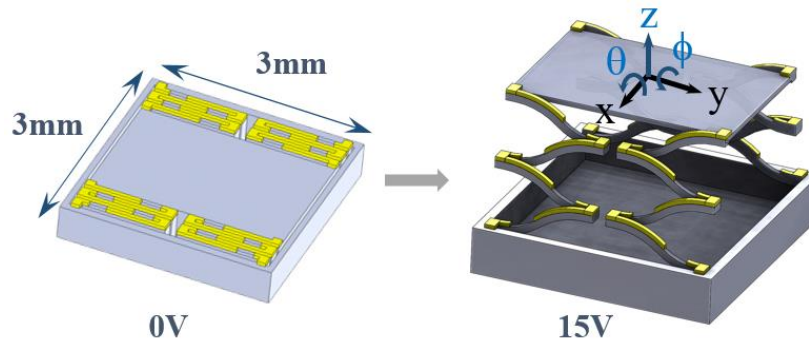


Figure 2.2. Proposed 3DOF micro-scanner design (actuatable directions in blue font)

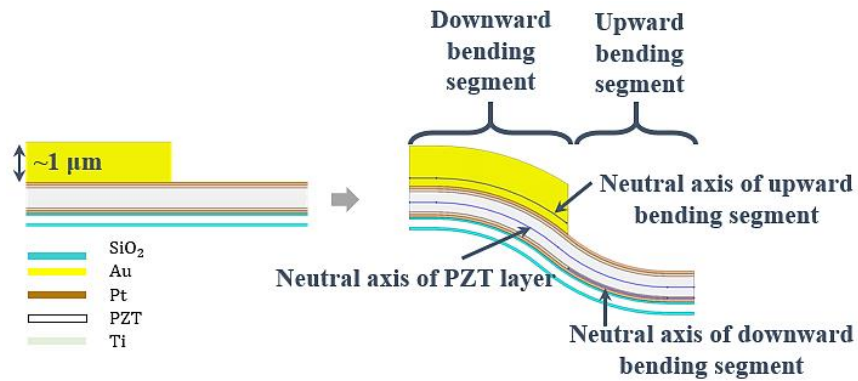


Figure 2.3. Schematic drawing of a unimorph bending in an S-shape

2. 2. 2. Static Modeling for Design

To achieve the required performance of the actuator in the limited footprint available, design trade-offs were identified, initially through a static model of the stage described in this section. The scanner of this work uses the thin-film PZT bending beam as its main component for actuation. Presented in this section are analytical expressions first for the deflection of a single unimorph beam and for the deflection of a single leg, which consists of four unimorphs, and then for the motion of the stage.

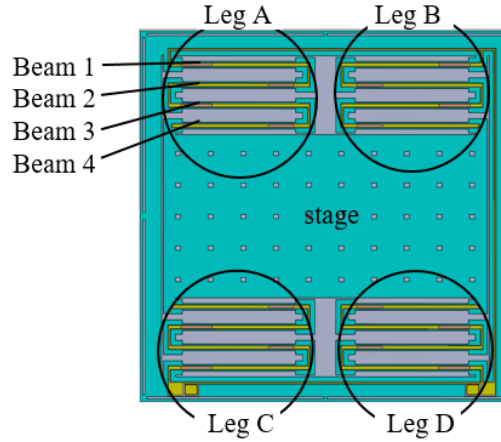


Figure 2.4. Notation for Beams and Legs

2. 2. 2. 1. Modeling of thin-film PZT unimorph

When an electric field is applied across the PZT layer, it contracts, or generate strain, which is called a converse piezoelectric effect. This converse effect can be used for actuators and is governed by the following constitutive equation written in Voigt notation,

$$\begin{bmatrix} \epsilon_1 \\ \epsilon_2 \\ \epsilon_3 \\ \epsilon_4 \\ \epsilon_5 \\ \epsilon_6 \end{bmatrix} = \begin{bmatrix} s_{11} & s_{12} & s_{13} & 0 & 0 & 0 \\ s_{12} & s_{22} & s_{23} & 0 & 0 & 0 \\ s_{13} & s_{23} & s_{33} & 0 & 0 & 0 \\ 0 & 0 & 0 & s_{44} & 0 & 0 \\ 0 & 0 & 0 & 0 & s_{55} & 0 \\ 0 & 0 & 0 & 0 & 0 & s_{66} \end{bmatrix} \begin{bmatrix} \sigma_1 \\ \sigma_2 \\ \sigma_3 \\ \sigma_4 \\ \sigma_5 \\ \sigma_6 \end{bmatrix} + \begin{bmatrix} 0 & 0 & d_{31} \\ 0 & 0 & d_{32} \\ 0 & 0 & d_{33} \\ 0 & d_{24} & 0 \\ d_{15} & 0 & 0 \\ 0 & 0 & 0 \end{bmatrix} \begin{bmatrix} E_1 \\ E_2 \\ E_3 \end{bmatrix} \quad (\text{Eq. 2.1})$$

where ϵ_i is the induced strain, s_{ij} compliance of the material measured with no applied electric field, σ_j stress, d_{mn} piezoelectric strain coefficients, and E_n electric field. Assuming free out-of-plane stress, PZT isotropy in the plane, and perfect clamping condition, the piezoelectric in-plane stress for a thin-film composite is expressed as follows [2.1, 2.2]:

$$\sigma_1 = -\frac{d_{31}E_3}{s_{11}+s_{12}} = -e_{31,eff}(V)E_3 \approx -d_{31,eff}(V)Y_{PZT}E_3 \quad (\text{Eq. 2.2})$$

where s_{13}^E and s_{33}^E are nominal (short circuit) compliances; d_{33} and d_{31} , piezoelectric coefficients; Y_{PZT} , the nominal elastic modulus; $d_{31,eff}$, effective electro-active piezoelectric strain coefficient

of the PZT; E_3 , the applied electric field. Due to very large electric field that thin-film PZT experiences, it exhibits nonlinear behaviors such as electrostriction. The nonlinear behaviors of PZT and linear piezoelectric effects are lumped in the effective electro-active piezoelectric strain coefficient as a function of voltage. By modeling using the effective electro-active piezoelectric strain coefficient, the change of the elastic modulus of PZT is also lumped into $d_{31,eff}$. There is likely a voltage dependence to Y_{PZT} as well, but to our current ability to measure this effect is small and neglected in our analysis.

The in-plane stress produces a force, which can be designed to be applied above or below the neutral bending axis of each segment of the beam, making the beam bend in an S-shape (Figure 2.3). Using this expression, the moment generated on each segment by the contraction of the PZT layer can be described as follows:

$$M_{UP} = -d_{31,eff}(V)Y_{PZT} \frac{V}{t_{PZT}} A_{PZT} (\bar{z}_{PZT} - \bar{z}_{UP}) \quad (\text{Eq. 2.3})$$

$$M_{DN} = -d_{31,eff}(V)Y_{PZT} \frac{V}{t_{PZT}} A_{PZT} (\bar{z}_{DN} - \bar{z}_{PZT}) \quad (\text{Eq. 2.4})$$

where M_{UP} and M_{DN} are moments produced on the upward bending segment and the downward bending segment, respectively. t_{PZT} , A_{PZT} , \bar{z}_{PZT} are the thickness, cross-sectional area, and midline of the PZT layer, respectively. V is the applied voltage across the PZT layer ($E_3=V/t_{PZT}$), and \bar{z}_{UP} and \bar{z}_{DN} are the neutral axes of the respective composite segment.

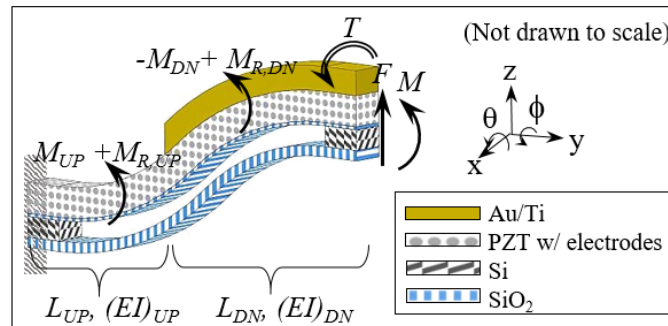


Figure 2.5. Free body diagram of Beam 1

The free body diagram of Beam 1, the closest beam to the outer frame of the scanner following the definitions described in Figure 2.4, is shown in Figure 2.5. In addition to bending moments generated by the PZT (M_{UP} , M_{DN}), the beam is assumed to experience residual stress ($M_{R,UP}$, $M_{R,DN}$) on each segment as well as an external force (F), bending moment (M), and torsion (T), which are all estimated to have effect at its tip. Compressive residual stress is developed during fabrication when the scanner undergoes different high-temperature etching and deposition processes. Now the moment that the composite beam experiences at a position y along its length direction can be described as the sum of all the external and internal moments:

$$M(y) = \begin{cases} M_{UP} + M_{R,UP} + (L_{UP} + L_{DN} - y)F + M & \text{for } (0 < y \leq L_{UP}) \\ -M_{DN} + M_{R,DN} + (L_{UP} + L_{DN} - y)F + M & \text{for } (L_{UP} < y \leq L_{UP} + L_{DN}) \end{cases} \quad (\text{Eq. 2.5})$$

where L_{UP} and L_{DN} are the lengths of the portion of the beam without and with the additional gold layer, respectively. This moment expression can be integrated to find the deflection and slope at the tip of the beam. The torsional displacement at the tip of the beam, ϕ_L , caused by the torsion T , can be written as follows:

$$\frac{(L_{UP} + L_{DN})T}{(GJ)_{comp}} = \phi_L \quad (\text{Eq. 2.6})$$

where $(GJ)_{comp}$ is the beam's torsional rigidity.

Now one can write the twisting and tilting angles (or slope) and deflections of a single beam at the tip, given an initial tilting angle, ϕ_0 , slope, θ_0 , and beam deflection, z_0 in a matrix form as follows:

$$\begin{bmatrix} \phi \\ \theta \\ z \end{bmatrix} = \tilde{S}_{ext} \begin{bmatrix} T \\ M \\ F \end{bmatrix} + \tilde{S}_{int} d_{31,eff}(V)V + \tilde{P} \begin{bmatrix} \phi_0 \\ \theta_0 \\ z_0 \end{bmatrix} + \tilde{R} \begin{bmatrix} M_{R,UP} \\ M_{R,DN} \end{bmatrix} \\ := \tilde{S}_{ext} \bar{F} + \tilde{S}_{int} d_{31,eff}(V)V + \tilde{P} \bar{X}_0 + \tilde{R} \bar{M}'_R \quad (\text{Eq. 2.7})$$

\tilde{S}_{ext} corresponds to a compliance matrix for the composite beam; \tilde{S}_{int} , a force-mapping matrix relating the input voltage to the tip displacements; \tilde{P} , a geometric mapping accounting for the contribution of its boundary (initial) positions to the tip of the beam; \tilde{R} , mapping from residual stress to beam displacements. Each matrix is defined in Appendix A.1.

2. 2. 2. 2. Modeling of PZT bending leg

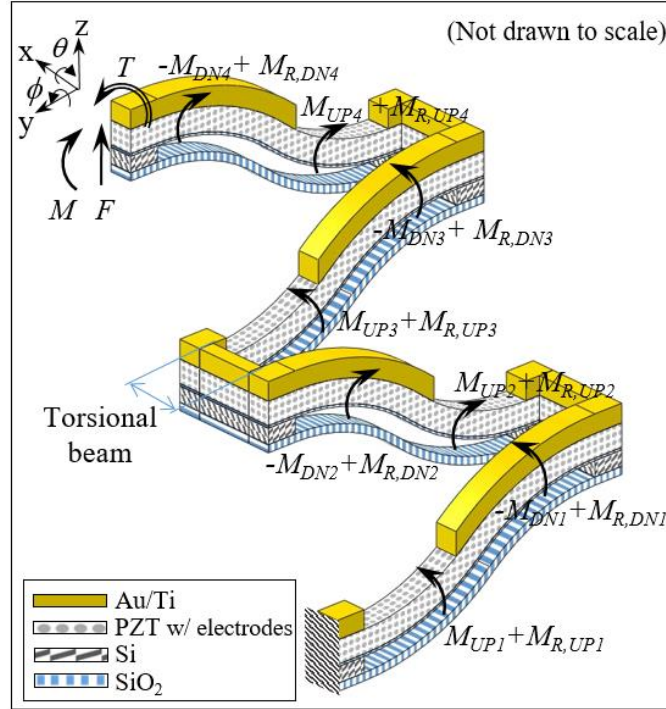


Figure 2.6. Free body diagram of a Leg

Each leg is composed of four composite beams connected by rigid silicon links in a serpentine pattern. The silicon links, also referred to as torsional beams in Figure 2.6, are assumed to be too stiff to be bent due to a force or moment, but allowed to be twisted by a torsion. If all external forces, moments, and torsions acting on a leg are combined as one effective force, moment, and torsion at the end of the leg, one can calculate the effects of the external loadings on each beam within the leg. Then, using the expression for the angular and translational displacements developed in the previous section in terms of external forces, piezoelectric force, boundary positions, and residual stress (Eq. 2.7), the displacement of a full leg can be computed by summing up the displacements of individual beams. After the compilation of the displacements

of the four individual beams, the expression for the tip position of a leg can be grouped in the following manner:

$$\begin{aligned} \begin{bmatrix} \phi^i \\ \theta^i \\ z^i \end{bmatrix} &= S_{ext} \begin{bmatrix} T^i \\ M^i \\ F^i \end{bmatrix} + S_{int} d_{31,eff}(V)V + \sum_{j=1}^4 R_j \begin{bmatrix} M_{R,UPj} \\ M_{R,DNj} \end{bmatrix} \\ &:= S_{ext} \bar{F}^i + S_{int} d_{31,eff}(V)V + R \bar{M}_R \end{aligned} \quad (\text{Eq. 2.8})$$

where the superscript i denotes the leg number ($i=A, B, C, D$) and the subscript j the beam number ($j=1, 2, 3, 4$), as defined in Figure 2.4. Similar to the expression for a single beam, the tip position of a leg is also expressed in terms of the applied external force, voltage, and each segment's residual stress. Matrices in equation (2.8) are defined in Appendix A.2. S_{ext} and S_{int} matrices define beam compliance. The effective residual moment is allowed to vary from one segment to the other even within the same leg as observed in the prototype scanners.

2. 2. 2. 3. Modeling of stage motion

Now that the equation for leg displacements is obtained, if the forces and moments acting on the stage as well as reaction forces, moments, and torsions between the stage and each leg identified, the overall stage motion can be found.

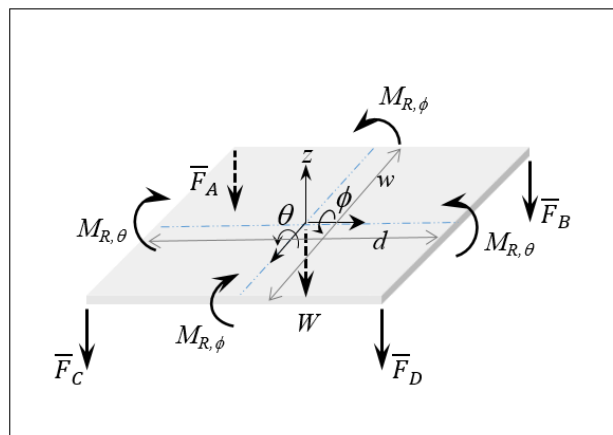


Figure 2.7 Free body diagram of the stage

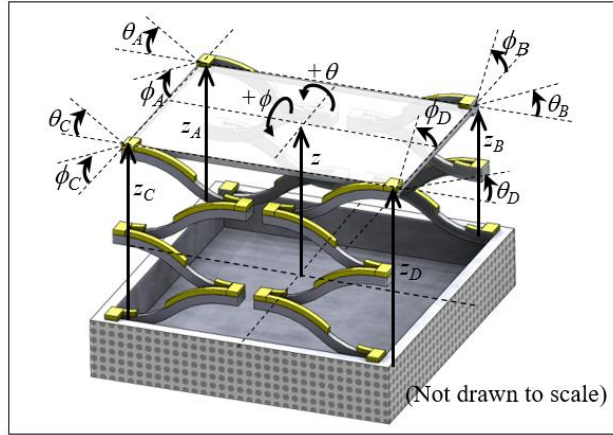


Figure 2.8. Definitions of angles and displacements

Figure 2.7 shows the free body diagram of the stage, where the reaction force, moment, and torsion for each leg are represented as a vector, \bar{F}_i (the subscript $i=A, B, C, D$ indicates each leg), and the gravity force is denoted by W . The reaction moment and torsion acting on each corner of the stage are in the negative direction, opposite to the directions defined in Figure 2.8, because the counterpart moment and torsion acting on the leg are defined in the positive angle directions. If the residual stresses on the stage are assumed to only affect its initial deflections in two directions, the effects of the residual stresses can be approximated using effective moments, $M_{R,\theta}$ and $M_{R,\phi}$. Using Newton's 2nd law, the equation of motion for the stage can be written as the following.

$$\begin{aligned} \begin{bmatrix} J_\phi & 0 & 0 \\ 0 & J_\theta & 0 \\ 0 & 0 & m \end{bmatrix} \begin{bmatrix} \ddot{\theta} \\ \ddot{\phi} \\ \ddot{z} \end{bmatrix} &= \sum_{i=A,B,C,D} P_n^i \begin{bmatrix} T^i \\ M^i \\ F^i \end{bmatrix} + \begin{bmatrix} 0 \\ 0 \\ -mg \end{bmatrix} \\ &:= \ddot{J}\bar{X} = P_n^A \bar{F}^A + P_n^B \bar{F}^B + P_n^C \bar{F}^C + P_n^D \bar{F}^D - \bar{W} \quad (\text{Eq. 2.9}) \end{aligned}$$

$$\text{where } P_n^A := \begin{bmatrix} 1 & 0 & -\frac{w}{2} \\ 0 & 1 & \frac{d}{2} \\ 0 & 0 & -1 \end{bmatrix}, P_n^B := \begin{bmatrix} -1 & 0 & -\frac{w}{2} \\ 0 & -1 & -\frac{d}{2} \\ 0 & 0 & -1 \end{bmatrix}, P_n^C := \begin{bmatrix} 1 & 0 & \frac{w}{2} \\ 0 & 1 & \frac{d}{2} \\ 0 & 0 & -1 \end{bmatrix}, P_n^D := \begin{bmatrix} -1 & 0 & \frac{w}{2} \\ 0 & -1 & -\frac{d}{2} \\ 0 & 0 & -1 \end{bmatrix},$$

$$\bar{W} := \begin{bmatrix} 0 \\ 0 \\ mg \end{bmatrix}$$

P_n^i (i=A, B, C, D) matrices describe how the torsion, moment, and force from each leg affect the stage motion.

Due to the physical constraints between the legs and the stage, the position of the stage and that of the tip of each leg have the following relationship:

$$\bar{X}^i = [\phi^i \ \theta^i \ z^i]^T = T_n^i \bar{X} + T_{2,n} M_{R,\theta} + T_{3,n}^i M_{R,\phi} \quad (\text{Eq. 2.10})$$

Residual stresses on the stage that affect the legs' initial displacements are accounted for by the last two terms in Eq. 2.10. The matrices $T_{2,n}$ and $T_{3,n}^i$ relate the effective residual moments, $M_{R,\theta}$ and $M_{R,\phi}$ in the θ and ϕ directions, respectively, to the initial stage deflections (*i.e.* at 0V). The definitions of T^i (i=A, B, C, D), T_2 , T_3^i matrices are below.

$$T_n^A := \begin{bmatrix} -1 & 0 & 0 \\ 0 & -1 & 0 \\ \frac{w}{2} & -\frac{d}{2} & 1 \end{bmatrix}, T_n^B := \begin{bmatrix} 1 & 0 & 0 \\ 0 & 1 & 0 \\ \frac{w}{2} & \frac{d}{2} & 1 \end{bmatrix}, T_n^C := \begin{bmatrix} -1 & 0 & 0 \\ 0 & -1 & 0 \\ -\frac{w}{2} & -\frac{d}{2} & 1 \end{bmatrix}, T_n^D := \begin{bmatrix} 1 & 0 & 0 \\ 0 & 1 & 0 \\ -\frac{w}{2} & \frac{d}{2} & 1 \end{bmatrix}$$

$$T_{2,n} := \begin{bmatrix} 0 \\ \frac{d}{2EI_{stg}} \\ \frac{(d)^2}{8EI_{stg}} \end{bmatrix}, T_{3,n}^i := \begin{bmatrix} (-1)^m \frac{w}{2EI_{stg}} \\ 0 \\ \frac{(w)^2}{8EI_{stg}} \end{bmatrix}, \quad m=1 \text{ for } i=A \text{ and } D, \quad n=2 \text{ for } i=B \text{ and } C.$$

Using the expressions for physical relationship between the legs and the stage (Eq. 2.10) and for the leg position (Eq. 2.8), the reaction forces, moments, and torsions can be solved and written in terms of residual moments, piezoelectric forcing, and importantly the stage position.

$$\bar{F}^i = (S_{ext}^i)^{-1} \left(T_n^i \bar{X} + T_{2,n} M_{R,\theta} + T_{3,n}^i M_{R,\phi} - S_{int}^i d_{31,eff}(V) V^i - \bar{M}_R^i \right) \quad (\text{Eq. 2.11})$$

The expression above can be plugged into the stage's static equation of motion, *i.e.* Eq. 2.9 set to zero, to describe the static motion of the center of the stage.

$$\sum_{i=A,B,C,D} (-1)^{P^i} (S_{ext}^i)^{-1} T_n^i \bar{X} = d_{31,eff}(V) \sum_{i=A,B,C,D} \{(-1)^{P^i} (S_{ext}^i)^{-1} S_{int}^i V^i + \bar{M}_{res}^i\} + \bar{M}_{stg_{res}} - \bar{W} \quad (\text{Eq. 2.12})$$

Finally, Eq. 2.12 can be written in terms of the input voltage applied to each leg, effective residual moment, and gravity to describe the position of the center of the stage:

$$K_n \bar{X} = d_{31,eff}(V) V_{coef,n} \begin{bmatrix} V^A \\ V^B \\ V^C \\ V^D \end{bmatrix} + \bar{M}_{res,n} - \bar{W} \quad (\text{Eq. 2.13})$$

Now the contributions to the position of the stage are fully expressed. The initial position of the stage (when $V^A=V^B=V^C=V^D=0$) is due to the gravity and residual stresses, and when voltage is applied to each leg its displacements are related to the stiffness of the structure and piezoelectric forcing.

2. 2. 3. Design Trade-off Analysis

Now with a model that can predict the scanner's performance, design trade-offs between the displacement and natural frequency of the stage have been studied as some key geometric parameters were varied.

As expected, increase in the beam length results in increase in the displacement and decrease in the natural frequency as shown in Figure 2.9 (a). In this work, endoscope compatibility, *i.e.* available footprint (5mm in diameter), limits the beam length. Figure 2.9 (b) shows the influence of the ratio of the length of the downward bending segment to that of the upward bending segment on the displacement and natural frequency when the total length of the beam is fixed. The results suggest that when 50% of the total beam length is overlaid with gold the displacements are at their maximum. When the coverage is below 50%, the longer the downward bending segment is, the more slope (θ) it produces at its tip, which makes the next beam produce a larger displacement. On the other hand, when the coverage is above 50%, the longer the

downward bending segment is, the more it bends downward, ultimately decreasing the total displacement. As the gold coverage increases, it stiffens each beam, increasing the structural natural frequency of the stage.

Figure 2.9 (c) and (d) describe the effect of the thickness of the gold and PZT layers on the scanner performance, respectively. Thicker gold layer moves the neutral bending axis further away from the midline of the PZT layer, which means larger moment and thus displacement. However, if it is too thick, the bending beams become too stiff, resulting in less displacement. Thus, there exists an optimal thickness for the gold layer. As one can see from equations (2.3) and (2.4), moment generated by the PZT layer does not depend on the thickness of the PZT layer. As the PZT thickness decreases, the distance between the neutral bending axis and the midline of the PZT layer, or the “moment arm,” changes little, but the composite beam becomes less stiff. Then, under the same electric field, thinner PZT layer produces larger displacement, not considering the break-down voltage. If the PZT layer becomes too thin, its piezoelectric properties degrade, so figure 2.9 (d) shows an ideal case. The thickness of the PZT film of this work was decided to be $0.8\mu\text{m}$ as both the US Army research lab and Radiant technologies (NM, USA), from which films was provided, demonstrated good piezoelectric properties in that thickness. For the value of effective electro-active piezoelectric strain coefficient, $d_{31,\text{eff}}$, an experimentally extracted value from previous study was used [2.1]. Material properties and other conditions used to generate Figure 2.9 are listed in Table 2.1.

With the parameters listed in Table 2.1, the stiffness of the stage in the z-axis direction is about 0.03N/m . With a more compliant structure, larger displacement can be generated, but residual stress will deflect the bending legs more, and more likely residual stress would be non-uniform, causing undesired displacement mismatch and off-axis tilting motion. To increase the stiffness of the structure without sacrificing the displacement, the elastic layers can be made thicker, but the input voltage would approach the PZT breakdown voltage. The legs can be made wider instead, but the footprinted is limited. If the actuator needs to carry a mirror chip, a $30\mu\text{m}$ -thick silicon

chip coated with thin reflective material only requires about $0.6\mu\text{N}$, which minimally affects the displacement as shown in Figure 2.9 (e).

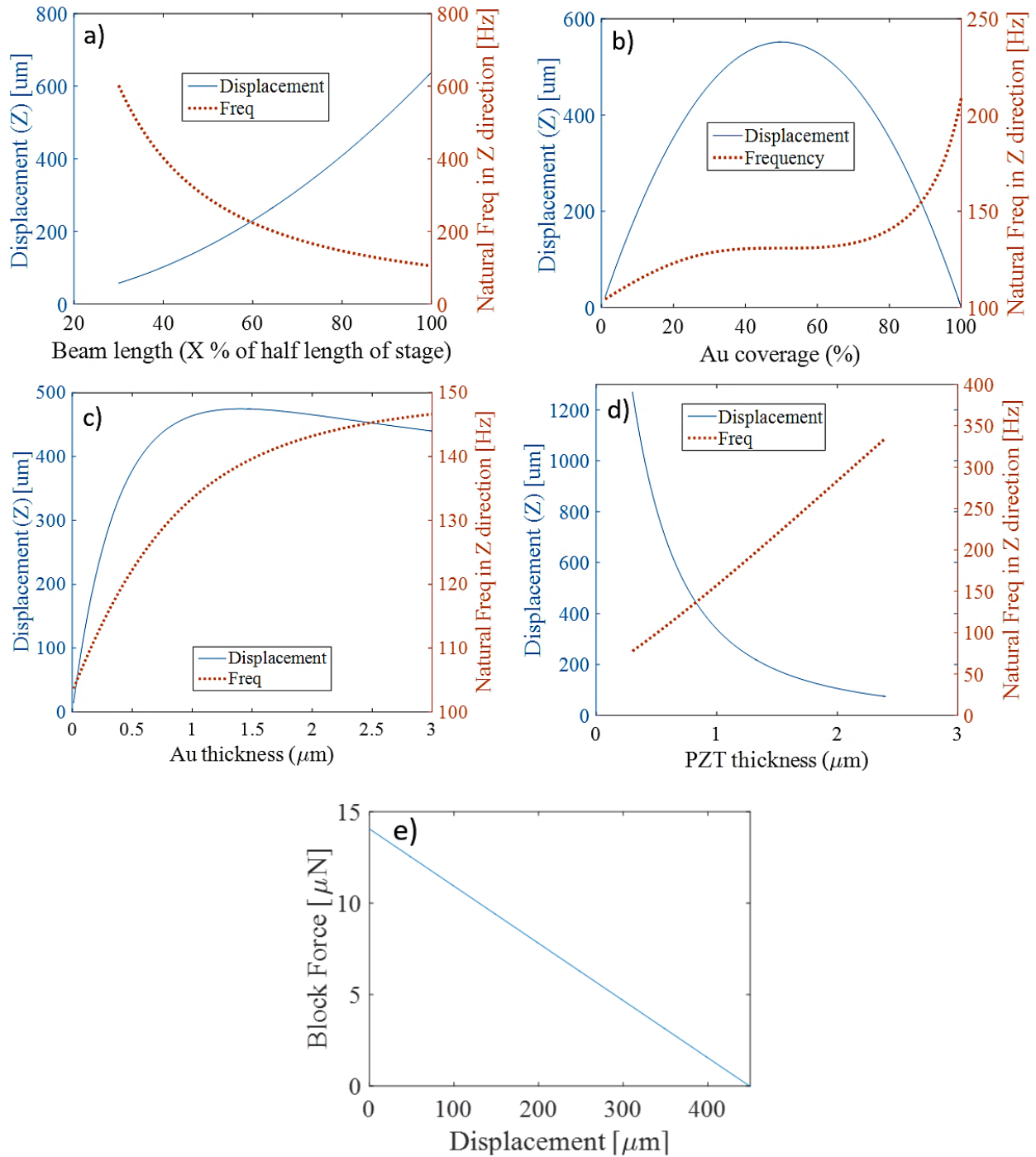


Figure 2.9. Predicted displacement and frequency of the center of the stage in Z direction at 15V (all the legs actuated) as (a) the beam length changes, (b) the Au coverage on each beam changes while its length is fixed, (c) the thickness of the Au layer changes, or (d) the thickness of the PZT layer changes; (e) stage displacement vs generative force

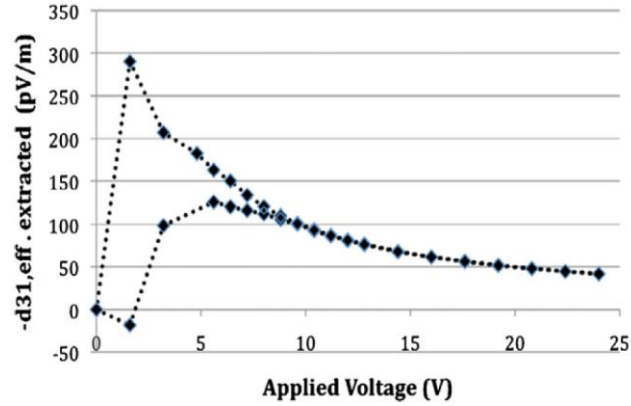


Figure 2.10. Experimentally extracted effective electro-active piezoelectric strain coefficient from previous generation batch [2.1]

Table 2.1. Material properties and dimensions used for design optimization

Property	Notation	Nominal Value (x)
<i>Film Thickness</i>		
Au+Ti layer	t_{Au}	1 μ m
Top Pt layer	$t_{Pt,top}$	0.105 μ m
PZT layer	t_{PZT}	0.8 μ m
Bottom Pt+Ti layer	$t_{Pt,btm}$	0.08 μ m
SiO ₂ layer	t_{SiO2}	0.5 μ m
<i>Elastic modulus of Film material [2.3-2.5]</i>		
Au+Ti	$E_{Au/Ti}$	86GPa
Pt	E_{Pt}	170GPa
PZT	E_{PZT}	70GPa
SiO ₂	E_{SiO2}	80GPa
<i>Beam Dimension</i>		
Width of beam	w	100 μ m
Length of segment w/o Au layer	L_{UP}	354 μ m
Length of segment w/ Au layer	L_{DN}	823 μ m
<i>Stage Property</i>		
Thickness of stage	thk_{stg}	10 μ m
Mass of stage	m	44.5 μ g
<i>Other Parameters</i>		
Applied voltage	V	15V
Eff. electro-active piezoelectric strain coef.	$d_{31,eff}$	-70pm/V [2.15]
Residual stress	-	0

Based on the results of this design trade-off study, prototype stage designs were chosen to maximize the beam length (*i.e.* half of the stage length) and to overlay 70% of the beam length in order to achieve a higher bandwidth than for the maximum displacement.

2. 3. Fabrication

The prototype actuators were fabricated based on a robust encapsulation fabrication process where silicon structures are completely protected by a layer of SiO₂ so that they can be preserved during the last releasing step of XeF₂ etching as reported in [2.6]. Compared to previous work [1.39-1.41, 1.47], this fabrication method allows the PZT unimorphs to generate larger out-of-plane displacement by removing the substrate silicon underneath the PZT film thus making the PZT bending beams more compliant.

As a summary of the process steps, narrow (3 μm wide) trenches defining the sidewalls of the silicon structures are firstly etched through the device layer of a SOI wafer by deep reactive ion etching (DRIE) as shown in Figure 2.11 (b). A series of deposition of SiO₂ by pressure chemical vapor deposition (LPCVD) and removal of SiO₂ by chemical mechanical polishing (CMP) and reactive ion etching (RIE) is repeated to reduce the size of the keyholes formed in SiO₂ trenches, while filling the trenches with SiO₂; Figure 2.11 (c). After the surface planarization, additional SiO₂ layer was deposited by plasma-enhanced chemical vapor deposition (PECVD) for a base layer (0.5 μm) for PZT, as depicted in Figure 2.11 (d).

To create a PZT and metal electrode stack, Ti/Pt (80 nm) is firstly sputtered onto the SiO₂ layer for the bottom electrode. A chemical solution process was used to deposit thin-film PZT (0.8 μm; Radiant Technologies, Inc.), and then Pt (0.1 μm) was sputtered. After the PZT stack is etched by ion milling and RIE, an Au (1μm) layer for the downward bending segment and bond pads is deposited by lift-off, as shown in Figure 2.11 (e).

To both define the actuator structures and create release trenches, a sequence of DRIE, RIE, and DRIE is used to etch the device silicon layer, buried SiO₂, and handle silicon layer, respectively, as illustrated in Figure 2.11 (f). Then, the handle silicon layer underneath the actuator structures is etched from the backside of the wafer using DRIE; Figure 2.11 (g). Lastly, XeF₂ is used to isotropically etch silicon underneath the PZT stack to release the actuator, as represented in Figure 2.11 (h). In this step, the silicon structures encapsulated in a layer of SiO₂ are preserved, which allows a longer etching time to ensure complete release of PZT beams without etching support structures of silicon, and thus increases device yield, compared to an earlier process used [2.1]. As mentioned earlier, the removal of the silicon device layer beneath the bottom electrode layer allows the unimorphs to achieve large bending deflections. The presence of the bottom SiO₂ layer—the buried SiO₂ layer of a silicon-on-insulator (SOI) wafer—is due to a limitation of the current fabrication process. However, this process allows the legs to have greater robustness during fabrication, compared to etching the buried SiO₂ and silicon layers underneath the PZT by a backside etch before releasing the device.

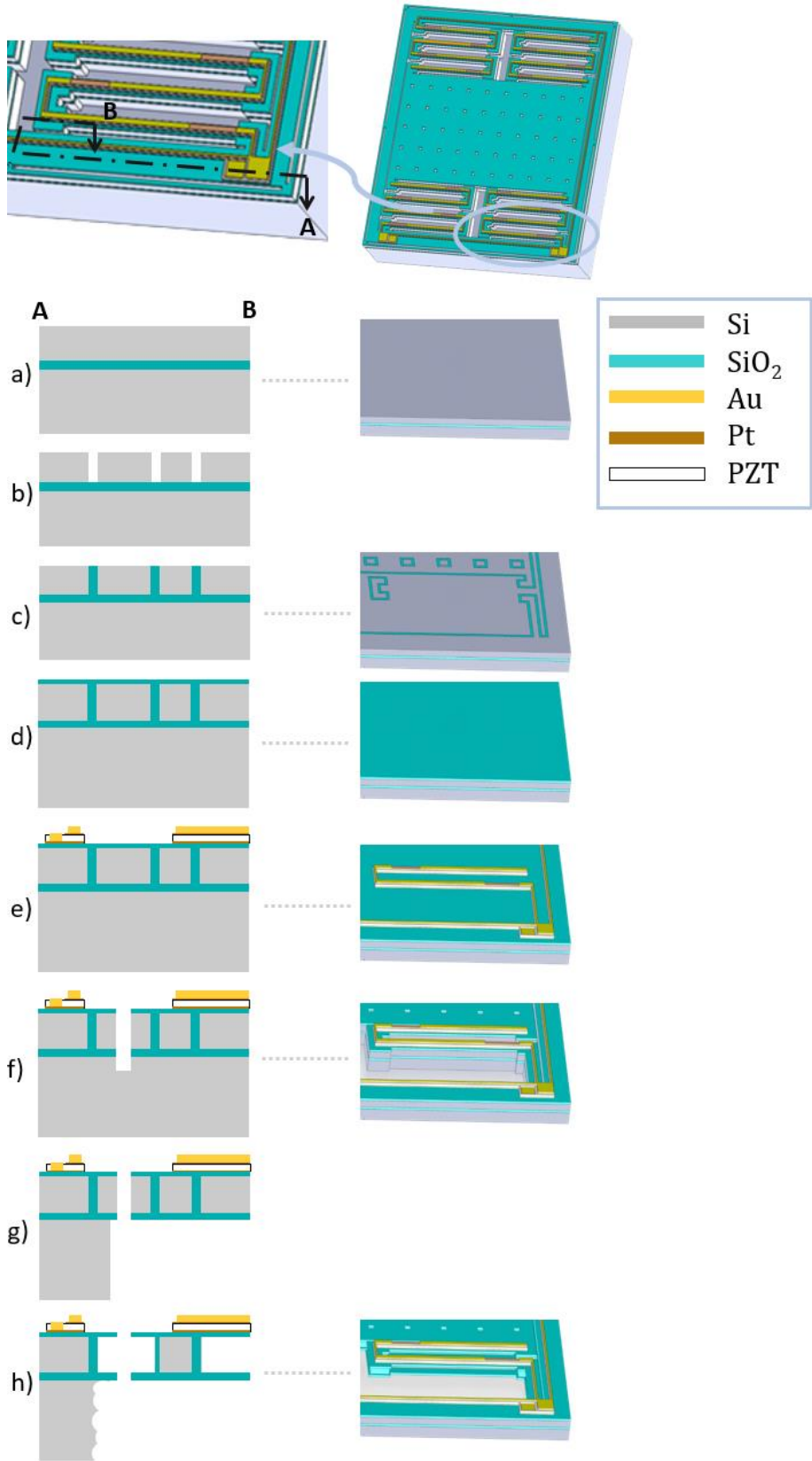


Figure 2.11. Fabrication process

2. 4. Performance Characterization

Based on the folded-leg design introduced in the previous section, two types of thin-film PZT scanners were fabricated. One type has all driving pads connected together so that only out-of-plane actuation can be generated, referred to as non-differential. The other type has with separate driving pads so that additional tilting modes can be achieved, referred to as a differential actuator. For both types of scanner, static and transient vertical motion were experimentally characterized, and static tilting motions (rotation about x- and y-axes) were also tested for the differential actuator. The testing results were used to develop an analytical model to capture fabrication uncertainty.

2. 4. 1. Characterization of Non-Differential-Drive Scanners

Non-differential actuators were tested for displacement in the vertical direction, with possible out of plane rotation about x- and y-axes. After poling the thin-film PZT at 15 V for 15 minutes and then stepping back to 0 V in 3 V increments, the static displacements of the four corners and the center of the stage were measured from 0 V to 15 V and back in 3V increments as shown in Figure 2.12. Measurements were taken using an Olympus LEXT OLS4000 3D Laser Measuring Microscope. Sample microscope images of the scanner at 0V and 15V are shown in Figure 2.13. The non-zero displacements at 0 V are due to the deflection of the stage and the beams of the legs from residual stress of the thin-film stacks. As presented in the figure, the micro-stage of the prototype scanner has shown as much as 430 μm of out-of-plane displacement at 15 V with two legs having more than 500 μm in a footprint less than 5 mm in diameter. This is very close to the performance needed for in vivo medical imaging for cancer diagnosis.

The transient response of the actuator was also obtained (Figure 2.15) by applying a pulse wave with a frequency of 4 Hz, pulse duration of 0.1 second, amplitude of 5V, and offset voltage of 2.5V. As expected using Bernoulli beam theory, the natural frequency of the scanner was found to be about 200 Hz. Compared to the approximated static displacement (z_D : $\sim 80 \mu\text{m}$) at 5 V (Figure 2.12), the steady state displacement of dynamic testing ($\sim 30 \mu\text{m}$) is noticeably smaller.

This is believed to be the case because the thin-film PZT was not poled before performing the transient test and a time varying input voltage was applied.

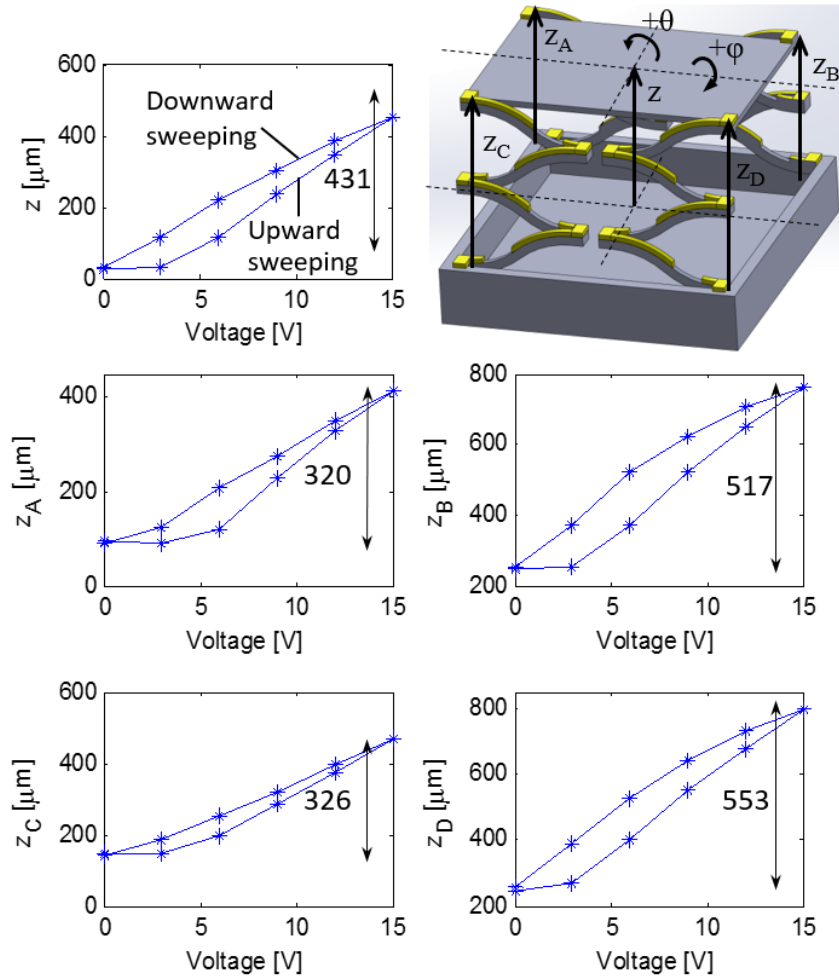


Figure 2.12. Experimental static displacements of the stage

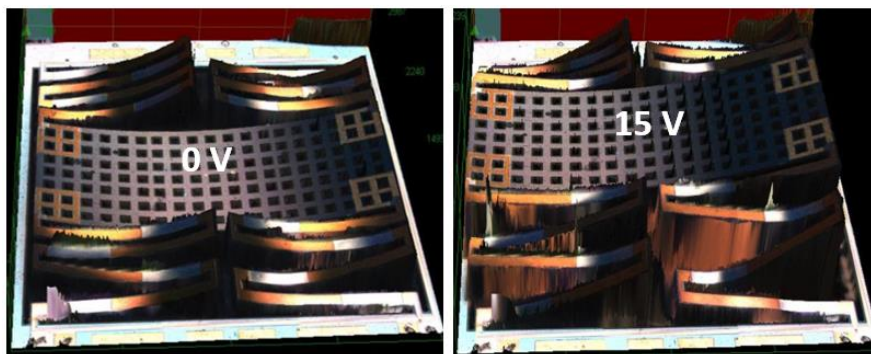


Figure 2.13. Microscope images of prototype scanners showing vertical motion

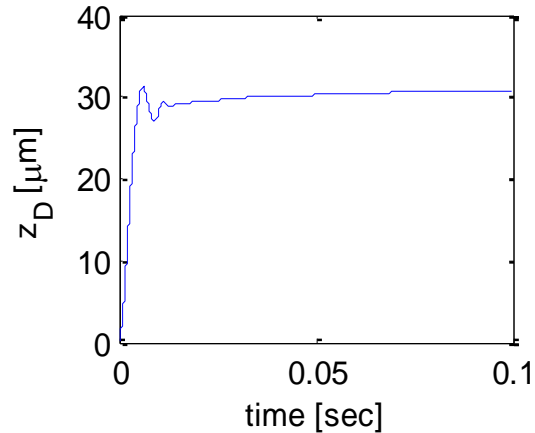


Figure 2.14. Transient response to a 5V impulse wave

2. 4. 2. Characterization of Differential-Drive Scanners

Prototype actuators with separate pads for each leg were also tested at different DC voltage levels, and their static and dynamic motion in response to various step voltage inputs was recorded. Applying step voltages from 14V to 2V in 3V-decrement and then from 2V to 14V in 3V-increment, the transient response of the center and four corners of the stage was measured. Before taking each measurement, a step input was applied about five times to allow the piezoelectric behavior of the PZT film to reach its steady state. This step was taken instead of a sustained poling process after observing the breakdown of PZT in other samples at the 15-20 V range. A Tenma's DC Power supply (72-6905) was used to supply step voltages, and a Keyence displacement sensor (LK-G32) to measure the displacement (Figure 2.15). A sampling cycle of 20 μsec and a built-in moving average filter were used to capture the transient motion of the stage, and they sufficed to measure the dynamics of the tilted stage. Although the peak time and damping ratio determined from the measurements are slower and higher, respectively, than the actual dynamics due to the implemented filter, it does not affect the measurements of the periods or the steady-state values, and the timing error due to averaging can be calculated. Different combinations of two legs were actuated at the same time to produce motion in each direction, as explained earlier.

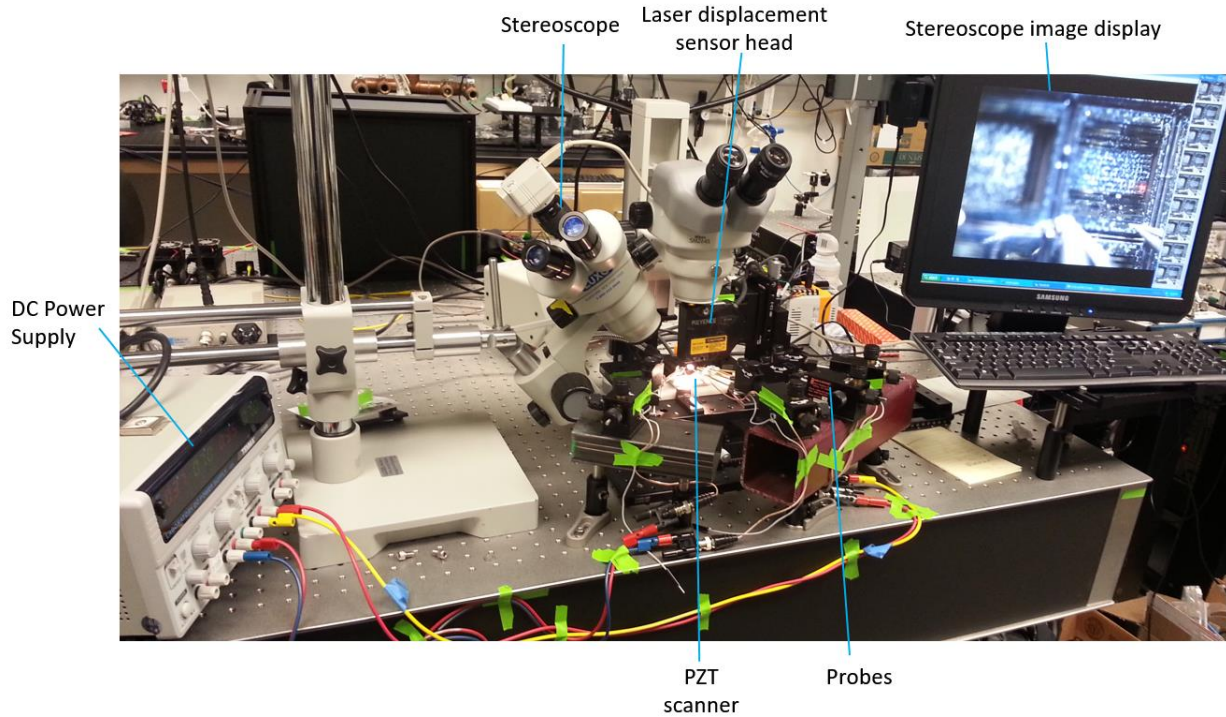


Figure 2.15. DC Testing setup for characterizing differential-drive scanners

Table 2.2. Static displacement of the stage

Actuation mode	Actuated legs	Displacement at 14V
translation in Z	A & D	$177.1 \pm 4.9 \mu\text{m}$
rotation about X (θ)	B & D	$6.4 \pm 0.3 \text{ deg}$
rotation about Y (ϕ)	A & B	$2.9 \pm 0.4 \text{ deg}$

Table 2.2 reports the maximum static displacement of one prototype actuator in each actuation mode at 14V, where static displacement was taken from the measurements of the transient response after it reached its steady state. It is noticed that angular displacement in the ϕ direction is smaller than in the θ direction, even though the opposite trend can be expected when the length of the stage is longer than the width if each leg only actuates its associated corner of the stage and provide the same actuation as other legs. However, it was observed that when legs A and B are actuated they also lift up the corners associated with legs C and D. Other sample

actuators with the same design have shown more than ± 10 degrees of tilt in the θ and ϕ directions at 15~20 V.

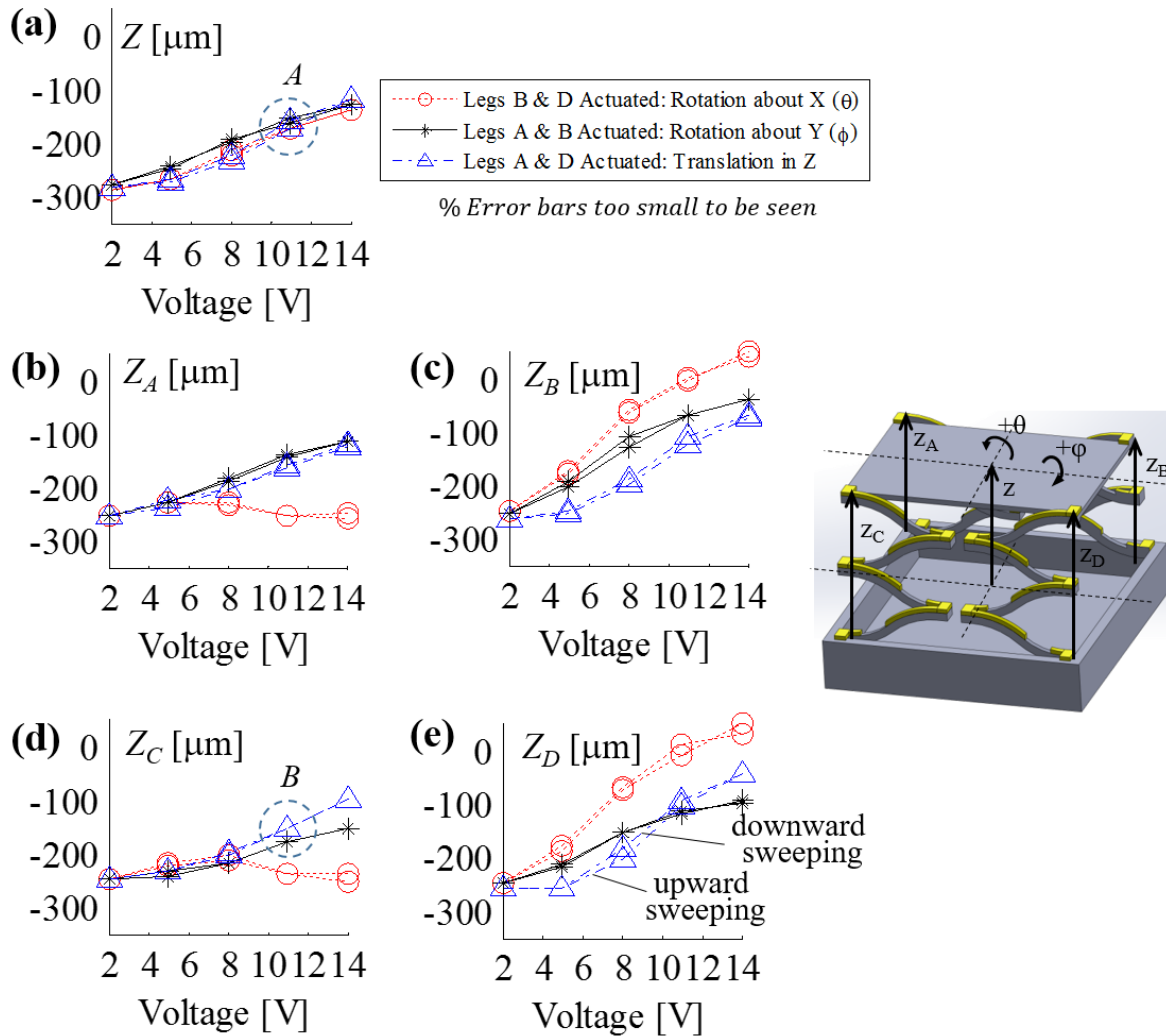


Figure 2.16. Static displacements of the stage when different combinations of legs are actuated

Experimental static displacements of a prototype differential-drive scanner are plotted in Figure 2.16 with deviation over typical 5 repeated tests. Although all the legs are designed to be symmetric and therefore to produce same displacements, they all show different displacements at each voltage. This is caused by non-identical initial deflections of the four legs at 0V due to non-uniform residual stress across the actuator and by different stroke lengths produced among the four legs. Residual stress can change due to environmental factors such as temperature or

humidity, affecting the repeatability of the actuator performance. Chapter 4 will examine modeling of motion accounting for residual stress; to improve the robustness of the actuator against environmental uncertainties, future work need to include developing a closed-loop control strategy.

Table 2.3. Transient response of stage when Legs A & D are actuated

In figure 3.4	Avg period	Peak time	Overshoot	Settling Time (5%)
Point A	12.0 ms	10.2 ms	16.4 %	23.44 ms
Point B	11.2 ms	13.0 ms	12.8 %	43.1 ms

Table 2.3 presents the characteristics of the transient response of the stage when it is actuated in the out-of-plane mode at 11V. The natural frequency in the Z direction was found to be about 84 Hz, lower than that of the scanner in the previous section due to the heavier mass of the stage (thicker device Si layer) but high enough to achieve the minimum required bandwidth of 10 Hz.

Device yield was primarily limited by poor adhesion of the gold layer to the piezoelectric legs and/or bond pads in spite of the use of an adhesion layer. In many cases, delamination of the gold layers of the electrode pads was observed during wire bonding.

2. 5. Imaging Using Low Frequency Actuation

Micro-scanners based on thin-film PZT for vertical cross-sectioning in endomicroscopy for early diagnosis of mucosal diseases have been fabricated and characterized. Although prototype devices show non-ideal vertical motion, one device was integrated to imaging setup built by Xiyu Duan, a collaborator in Biomedical Engineering at the University of Michigan, for initial imaging test.

2. 5. 1. Reflectance Mode Remote Scan

A sample actuator mounted on a dual in-line package (DIP) was used in a tabletop reflectance mode remote scan setup. When an imaging system is developed, a tabletop version is usually first built as a proof of concept. Developed by Botcherby *et al.*, a remote focus method, shown in Figure 2.17, is a novel imaging technique that allows fast out-of-plane refocusing for vertical sectioning or 3D imaging without moving the sample to be imaged or objective lens [2.7]. In remote scan, two microscope configurations, one with objective lens L_1 and another with L_2 , are combined back to back to achieve zero spherical aberration refocusing without moving the specimen. To avoid refocusing by moving a cumbersome objective lens L_2 , a small and light mirror is used for axial refocusing. The axial scanning speed is then dependent on the speed of the mirror.

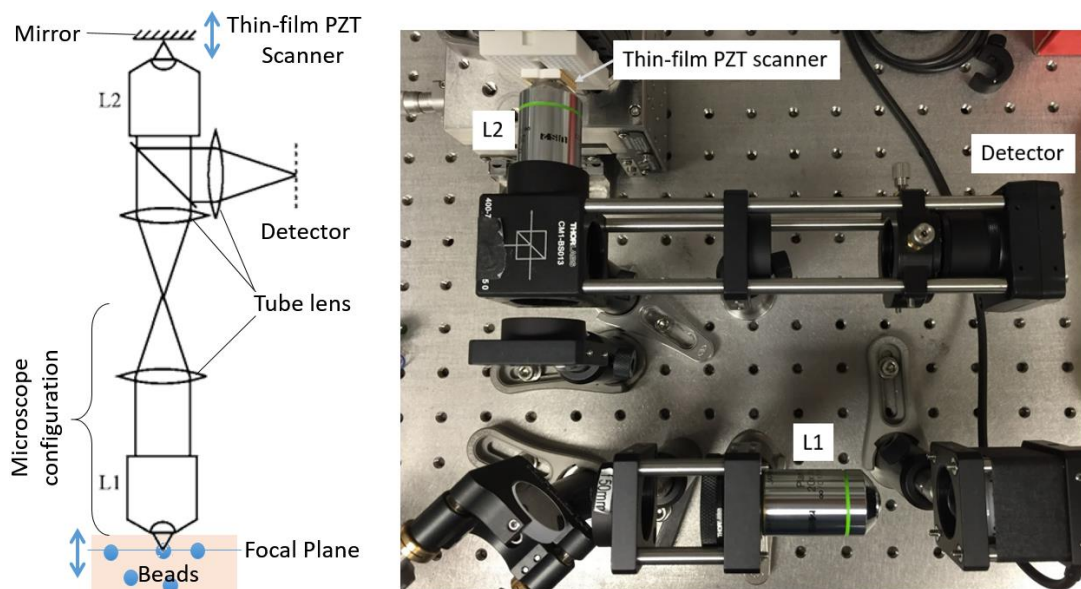


Figure 2.17. Reflectance mode remote scan setup (left: schematic from [2.7], right: tabletop setup made by collaborator Xiyu Duan, UM)

The sample thin-film PZT actuator shown in Figure 2.18 is used as an axial scanning mirror in the setup. The motion of the actuator when driven with a 5Hz 12V_{pp} 8V_{off} triangular wave is plotted in Figure 2.19, and as other tested devices it shows tilting motion as it travels vertically. Despite the low reflectivity of the stage due to the absence of a mirror or lens on it, reasonable quality images of 15 μ m diameter beads were obtained. As the scanner moves vertically, it changes the focal plane. Figure 2.20 presents shows the images obtained at different focal plane. This imaging

test has demonstrated that the scanner can effectively move the focal plane for vertical cross-sectional imaging, but also showed a need for mirror surface. As mentioned in Chapter 2, the actuators were designed with an intention to mount a mirror chip or lens on top of the stage, but it turned out that is not an easy task without proper equipment. It was decided to remove the holes in the stage and coat it with gold for a reflective surface for the next generation of devices.

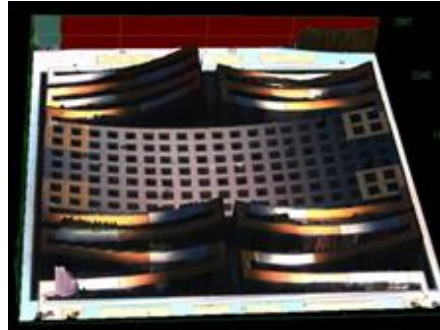


Figure 2.18. Sample scanner integrated into the imaging system in Figure 2.17

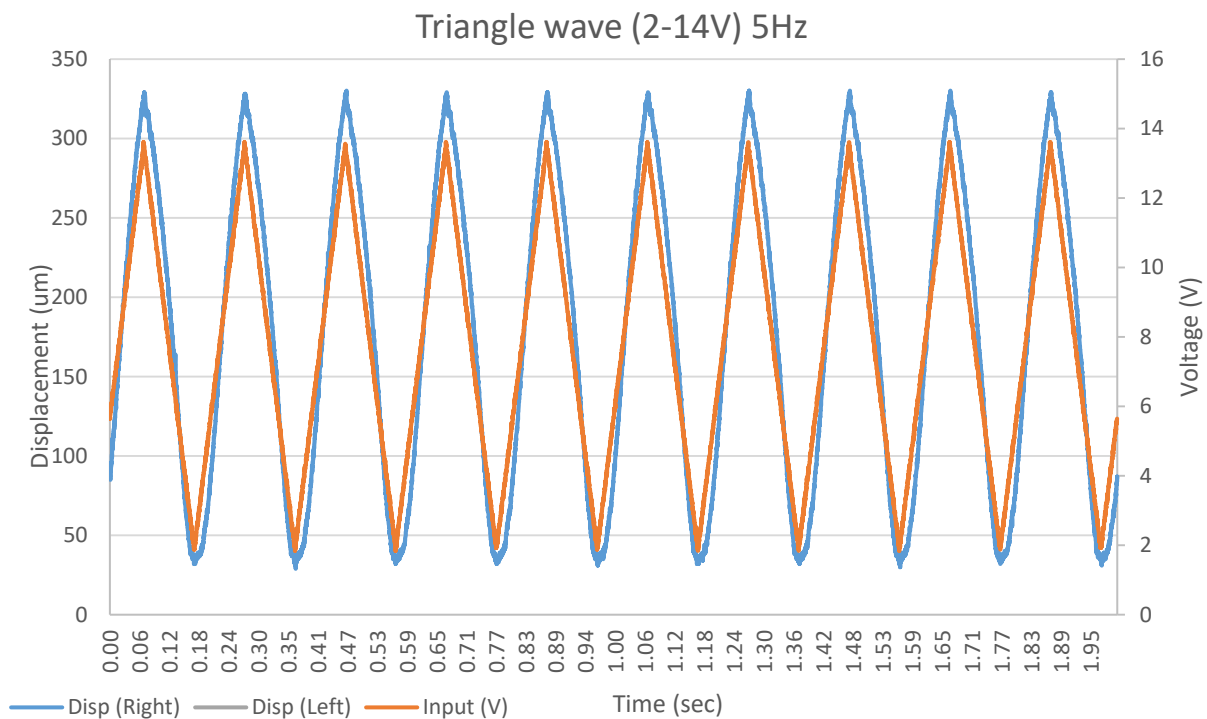


Figure 2.19. Actuator behavior with 5Hz triangular wave (12V_{pp} 8V_{off})

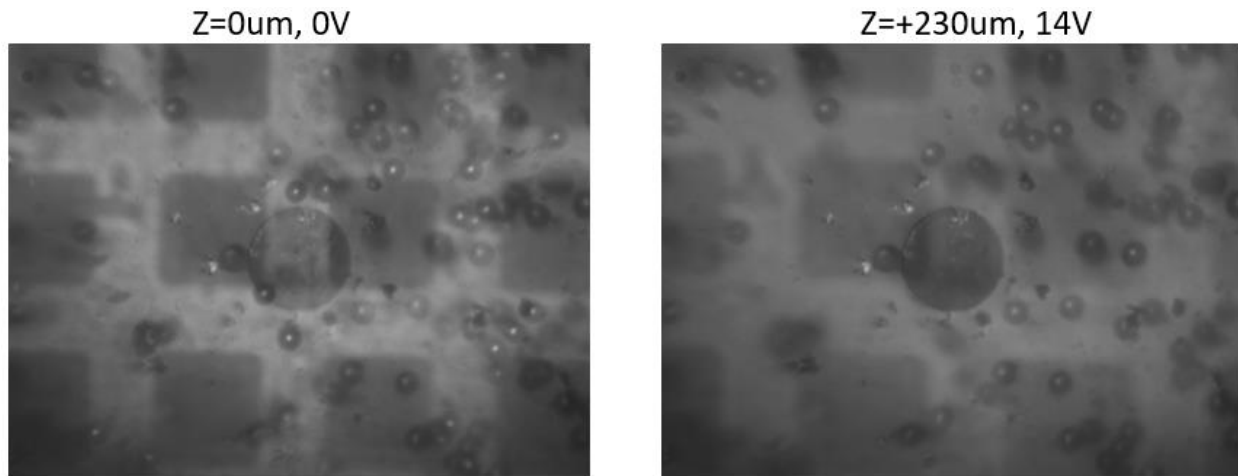


Figure 2.20. Images of beads taken at different focal plane (Photo credit: Xiyu Duan, Biomedical Engineering, UM)

2. 5. 2. Two Photon Imaging

As explained in Chapter 1, multi-photon microscopy offers both high resolution and significant imaging depth using intense ultrafast pulses of long wavelength light to excite shorter wavelength photons via nonlinear effects. Relative to other optical imaging modalities, multi-photon microscopy has benefits of reduced photobleaching and capacity to excite endogenous fluorescence, in addition to its compatibility with a variety of targeted fluorescent biomarkers, making it a good technique for vertical sectioning.

The remote scan setup described in the previous section was reconfigured for 3D multiphoton microscopy. A Ti-Sapphire laser was used to provide ultra-short (wavelength: 750nm), high peak-intensity pulses of light, which is linearly polarized and then reflected off from the a 2D electrostatic MEMS mirror. Lenses L_1 and L_2 expand the beam for the size of the back aperture of lens L_3 . After going through the beam splitter and the quarter wave plate, the beam reflects off from the stage of the PZT scanner. After double-passing the quarter wave plate, the beam has changed its polarization state and is directed toward L_4 via the beam splitter. Passing through telescope lenses L_4 and L_5 , the beam is reflected by the dichroic mirror and focused on the sample by objective lens L_6 . Fluorescence generated from the specimen goes through the dichroic mirror and is focused by L_7 before collected by a photomultiplier tube (PMT) detector. Scanning in the

x-y plane is achieved by the 2D electrostatic mirror, and as the PZT scanner moves vertically, it performs a “remote” (distant from the distal optics) z-axis scanning.

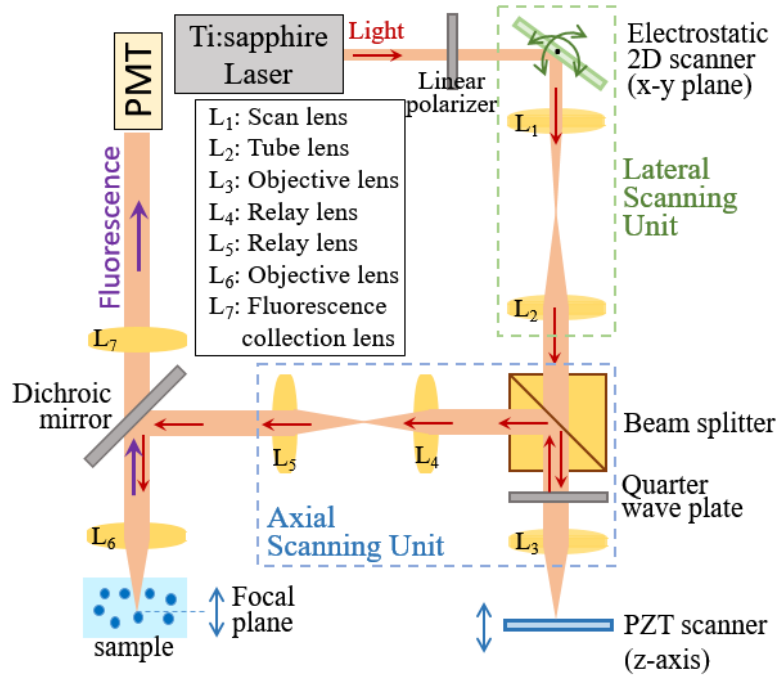


Figure 2.21. Schematic of 3D multiphoton imaging system

The electrostatic mirror produced more than 5.5° of mechanical scanning angle in both X and Y axes with 60Vpp sine wave at 8210 Hz and 1960 Hz for the X and Y axes, respectively. More details of the electrostatic scanner are reported in [2.8]. The PZT scanner was actuated with the same input as the reflectance mode with a 5Hz 12V_{pp} 8V_{off} triangular wave shown in Figure 2.19 to image with a frame rate of 1 Hz 15 μ m diameter florescent beads in a polydimethylsiloxane polymer matrix, used as a simple tissue phantom for basic imaging system evaluation. Figure 2.23 shows x-y plane image at two different depths. Because of the holes in the stage (Figure 2.18), the full shape of many beads was not collected. Also, because of the non-ideal off-axis rotation generated during the vertical motion, only one bead showed a strong signal. For better imaging results, a reflective surface in thicker silicon stage was decided to be integrated for a better mirror, and a model to be developed to compensate for the off-axis rotational motion.

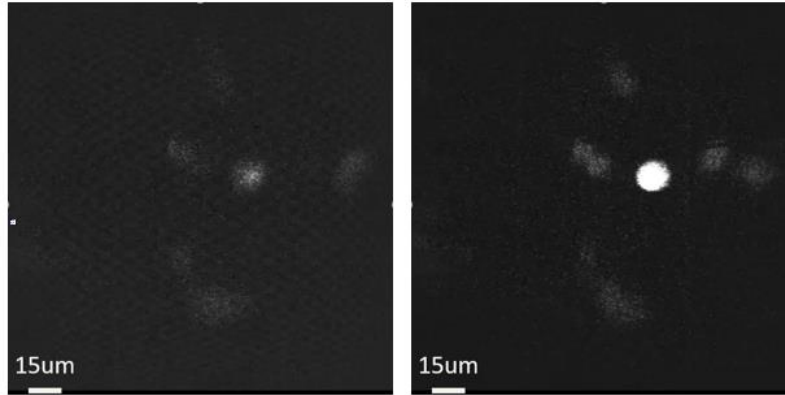


Figure 2.22. Fluorescent bead imaging with remote axial scanning in multiphoton microscopy

2. 6. Summary

For accurate early cancer detection in the digestive tract in optical endomicroscopy, a miniature scanning mechanism to move the focal point of the light over a large range at a fast speed. While the actuators based on conventional technology such as DC motors are too large for medical endoscopes, MEMS technology can provide the required performance in an endoscope-compatible form factor (footprint <5mm in diameter).

There has previously been developed various vertical translational MEMS scanners with different actuation schemes, but they either do not have the required performance (*i.e.* too slow and/or not enough displacement) or have some limitations to be used in an endoscopic system. Here multi-axis micro-scanners based on thin-film PZT for deep vertical optical sectioning in endomicroscopy are introduced. They have a central mirror platform that is actuated by four symmetric PZT bending legs. The prototype scanners are fabricated from silicon-on-insulator wafers with both front- and backside- patterning following the deposition and patterning of the PZT layer.

Prototype piezoelectric micro-scanners that had been designed to produce large displacements in three axes (translation in z axis, rotation about x and y axes) and a relative high bandwidth in z-axis direction were tested. They closely meet the performance requirement for real-time early cancer detection in endomicroscopy. They have shown more than 430 μm of vertical displacement at 15 V with a natural frequency of about 200 Hz, and approximately 6.4° and 2.9° of stage tilting about the x-axis and y-axis, respectively, at 14V in a footprint of 3.2×3.2 mm.

Using these working prototypes, initial imaging tests were performed where a remote z-axis scan was realized for vertical sectioning in reflectance and multiphoton microscopy. Obtained images of simple tissue phantoms showed effective change of the focal plane by the vertical motion of the PZT scanner, but it was recognized that a better method to integrate a mirror to the stage and to produce pure vertical motion is needed for improved image results.

2. 7. References

- [2.1] Qiu, Z., Pulskamp, J. S., Lin, X., Rhee, C.-H., Wang, T., Polcawich, R. G., and Oldham, K., 2010, Large displacement vertical translational actuator based on piezoelectric thin films, *Journal of Micromechanics and Microengineering*, 20.
- [2.2] Trolrier-McKinstry S, Muralt P. Thin film piezoelectrics for MEMS. *Journal of Electroceramics*. 2004 Jan 1;12(1-2):7-17.
- [2.3] Hopcroft M A, Nix W D and Kenny T W 2010 What is the Young's Modulus of Silicon? *Microelectromechanical Systems, Journal of* 19 229-38
- [2.4] Sharpe W N, Pulskamp J, Gianola D S, Eberl C, Polcawich R G and Thompson R J 2007 Strain Measurements of Silicon Dioxide Microspecimens by Digital Imaging Processing *Experimental Mechanics* 47 649-58

- [2.5] Hemker K J and Sharpe W N 2007 Microscale Characterization of Mechanical Properties Annual Review of Materials Research 37 93-126
- [2.6] Rhee C-H, Pulskamp J S, Polcawich R G and Oldham K R 2012 Multi-Degree-of-Freedom Thin-Film PZT-Actuated Microrobotic Leg Journal of Microelectromechanical Systems 21 1492-503
- [2.7] Botcherby, E.J., Juskaitis, R., Booth, M.J. and Wilson, T., 2007. Aberration-free optical refocusing in high numerical aperture microscopy. Optics letters, 32(14).
- [2.8] Duan, X., Li, H., Oldham, K., Wang, T., 2016, MEMS-based multiphoton microscopy with remote axial scanning, Biomed. Opt. Express, 2016, Submitted

CHAPTER 3: SECOND GENERATION PIEZOELECTRIC ACTUATOR

3. 1. Problems with 1st Generation Devices

Although some devices from the 1st generation demonstrated high performance needed for real-time *in vivo* vertical cross sectioning in endomicroscopy, the device yield was low due to some problems observed at different fabrication steps. This chapter presents different causes of device failure and discusses possible solutions that was implemented.

3. 1. 1. Delamination of Gold Layer

As mentioned in the previous chapter, delamination of the gold bonding pads on top of the PZT stack was one of the main sources of device failure even with the use of a Cr or Ti adhesion layer (Figure 3.1). In some devices, the gold layer on the piezoelectric unimorphs was observed to be delaminated as shown in Figure 3.2 after a certain period of operation. To remedy this problem, aluminum, instead of gold, was selected to be used for the next generation of the devices as it generally has better adhesion. Furthermore, aluminum jumpers were included above a parylene insulation layer as illustrated in Figure 3.3 because a metal layer deposited directly on the silicon layer usually does not have the delamination problem.

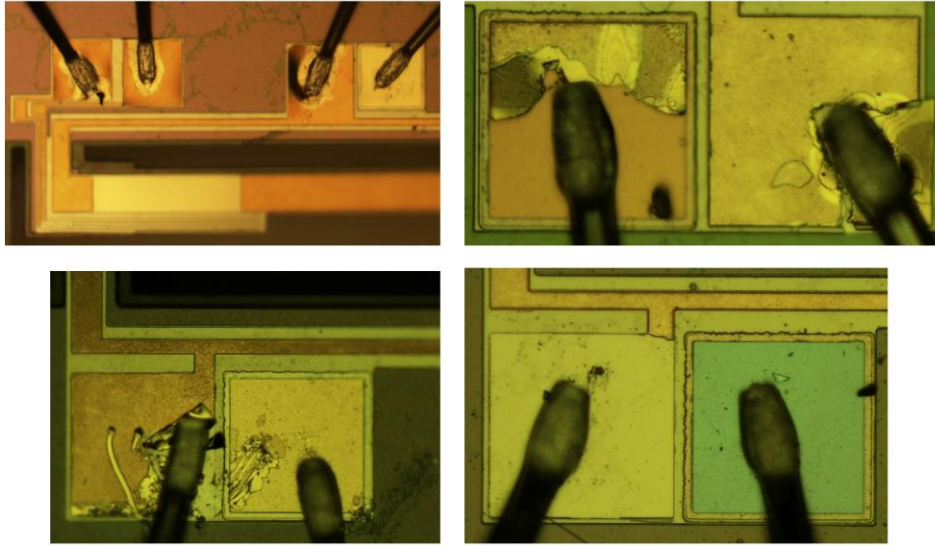


Figure 3.1. Delamination of gold bonding pads

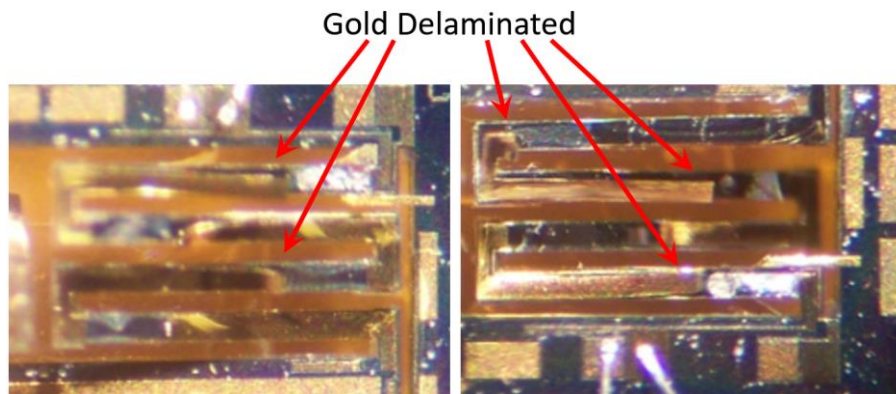


Figure 3.2. Delamination of gold layer on Legs

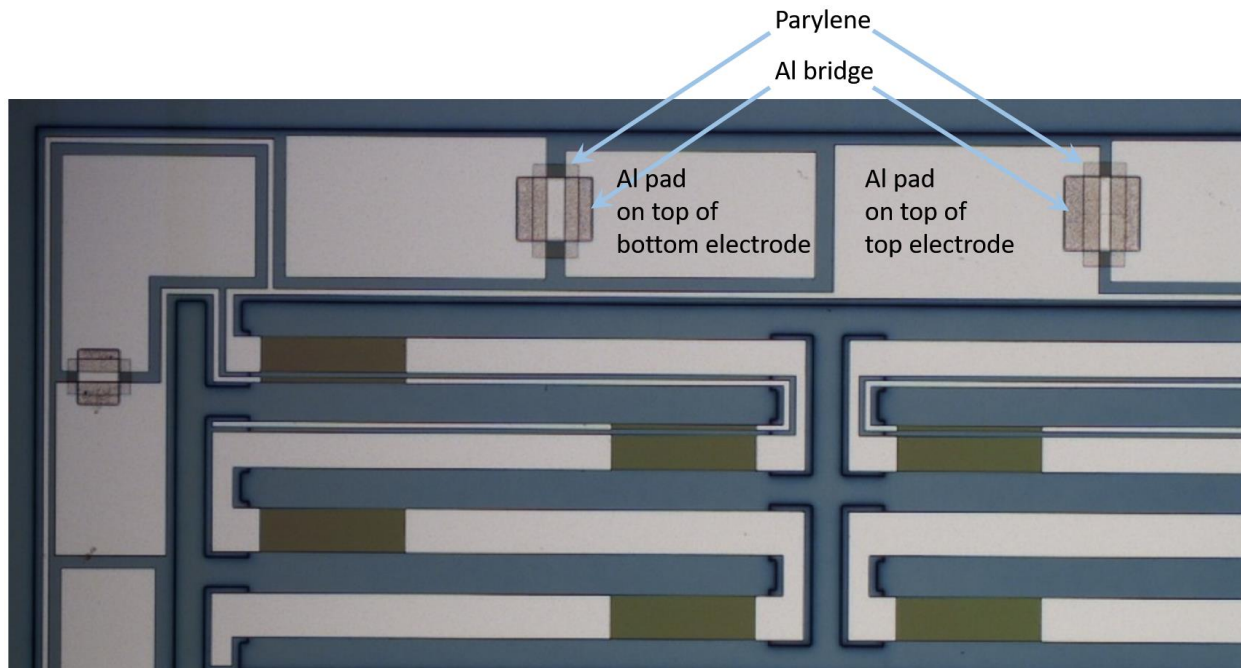


Figure 3.3. Concept aluminum jumper on a patch of parylene

3. 1. 2. Over-etching of Frame

The other main source of device failure was over-etching of the silicon handle layer during the final release step where silicon underneath PZT unimorphs are etched by the XeF_2 gas, described in Figure 2.11 (h). Since light is reflected from the central mirror surface of the scanner, the flatness of the central stage is important. It was observed that a 10- μm -thick stage was noticeably curved due to residual stress (Figure 3.4). However, when a 30- μm -thick silicon device layer was used for a flatter mirror surface, the time to etch the 30- μm -thick silicon underneath the PZT bending beams was long enough to substantially over-etch the silicon handle layer, which was designed to be used for mechanical support frame. As shown below in Figures 3.5 and 3.6, the remaining silicon in the handle layer is much less after final release for the devices with the 30 μm thick device layer. It is very hard to handle these over-etched scanners shown in Figure 3.6 as they are extremely fragile.

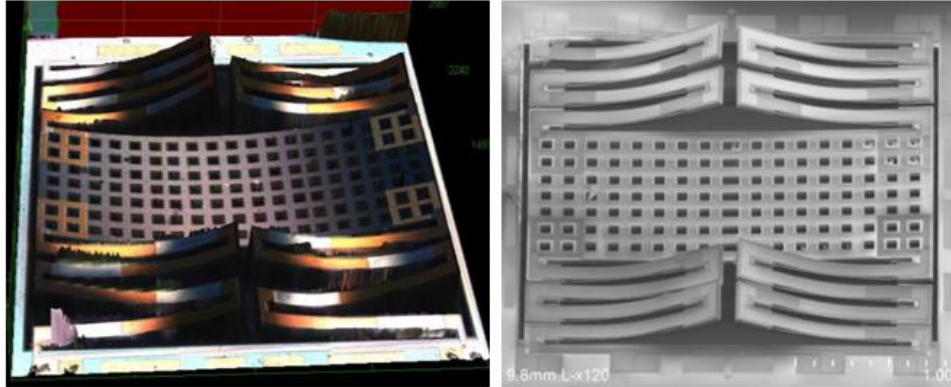


Figure 3.4. Bending of a 10µm-thick stage (left) is noticeably more than that of a 30µm-thick stage (right)

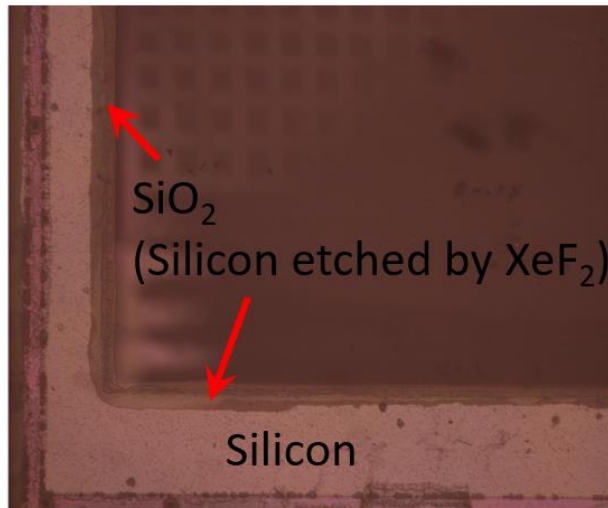


Figure 3.5. Microscope image of the backside of a sample scanner with 10 µm device layer after final release, focused on the handle layer of SOI

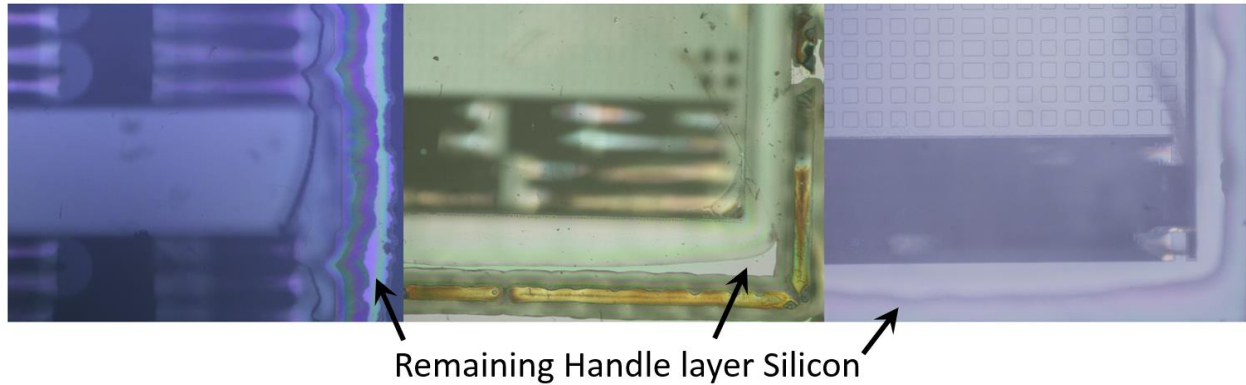


Figure 3.6. Microscope image of the backside of a prototype scanner with 30 μm device layer after final release, focused on the handle layer of SOI

One way to avoid this problem is to minimize the XeF_2 etching time by partially or completely remove the silicon under the PZT stack as described in Figure 3.7. These new process steps can be used after finishing patterning the PZT stack, which corresponds to the step illustrated in Figure 2.11 (e). The shallow trenches on the top side are needed because if they were etched through the device layer the mounting material used to mount the wafer on a handle wafer during the backside etch could fill in the trench and could act as a mask and prevent proper etch of silicon under the PZT stack. Since the complete removal of the device layer silicon during backside etching makes the devices very fragile and increases the risk of damaging the devices when unmounting the wafer from the handle wafer, one can partially etch the silicon, and then the remaining silicon can be etched using XeF_2 .

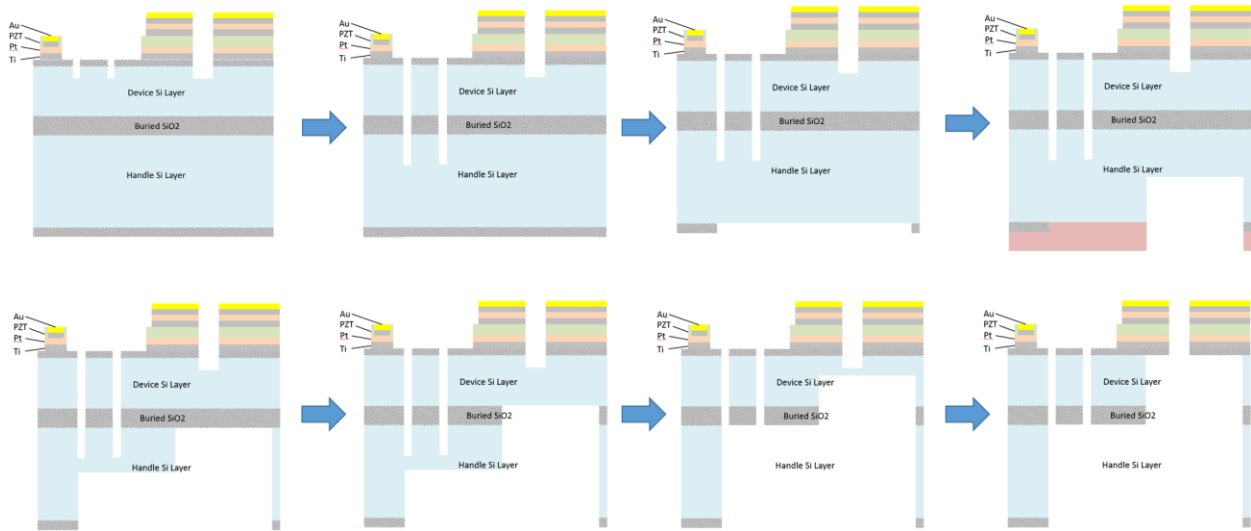


Figure 3.7. Release by DRIE

3. 1. 3. Failure of SiO₂ Encapsulation

Another device failure was related to the pinholes in the PECVD SiO₂ (Figure 3.8 (a)-(c)) deposited in step (d) in Figure 2.11 or the over-etched SiO₂ (Figure 3.8 (d)) during the PZT stack patterning performed in step (e) in Figure 2.11. Improperly filled trenches (performed in step (c) in Figure 2.11) that caused the etch of the structural silicon were also observed as shown in Figure 3.9. Thicker SiO₂ base layer beneath the PZT stack can minimize the pinhole and over-etching problem, but the thicker it is the stiffer the beams become, reducing their maximum displacements. This problem can also be avoided by reducing or removing XeF₂ etching. Thus, the DRIE release method (Figure 3.7) can remedy this problem as well. To simplify the repeated planarization and refilling steps to remove voids in the trenches to be refilled with SiO₂ and to perform a better refill, it was decided to use more conformal tetraethyl orthosilicate (TEOS) SiO₂, instead of LPCVD SiO₂ used in the 1st generation devices. Also, it was determined to use an LPCVD SiO₂ layer instead of PECVD SiO₂ as a base SiO₂ layer beneath the PZT stack after finishing polishing the TEOS SiO₂ layer to avoid producing pinholes.

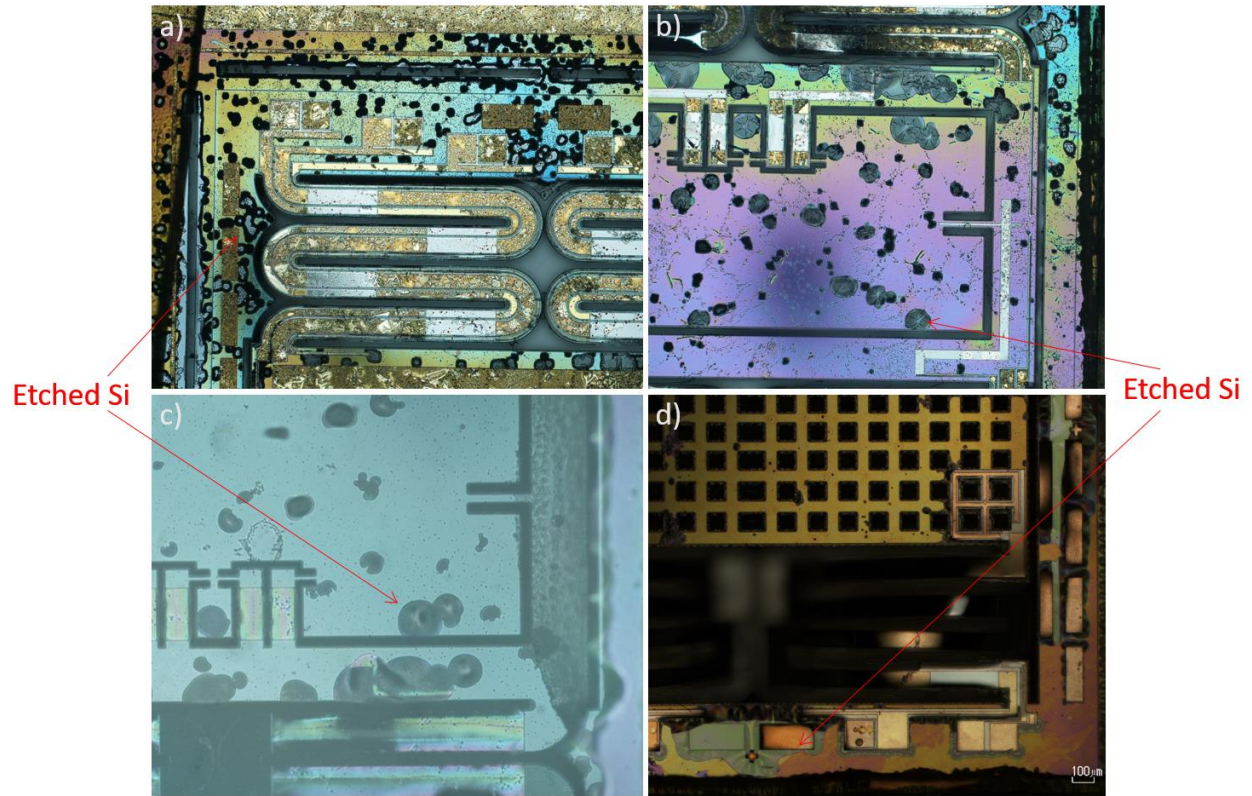


Figure 3.8. Microscope images of sample actuators that show etched device Si layer through the pinholes or over-etched areas in top SiO₂ layer



Figure 3.9. Etched silicon structure during XeF₂ etching due to voids in the SiO₂-filled trenches

3. 1. 4. Non-uniform XeF₂ Etching Due to Teflon

Release trenches are made using DRIE, where a Teflon-like fluorocarbon layer is deposited to protect the sidewall and inhibit lateral etching so that high aspect ratio trenches can be produced. However, this polymer film is usually not completely removed and sometimes affects later processes, such as a XeF₂ release step shown in Figure 3.10. The Fluorocarbon layer on the silicon sidewall (Figure 3.11) is preventing silicon to be etched by the XeF₂ gas, thus inhibiting a proper release. To remove this film, O₂ plasma can be used, but for the case of high aspect ratio trenches it is often very difficult to completely remove it because reactive species and ions can't easily reach the bottom side of deeper trenches. Releasing the actuators using DRIE can also allow to avoid this problem.

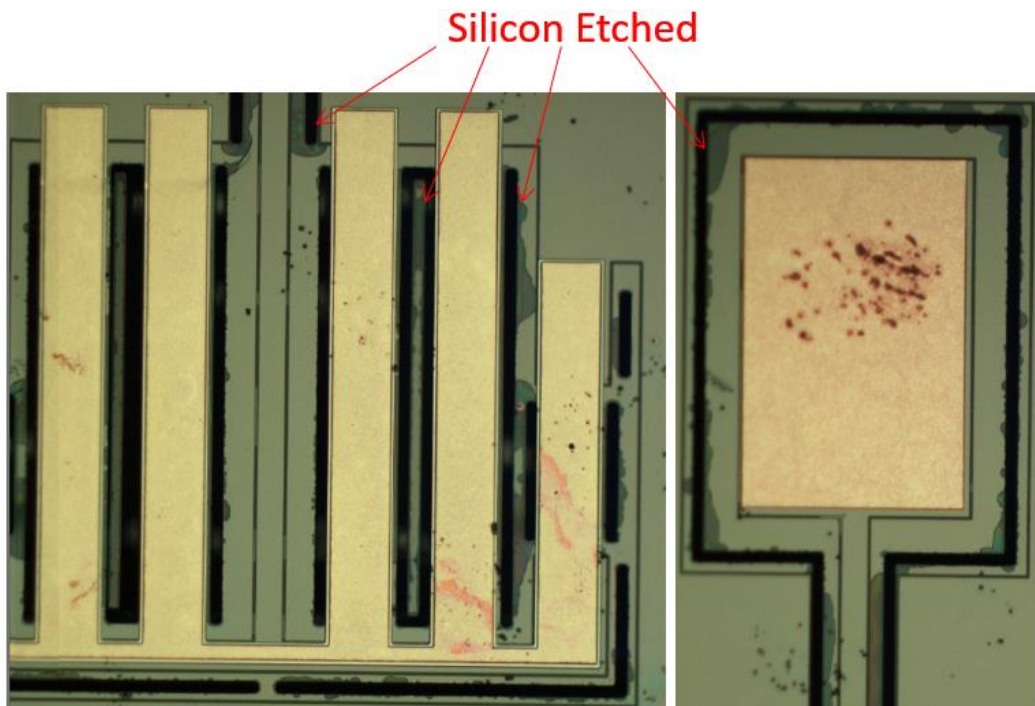


Figure 3.10. Microscope images showing non-uniform XeF₂ etching of silicon due to remaining fluorocarbon layer on the sidewalls from Bosch process

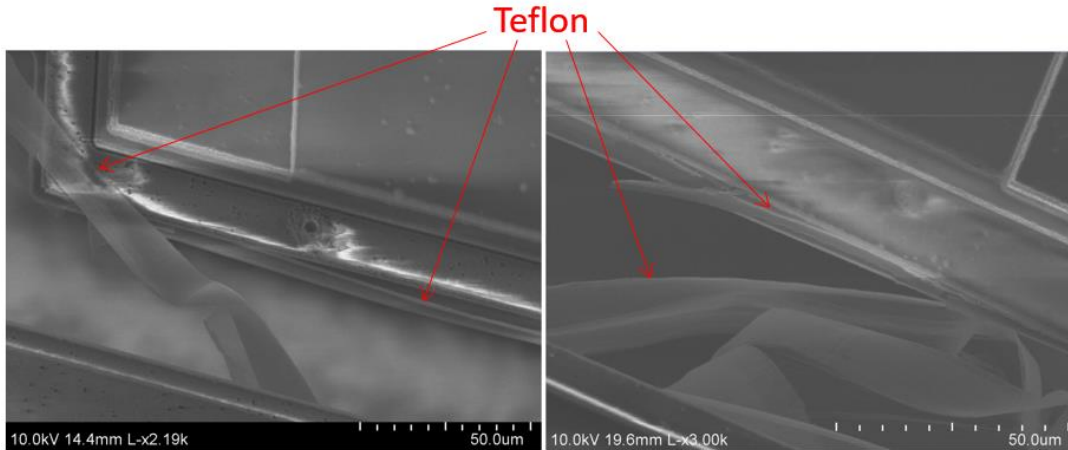


Figure 3.11. SEM images showing fluorocarbon layer on the sidewalls

3. 1. 5. Varying Outcome of Buried SiO₂ Layer

Although it does not directly affect the device yield, the behavior of the buried SiO₂ layer can largely contribute to varying performance of bending legs even within single devices. As shown in Figure 3.12, sometimes the buried SiO₂ layer sticks to the PZT stack, sometimes it remains in parallel with the PZT stack, or sometimes it breaks. Even though its effect can be possibly compensated by differential actuation, having one less source of variation is beneficial. DRIE release is helpful in this case as well, as it removes the buried SiO₂ layer.

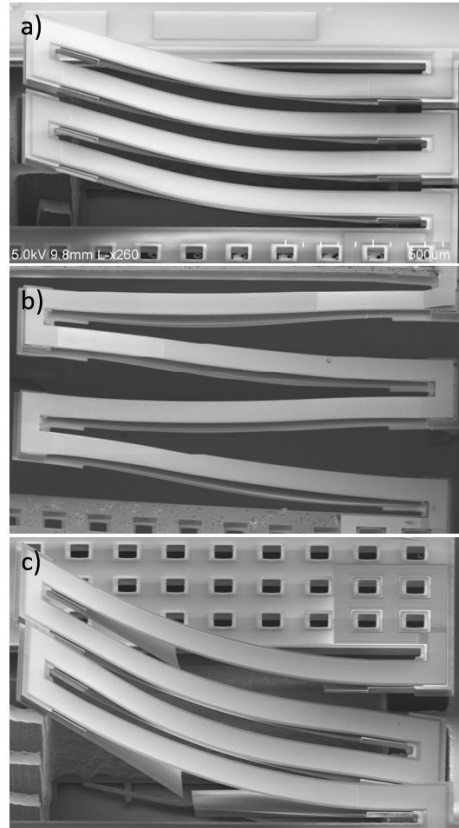


Figure 3.12. SEM images of different outcomes of buried SiO₂ layer

3. 2. New Fabrication Process

As previously mentioned, because of the difficulties associated with manually mounting a mirror or lens on top of the stage, it was determined to coat the stage surface with an aluminum or gold layer as shown in Figure 3.13. Since the actuators do not need to carry any payload with the embedded mirror surface, the gold coverage over the beams of 50% were also included for maximum placement based on the design optimization analysis presented in Figure 2.9. Table 3.1 summarizes the causes of device failure and possible solutions. Because of the issues affecting the XeF₂ release, 1st generation devices with 30μm thick device layer were processed die by die to increase yield.

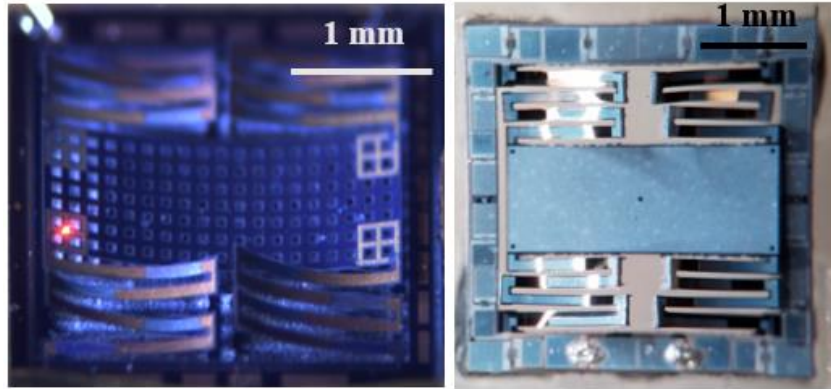


Figure 3.13. Microscope images of 1st generation device without embedded mirror surface (left) and 2nd generation device with embedded mirror surface (right)

Table 3.1. Issues with 1st generation devices and proposed solutions

Problems	Proposed Solution
Poor Gold adhesion	Use of aluminum & parylene Jumper Parylene Reinforcement
Over-etching of the handle layer silicon (frame)	
SiO ₂ Encapsulation Failure	Minimize XeF ₂ etching; DRIE release
Release problem due to teflon on the sidewall	
Varying outcome of buried SiO ₂ layer	
Difficult mirror or lens assembly	Integration of mirror surface
Long process time due to die-by-die processing	Module- or wafer-level processing

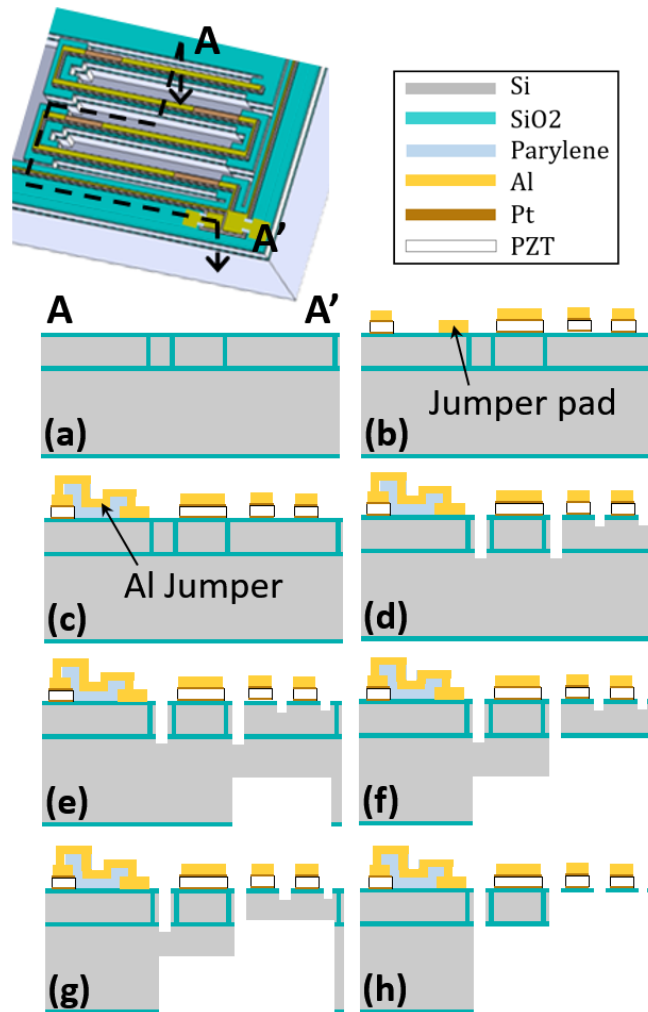


Figure 3.14. New fabrication process

Addressing the problems encountered in fabricating the 1st generation devices, a new fabrication process was defined as presented in Figure 3.14. First, narrow trenches are etched by deep reactive-ion etching (DRIE) to the buried oxide layer, and refilled by tetraethyl orthosilicate (TEOS) chemical vapor deposition (CVD) silicon dioxide (Figure. 3.14 (a)). The top surface of the wafer is chemically-mechanically polished and coated with an additional high temperature low pressure chemical vapor deposited (LPCVD) silicon dioxide that provides a uniform base layer for PZT deposition. The isolated structures in the device layer produced by this step become precisely defined rigid silicon elements of the completed platform, such as the frame and mirror platform.

Bottom electrode (Ti/Pt, 200 nm), piezoelectric (PNZT seed/chemical solution PZT, 1.2 μm) and top electrode (Pt, 120 nm) layers are next deposited on the prepared wafer (Radiant Technologies, Albuquerque, NM), and sequentially patterned by reactive-ion etching (RIE). A structural aluminum layer (1 μm) is then patterned by a lift-off process to the top surface of select regions of the electrodes, to improve bond-pad strength and adjust the neutral axis of bend-down portions of cantilever beams (Figure. 3.14 (b)). To further improve reliability of electrical interconnects, a parylene-C film (560 nm), silicon dioxide (230 nm) layer, and additional aluminum layer (1 μm) are deposited to create electrical jumpers from the top and bottom electrodes of the PZT film to bond pads patterned directly on the silicon dioxide wafer surface, which were found to have much better reliability for wire bonding necessary in the confined space of endomicroscopy instruments (Figure. 3.14 (c)). Microscope images of completed electrical jumpers are presented in Figure 3.16.

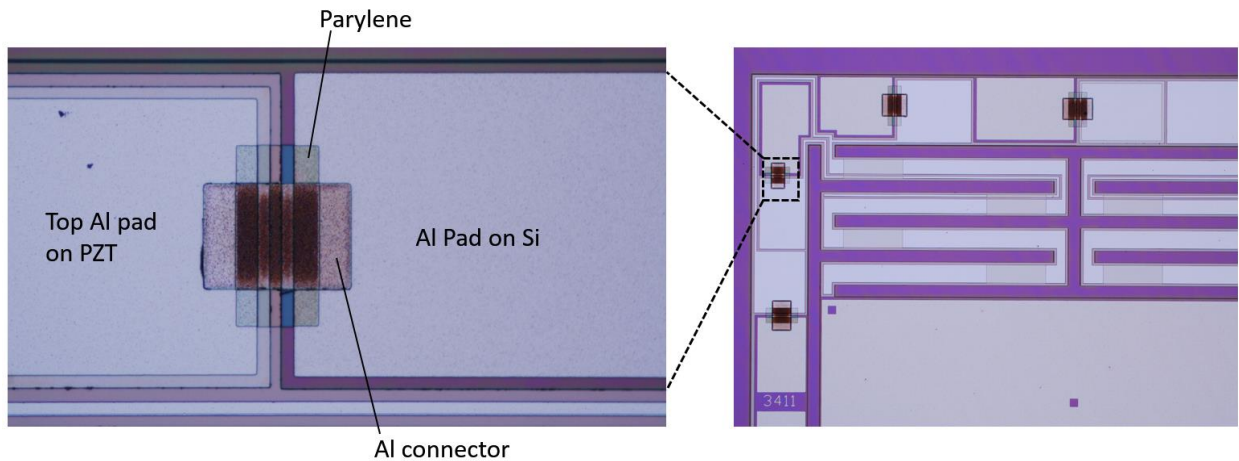


Figure 3.15. Electrical jumpers made from aluminum pads and parylene insulation layer

Release of actuators from the silicon wafer is performed using a series of deep trench etching steps. First, silicon DRIE and silicon dioxide RIE steps are performed to etch through the buried oxide between actuation legs (Figure. 3.14 (d)). Then, two-level backside DRIE is performed, with initial etching beneath the actuation legs (Figure. 3.14 (e)), then full backside area etching beneath all moving parts (Figure. 3.14 (f) and Figure 3.16).

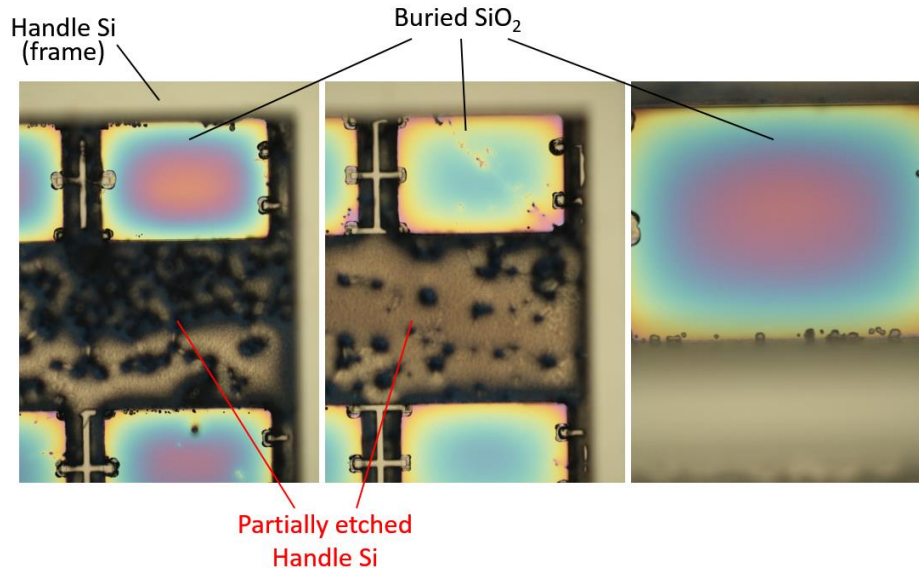


Figure 3.16. Microscope images of backside of sample devices after step (f) in Figure 3.15 completed

By etching the silicon dioxide layer exposed initially by the deeper portion of the backside etch (Figure. 3.14 (g) & Figure 3.17) before completing the backside DRIE process (Figure. 3.14 (h) & Figure 3.18), free-standing thin-film PZT beam elements could be released, while retaining a solid silicon platform as a mirror platform or as the mirror itself. Depending on the depth of the initial backside etching in step (e) in Figure 3.14, finished etching can have handle layer silicon on moving parts as shown in Figure 3.18 or not as in Figure 3.19. The devices such as shown in Figure 3.18 have more mass and thus lower natural frequency. If the remaining handle layer silicon is too thick, XeF₂ etching can be performed to etch some of the silicon.

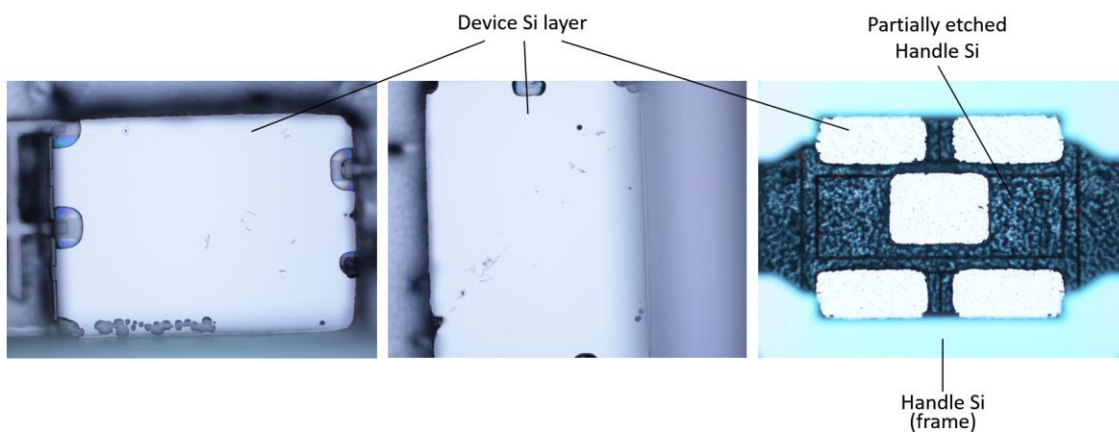


Figure 3.17. Microscope images of backside of sample devices after step (g) in Figure 3.15 completed

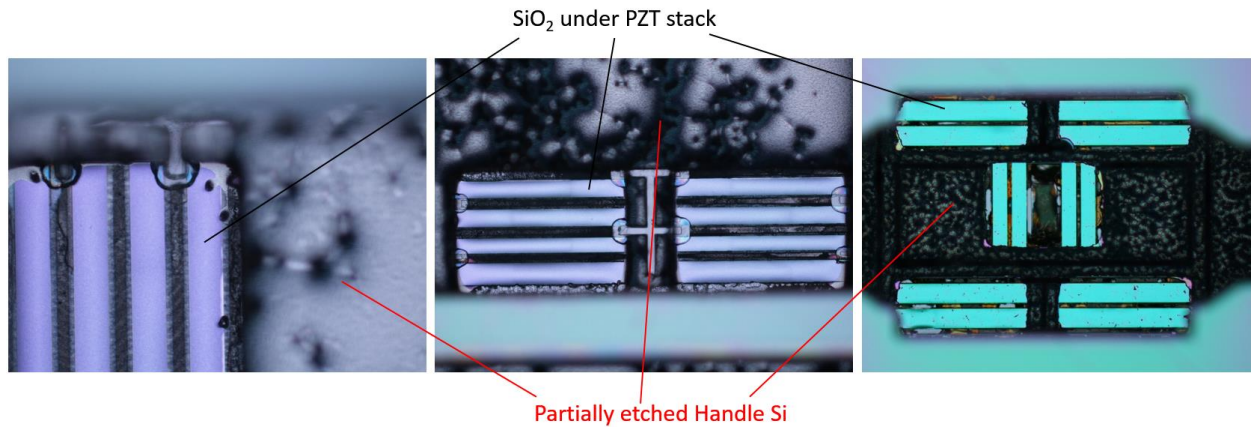


Figure 3.18. Microscope images of backside of sample devices that show moving parts still have silicon in the handle layer after step (h) in Figure 3.15 completed

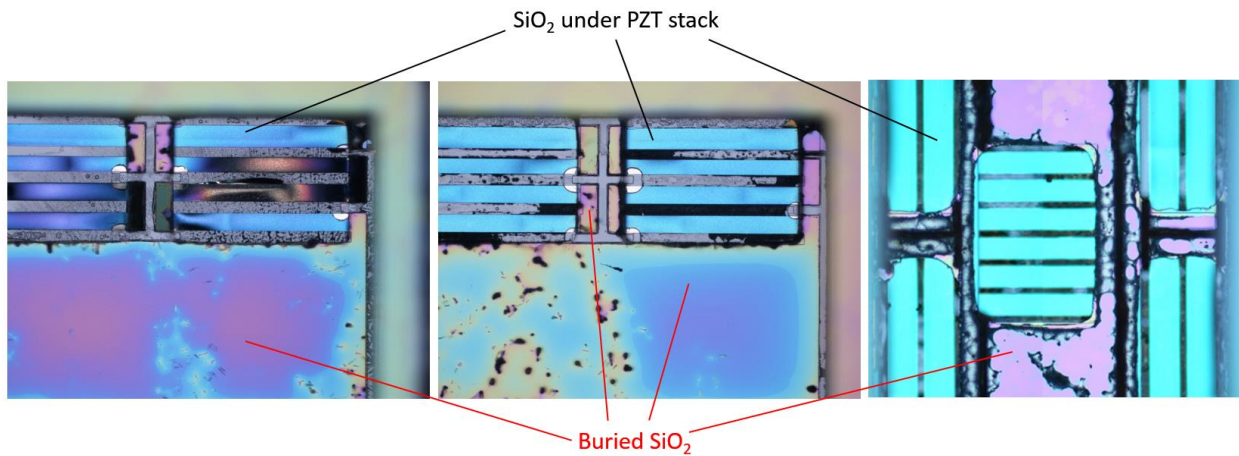


Figure 3.19. Microscope images of backside of sample devices that show all the silicon in the handle layer is etched after step (h) in Figure 3.15 completed

During this last release step, non-uniform etching of silicon or the formation of micro-columns or grass, such as shown in Figure 3.20 can be handled with SF_6 or XeF_2 etching thanks to the silicon-dioxide-filled trenches formed in the earlier step (Figure. 3.14 (a)). With optimized etching parameters and layer thicknesses, the formation of the protective silicon dioxide trenches in the device layer (Figure. 3.14 (a)) can be omitted.

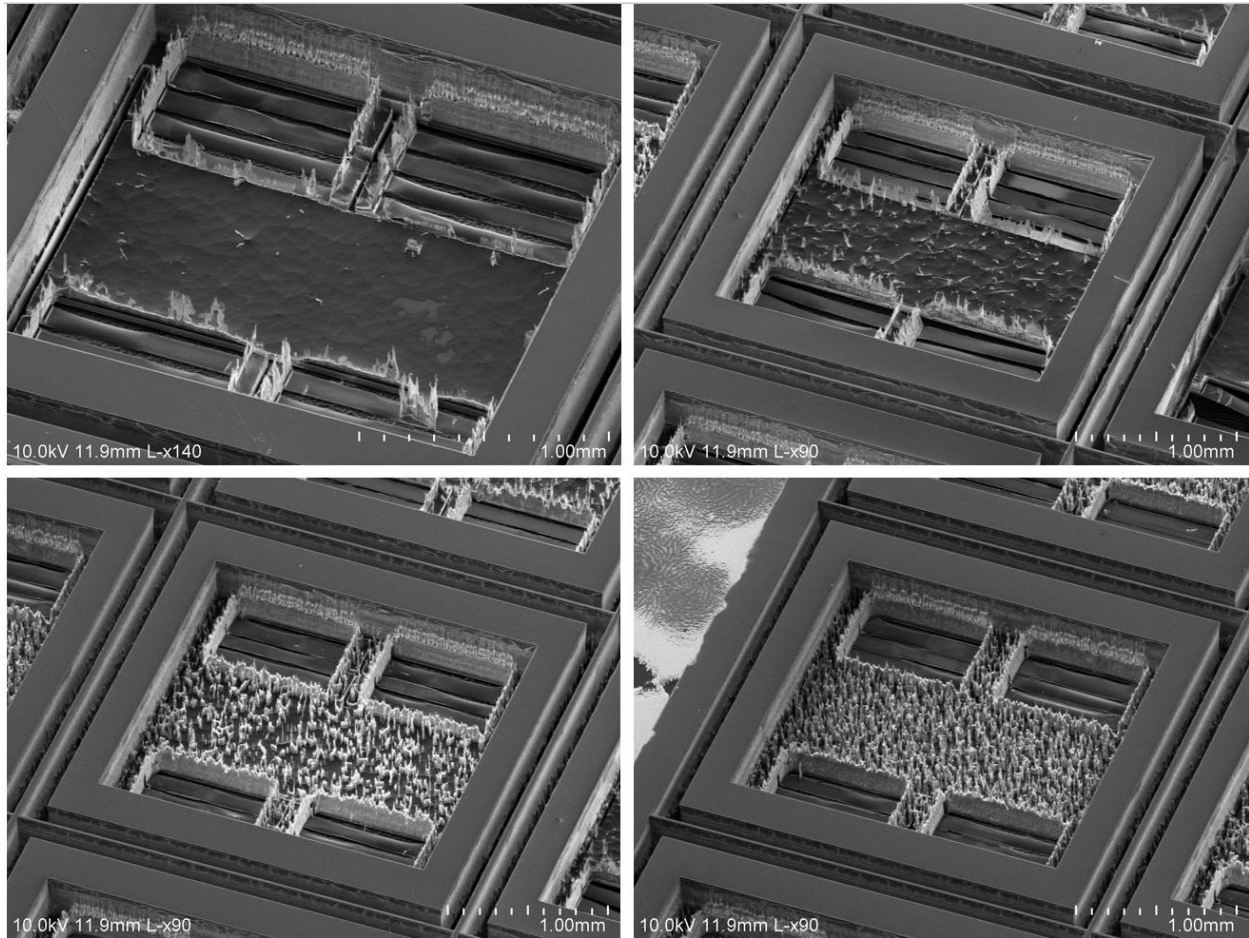


Figure 3.20. SEM images that show micro-columns formed during the DRIE release

When running a backside DRIE, the wafer is usually mounted on a handle wafer using a mounting material. When device silicon layer is completely etched, some portion of the bending legs is only about $1\mu\text{m}$ thick, and unmounting devices from the handle wafer without any damage can be challenging. One safe way is to unmount them chemically without using external agitation. For example, wafers mounted with Crystalbond can be dissolved in heated PRS2000. Additionally, “dicing lines” can be added to the DRIE patterns (both, front and backside), and they help unmount the whole wafer from the handle wafer by allowing the dies near the wafer edges to be detached first as shown in Figure 3.21. It is possible to tune DRIE recipes to perform a wafer level DRIE release, and thus for the entire flow a wafer level processing is possible. When all the dies or devices are detached, they can be rinsed in IPA last and dried on a hotplate to avoid stiction.

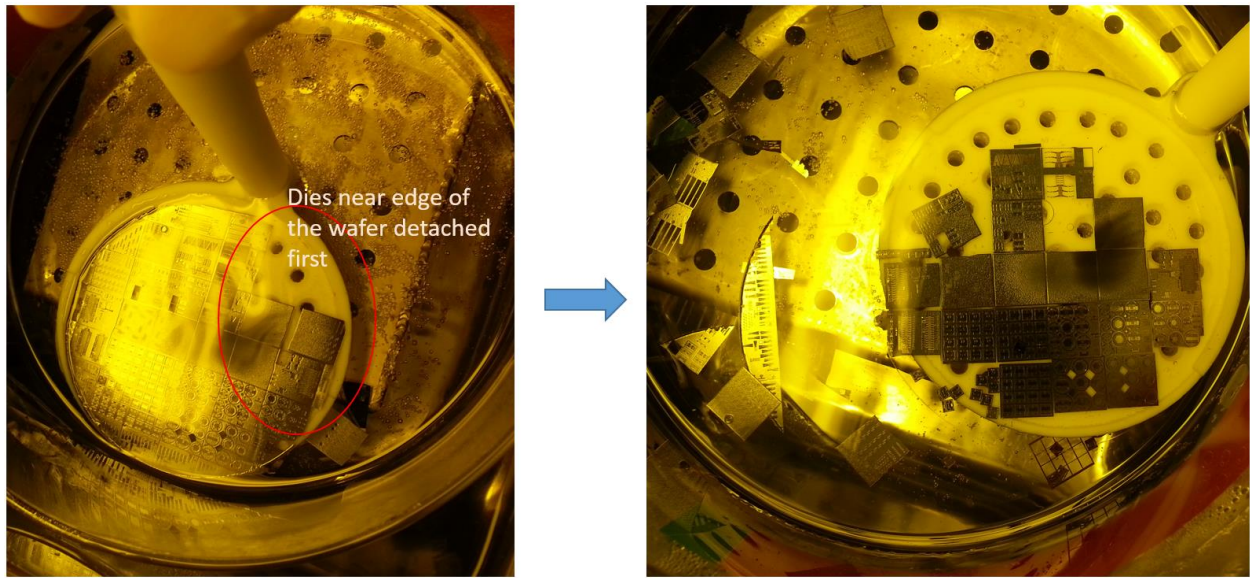


Figure 3.21. “DRIE dicing” unmounts the dies near the wafer edges first

Unfortunately, the PZT stack was observed to delaminate on some areas during the lithography for step (d) in Figure 3.14, the first topside DRIE. The bottom Pt layer might have had bad adhesion or high residual stress.

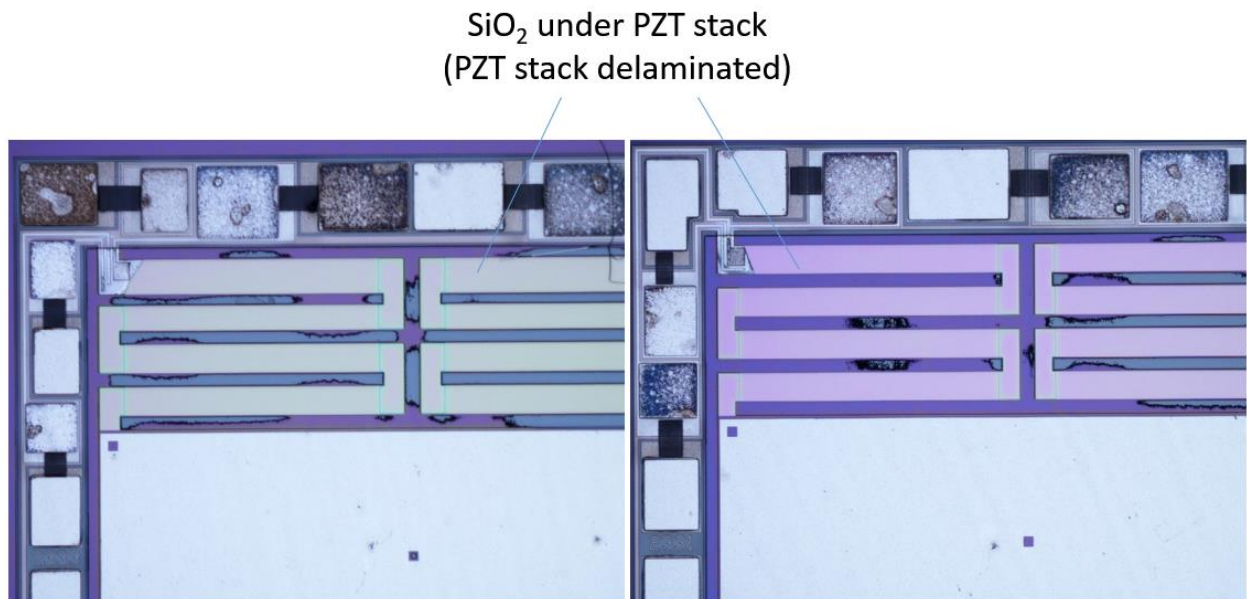


Figure 3.22. Delaminated PZT stack during process

For some devices, legs and pads were reinforced with parylene to help with adhesion as shown in Figure 3.22. This was observed to be helpful as some pads with the reinforcement were not delaminated when probed and wirebonded, when pads without the reinforcement were. Because parylene is a very soft material (low Young's modulus compared to other materials in the PZT-electrode stack), it does not affect the device performance as much, as shown in Figure 3.24. The simulation was obtained using the parameters listed in Table 2.3, and experimentally estimated elastic modulus of 1GPa was used for parylene [3.1].

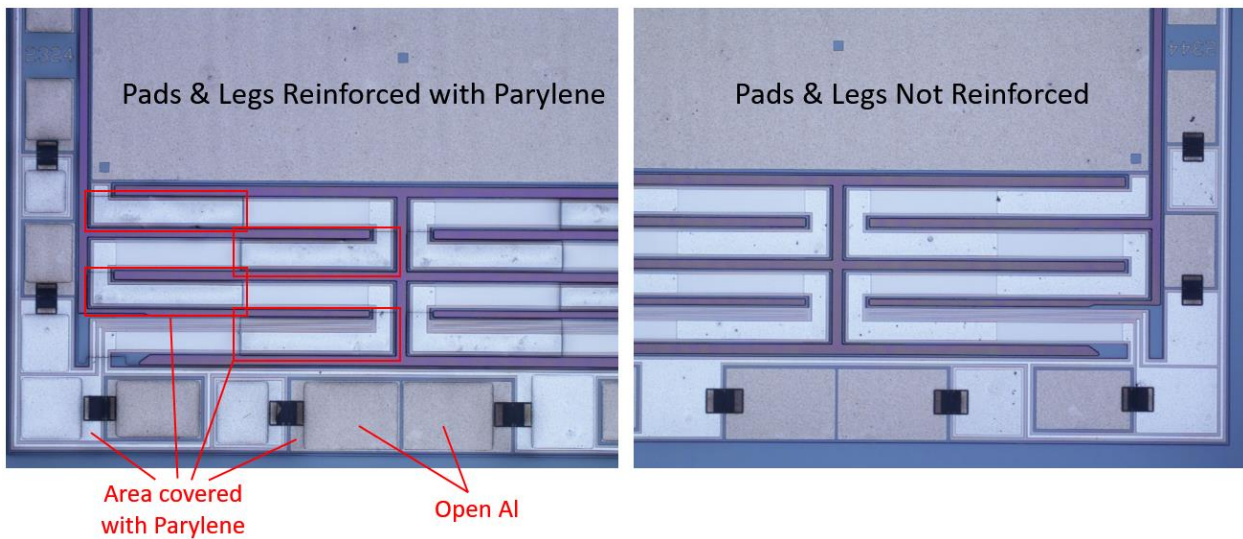


Figure 3.23. Left: sample device whose pads and legs are reinforced with parylene, Right: sample device with no reinforcement

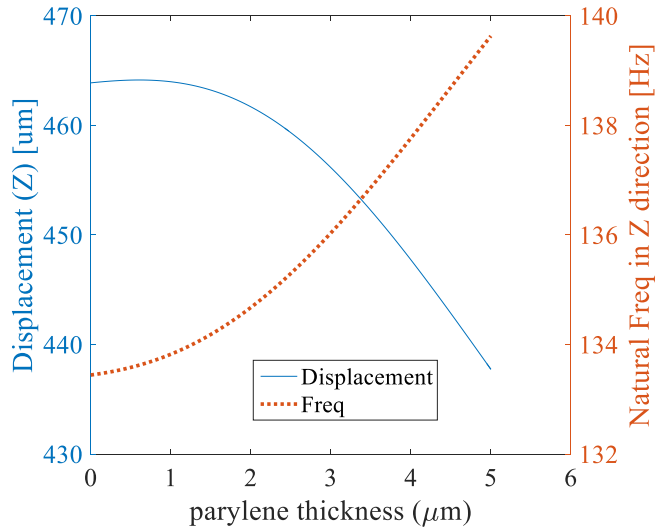


Figure 3.24. Simulated vertical displacement as a function of parylene thickness added to the bending legs

When the electrical jumpers were completed, it was confirmed that their connection was good. However, due to additional fabrication steps not shown in Figure 3.14 performed for other projects, strong ultrasonic agitation was used multiple times to clean the wafer, which might have caused delamination of the aluminum bridge by the time of actuator installation to endoscopy testbeds in some cases. Another layer of parylene for reinforcement, such as shown in Figure 3.23, right after the jumpers are completed could help with this problem. When the jumpers were confirmed to be not working, silver epoxy was manually applied to reestablish the connection between the original pads and jumper pads (Figure 3.25). Wirebonding on the aluminum bonding pads above the PZT stack was better than the gold pads in the 1st generation devices, but wirebonding on aluminum jumper pads was much easier and more reliable.

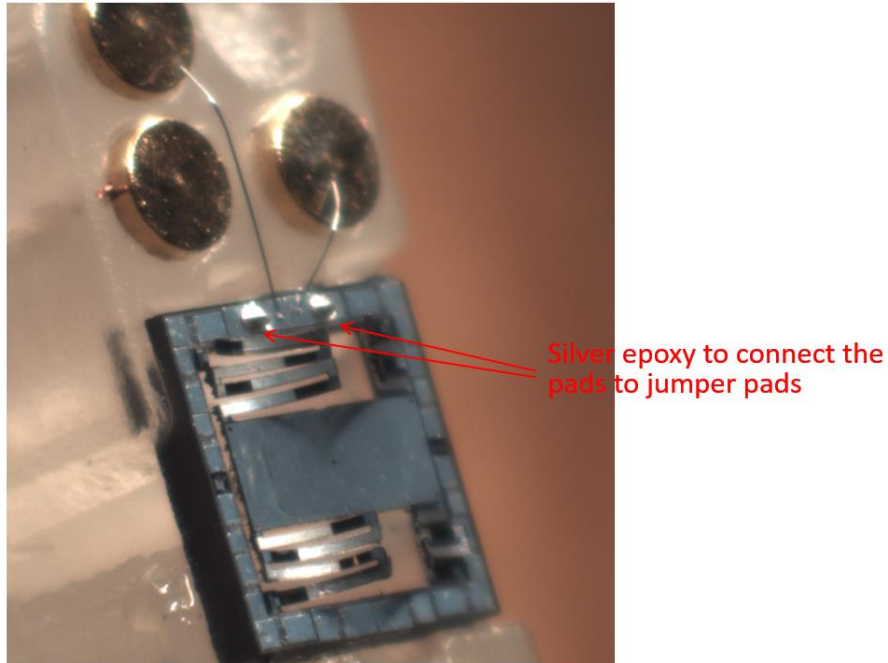


Figure 3.25. Silver epoxy applied to fix the jumpers

3. 3. Device Characterization

3. 3. 1. DC Actuation

After fabrication, static displacements of the stage were measured using Keyence's 2D Profiler LJ-V7001P and Keithley's 2400 SourceMeter. The prototype actuators have shown less than 300 μm of z-axis displacement at 14V_{DC}, which was less than the 1st generation devices. The vertical displacement was sacrificed due to the asymmetry and residual stress on bending legs that was developed from the fabrication process and observed to cause the legs to generate twisting motion, rather than pure vertical, as shown in Figure 3.26.

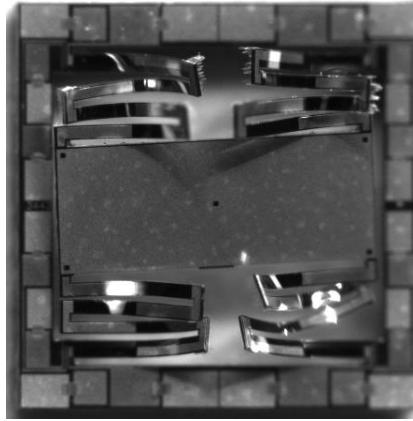


Figure 3.26. Sample actuator generating more twisting motion than vertical motion due to residual stress

In some devices, the initial tilt of the stage was too large to be compensated by a differential actuation. For example, Figure 3.27 shows a sample device where actuating a left-side leg alone is not enough to compensate the initial tilt due to residual stress. Scanners with a large initial tilt like this device are not easily used for imaging, as the current remote scan setup requires off-axis rotation less than 0.5° for vertical sectioning [2.8].

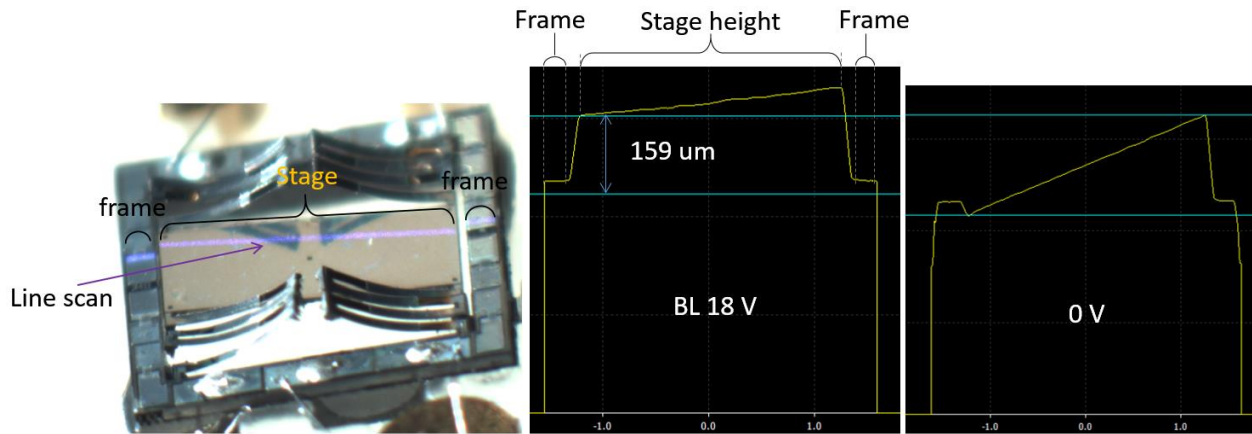


Figure 3.27. Tilt profile of the stage of a sample differential-drive actuator with large initial tilt (left: scanning laser line of the displacement sensor, center: bottom left leg actuated, right: 0V position)

Another group of devices showed initial tilting of the stage but their legs produced quite uniform displacements (Figure 3.28). This group of scanners can be used for imaging by positioning them such that initial off-axis tilt can be removed.

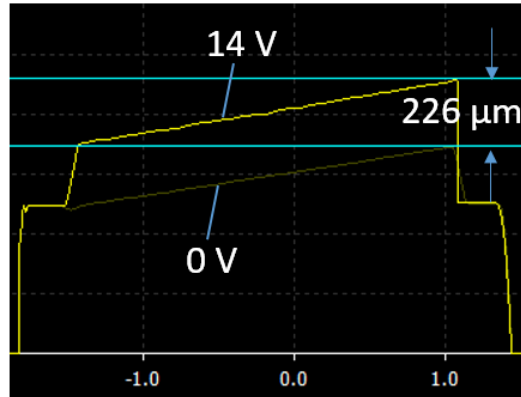


Figure 3.28. Stage height profile of a sample device when two diagonal legs were actuated with 14V

Because of large residual stress that led the actuators to produce more twisting motion and low yield due to the loss of devices from PZT delamination (Figure 3.22), measuring performance difference between the devices with 70% gold coverage on the beams and those with 50% coverage was not possible. The residual stress in the films in the PZT stack of this 2nd generation devices seemed to have much more variation in x and y plane than for 1st generation devices. Local heating occurred during exothermal etching processes [3.2] might have contributed to the large variation in residual stress. Nonetheless, the new process steps proposed in this chapter have been shown to fix all the problems observed during the fabrication of the 1st generation devices.

3. 3. 2. Isolation of Pure Vertical Motion Near Resonance

As shown in previous chapters, an important consequence of the non-idealities present in large displacement vertical stages that rely on bending beam architectures is that central stage motion can be very sensitive to asymmetries in individual legs, resulting from local variations in residual stress, photolithography misalignment, or other processing non-idealities. One way to deal with non-uniform central stage motion is to calibrate and compensate for asymmetries by applying distinct voltages to two or more legs, which requires multiple inputs. This section presents another method to achieve a uniform vertical motion using a single AC input.

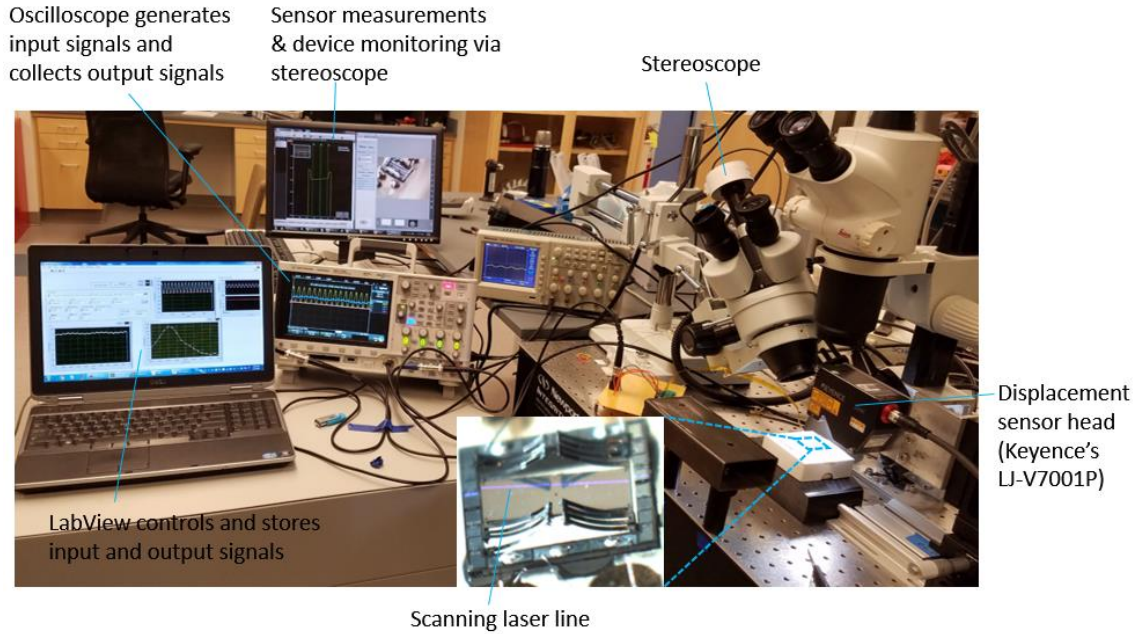


Figure 3.29. AC testing setup

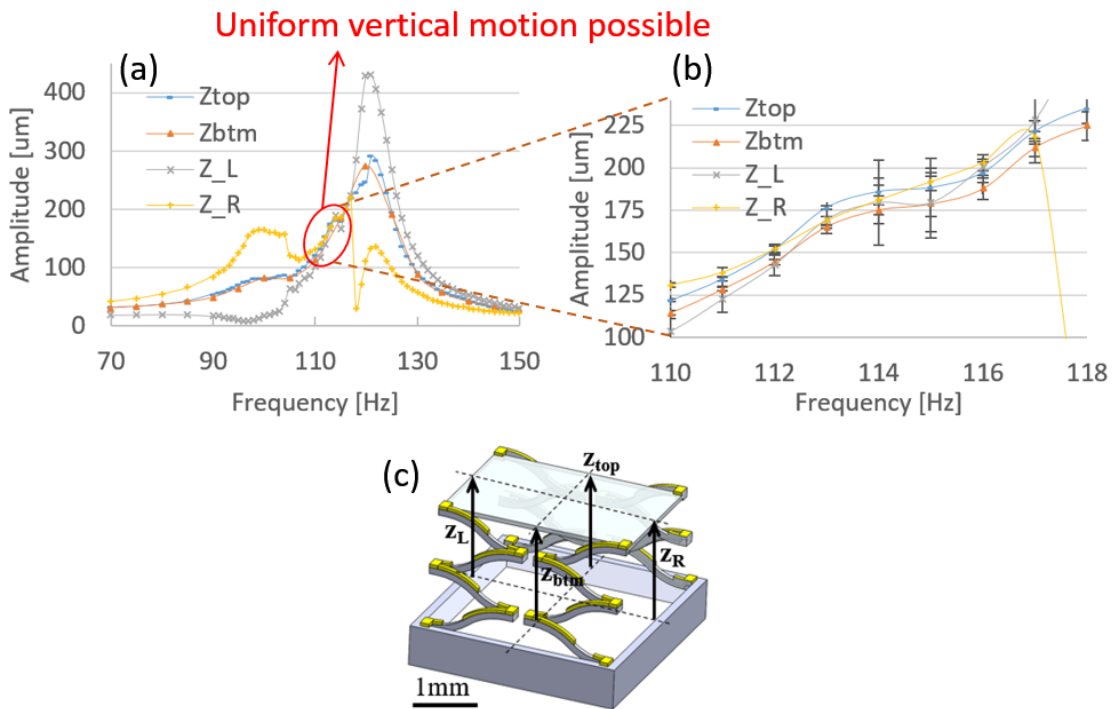


Figure 3.30. Frequency sweeping of a sample actuator with $4V_{pp}$ $2V_{off}$ sinusoidal input: (a) 70~150 Hz; (b) zoomed-in: 110~118 Hz; (c) definition of the displacements

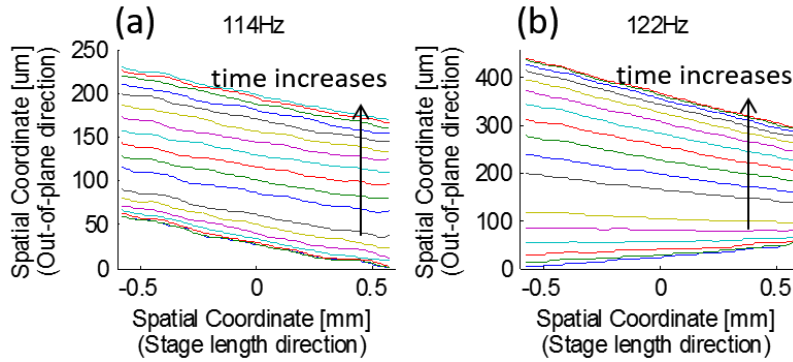


Figure 3.31. Stage motion at 114 Hz (a) and 122 Hz (b)

Using the test setup described in Figure 3.29, the dynamic response of a prototype was first evaluated using a $4V_{pp}$ $2V_{off}$ sinusoidal input, and confirmed that first dynamic modes associated with z-axis displacement and rotation about the x- and y-axes were present in the range of approximately 90-150 Hz, as shown in Figure 3.30 (a). Close proximity of vibration modes can increase complexity of dynamic actuator operation, but can also provide substantial flexibility in frequency selection to obtain varying components of vertical and rotational operation, allowing the mirror to be moved in nearly arbitrary patterns within its range of motion. After finding a frequency range where uniform out-of-plane motion can be possibly generated, the input frequency was adjusted to identify frequencies in which contributions from multiple vibration modes produce nearly pure vertical translation, allowing balancing to be performed with just a single voltage input to the stage (Figure 3.30 (b)). The error bars on the amplitudes in Figure 3.30 (b) are large not because the measurements are not repeatable but because of frequency shifts probably due to environmental changes. Such a shift can be easily adjusted during imaging using the acquired images. Figure 3.31 shows the traces of the stage motion as time increases, where coordinate 0 in x-axis is the center of the stage. The figure confirms more uniform motion at the selected frequency, although the static off-axis rotation needs to be manually adjusted for vertical motion.

To achieve vertical sectional images of mouse colon tissue using the current remote scan setup (Figure 2.21), z-axis scanning is required to operate with less than 0.5° off-axis rotation over the course of approximately $200 \mu\text{m}$ of vertical displacement [2.8]. When actuated with a single, low

frequency sinusoidal input, the sample scanner of Figure 3.30 produces 5.3° and 6.6° of tilting in the θ and ϕ directions, respectively. At 114Hz, the frequency selected to maximize pure z-axis translation, the actuator demonstrated less than 5 μm non-uniformity over a 175 μm stroke at 4 V_{pp} , or less than 0.28° off-axis rotation for a 2.4 mm by 1.0 mm mirror.

Using this near-resonance operation, the 2nd generation devices can produce a Lissajous scanning pattern in conjunction with a lateral electrostatic stage for xz-plane imaging. The benefit of this operation method is that it needs very low voltage and only one input to meet strict requirements of the remote scan architecture in use.

3. 4. Imaging Using Dynamic Balancing

3. 4. 1. 2nd Generation Actuator

With improved mirror integration and device robustness for instrument integration, and use of dynamic frequency adjustment to ensure uniform out-of-plane motion within strict requirements of the remote scan architecture in use, multiphoton imaging was tried again with the 2nd generation devices. The optical setup was identical to the one used for the imaging test with the 1st generation devices (Figure 2.21), except that here the electrostatic scanner only provides x-axis scanning to achieve real-time vertical cross-sectioning (x-z plane) imaging (Figure 3.32).

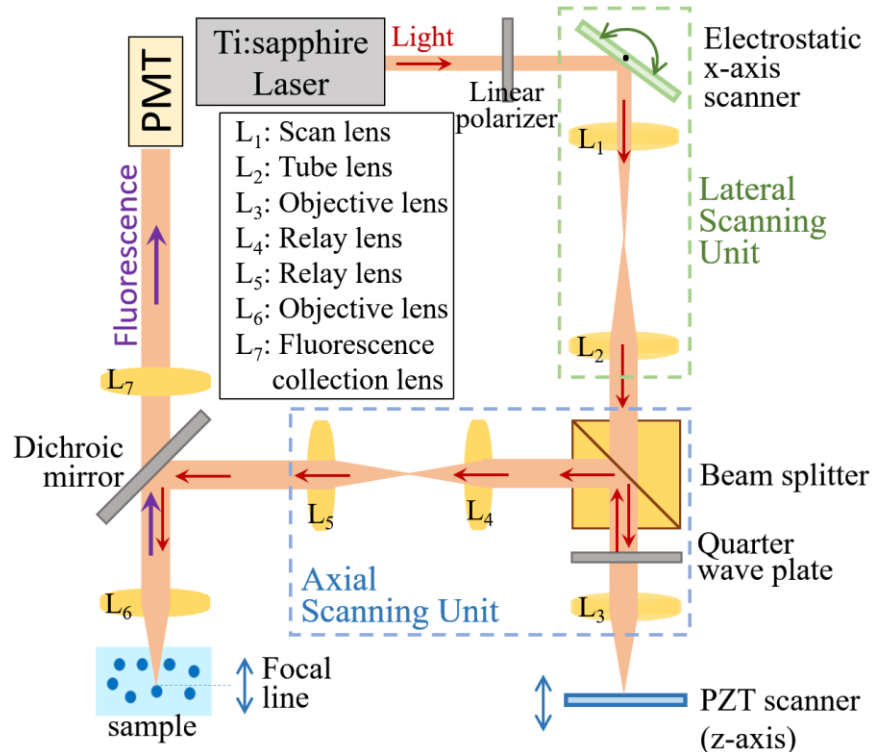


Figure 3.32. Schematic of XZ plane multiphoton imaging system using remote scan architecture

The remote scanning architecture in use here performs both axial and lateral scanning prior to the distal optics, and such an architecture can support small diameter distal optics with compact, handheld form factor. As a first step to build a small form factor imaging system, the current benchtop system was developed. The size of the PZT actuator is compatible with a small handheld imaging instrument, so a fixture was built that fits a handheld system shown in Figure 1.5 to directly implement the PZT actuator after evaluating the system performance with the benchtop system. Dealing with very small and fragile components and packaging them in a compact form factor requires to establish reliable assembly steps. The steps pictured in Figure 3.33 was developed with the collaborators in Wang Lab at the University of Michigan. The fixtures were 3D printed and 0.46mm-diameter brass alloy pins were used as connectors for 40 AWG wires and wirebonding. Epoxy was used to fix wires and secure the actuator.

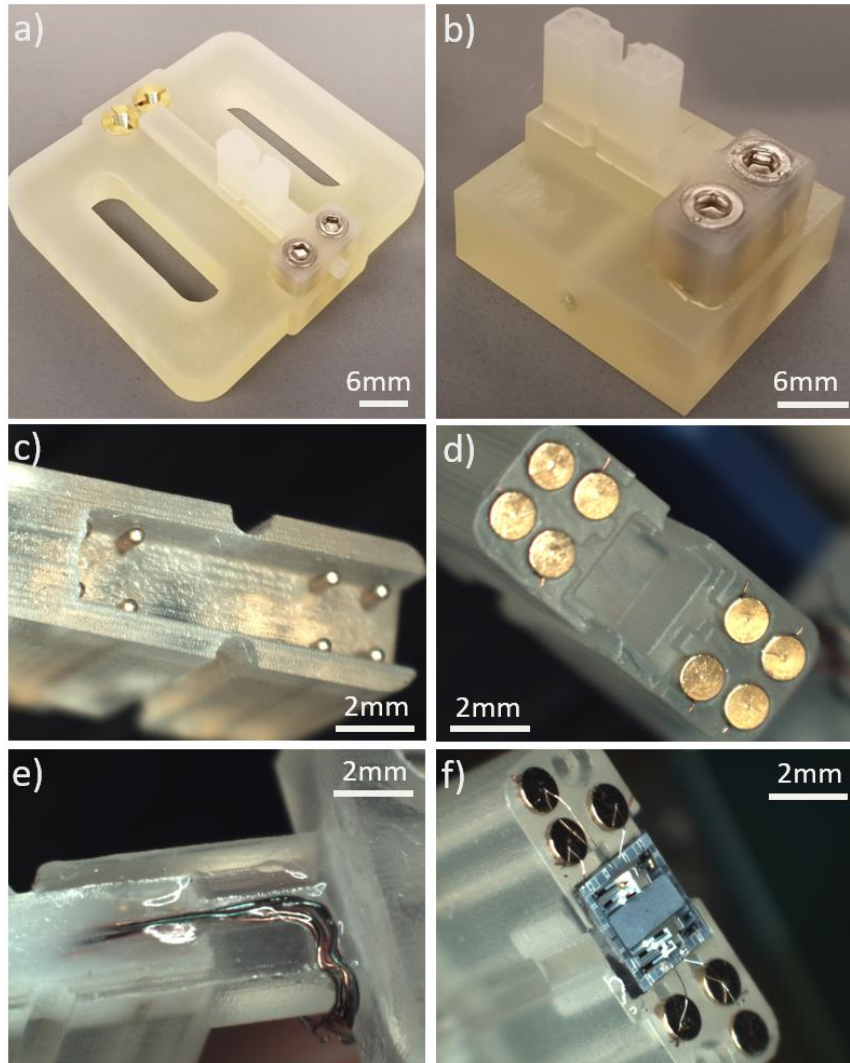


Figure 3.33. Steps to mount PZT actuator to a fixture for handheld system

After mounting the piezoelectric actuator to a fixture, the assembly was manually positioned to eliminate any static off-axis tilt of the scanning mirror such as shown in Figure 3.31 (a). The PZT scanner was then placed before the axial scan objective, L3, and uniformity of vertical scanning motion was verified. A Lissajous scan pattern combining piezoelectric axial scanning at 114 Hz (the frequency found to produce uniform vertical motion as plotted in Figure 3.31 (a)) and electrostatic lateral scanning at 9372 Hz was then initiated using Labview control software.

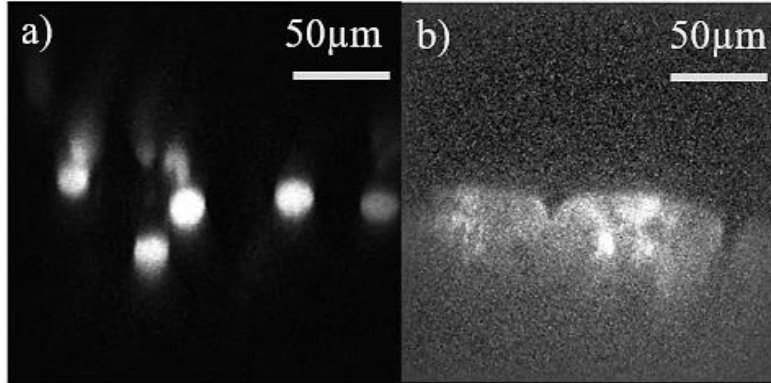


Figure 3.34. (a) 15µm-diameter fluorescent bead imaging; (b) *ex vivo* image of FITC dyed mouse colon

Sample images acquired in vertical sectioning mode are shown in Figure 3.34, where (a) shows several 15 µm diameter fluorescent beads in a polydimethylsiloxane polymer matrix and (b) a cross-section of excised mouse colon tissue dyed with fluorescein (FITC) dye. Features of the colon epithelium including surface profile and colon crypts can be distinguished. Imaging was performed using voltages of just 1.6 – 2.8 V_{pp}, less than the full range-of-motion of the device, given limited thickness of the bead phantom and FITC penetration in the sample tissue. A 60 V_{pp} sine wave at 9372 Hz used to drive the electrostatic mirror produced an x-axis scan angle of slightly less than 6°. With approximately 2X optical amplification of vertical scanning in the remote scan architecture, resulting field-of-view was approximately 300 µm by 300 µm, with axial resolution on the order of bead diameter of 15 µm.

3. 4. 2. 1st Generation Actuator with Attached Mirror

The 2nd generation devices have an integrated mirror, but its evaporated aluminum film was thought to be too thick (1µm) to provide a smooth surface, thus reducing its reflectivity and ultimately fluorescence signal. Thus, attempts to mount a 40µm-thick silicon mirror coated with 70nm of aluminum were made, and Figure 3.36 shows one successful case with a 1st generation device.

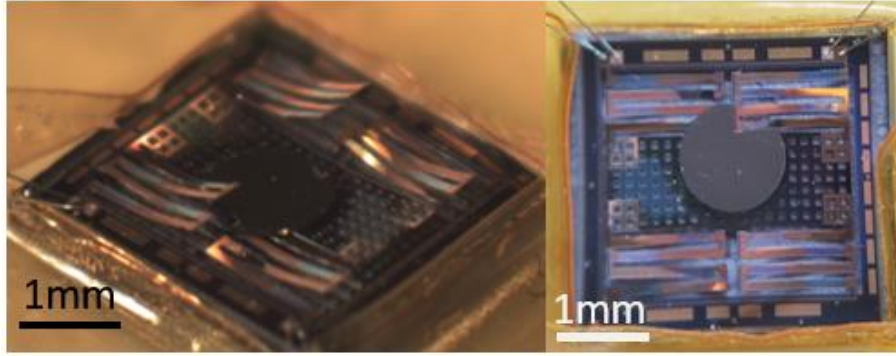


Figure 3.35. 1st generation actuator with manually mounted mirror on the stage

This device also showed non-ideal vertical motion when actuated with a low-frequency input signal. Using the same method described in Chapter 3.3.2, 140 Hz was found to be a frequency that produces a motion closest to pure vertical translation. Figure 3.36 shows its motion when driven with a $10V_{pp}$ $10V_{off}$ sine wave. The motion offset between the left and right side of the stage suggests there still exists some tilting motion.

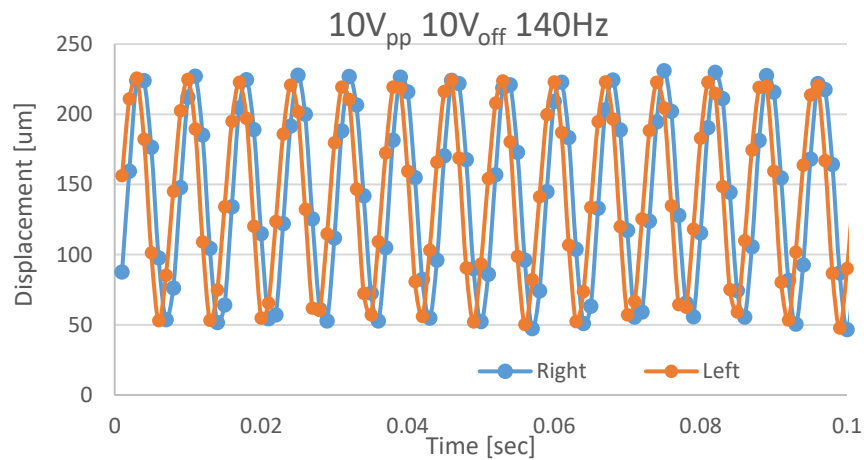


Figure 3.36. Motion of 1st generation PZT scanner with a manually mounted mirror

The same specimens as those in section 3.4.1 were imaged in the same setup, and they are presented in Figures 3.37 and 3.38. Compared with Figure 3.34, these images are clearly brighter and sharper, suggesting the smoothness of the mirror surface is an important factor. These images demonstrate the first use of a thin-film piezoelectric micro-actuator for vertical multi-photon cross-sectional imaging of tissue.

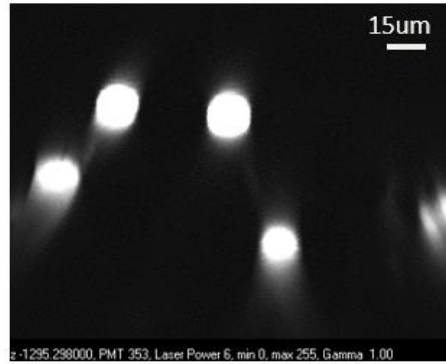


Figure 3.37. 15µm diameter fluorescent beads imaged with smoother mirror surface

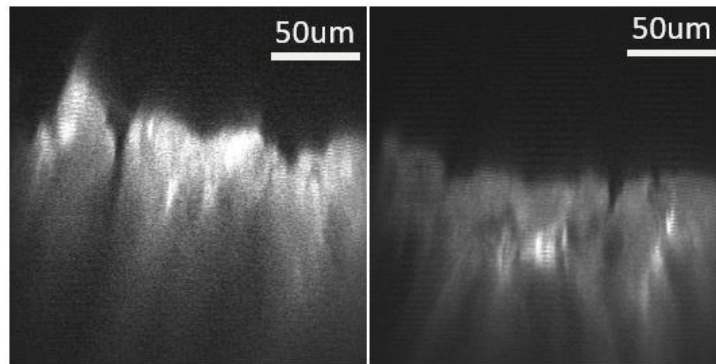


Figure 3.38. Excised FITC dyed mouse colon imaged with smoother mirror surface

The device was heated at 40-50C for longer than 30 mins to simulate the *in vivo* temperature loading, but after returning to room temperature no change in displacement was observed, suggesting that the actuator performance will be less likely affected by the body heat during *in vivo* imaging.

3. 5. Summary

Failure mechanisms of the 1st generation actuators were discussed with possible solutions. 2nd generation actuators were built using new fabrication processes developed for better yield and successful tissue imaging. The proposed solutions solved almost all issues observed during the fabrication of 1st generation devices.

2nd generation devices were characterized, and compared to the 1st generation, larger variation of residual stress within individual devices was observed, and this affected the performance of the 2nd generation actuators. Their dynamic behaviors were also characterized. Actuators have achieved large displacements (nearly 200 μm) at low voltages ($< 5 \text{ Vpp}$) near resonance. Also, a method is introduced to select a frequency to isolate pure z-axis translation from rotational components of motion about other axes, even when using a single actuation signal and in the presence of substantial fabrication non-idealities.

Multi-photon microscopy is performed for the first time using a thin-film piezoelectric microactuator for fast axial scanning in vertical cross-sectional image acquisition. Limitations of existing actuator design are minimal optimization of the scanning mirror surface, need to operate and assemble actuators with individual calibration of operating frequency for any static tilt compensation, and potential vulnerability to external vibrations.

3. 6. Reference

- [3.1] Shin, M., Choi, J., Rudy, R.Q., Kao, C., Pulskamp, J.S., Polcawich, R.G. and Oldham, K.R., 2014, August. Micro-Robotic Actuation Units Based on Thin-Film Piezoelectric and High-Aspect Ratio Polymer Structures. In ASME 2014 International Design Engineering Technical Conferences and Computers and Information in Engineering Conference (pp. V004T09A021-V004T09A021). American Society of Mechanical Engineers.
- [3.2] Gilgunn, P.J. and Fedder, G.K., 2010, January. Mechanisms of process-induced heating of MEMS structures during plasma release etch. In Micro Electro Mechanical Systems (MEMS), 2010 IEEE 23rd International Conference on (pp. 320-323). IEEE.

CHAPTER 4: MODELING

4. 1. Calibrated Static and Transient Model

4. 1. 1. Background

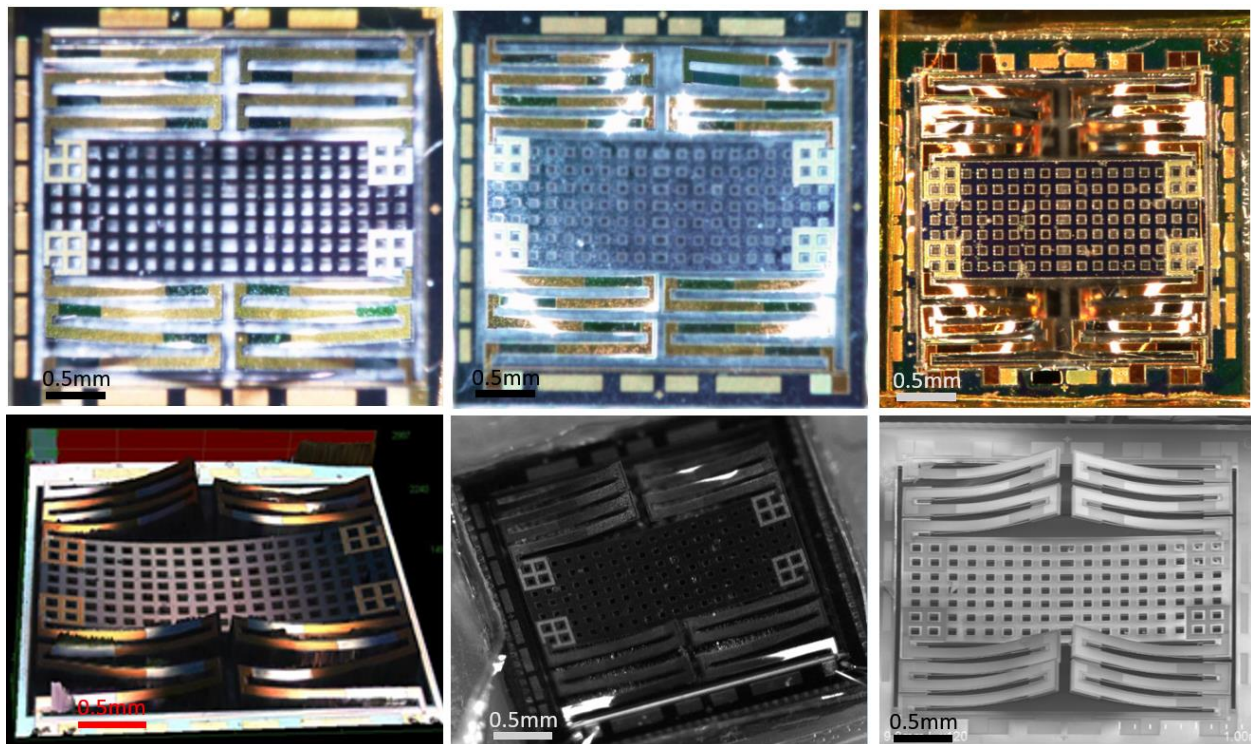


Figure 4.1. Variation in fabrication outcomes

Both characterization data of the actuators and imaging results emphasize a need for detailed development of a mechanical model of this kind of micro-actuators to understand non-ideal

outcomes after fabrication. Using MEMS fabrication techniques, it is very difficult to produce actuators such that they generate motions exactly as designed. For instance, as shown in Figure 4.1, fabricated actuators show a considerable variation in their initial deflection. As will be seen, motion is also very sensitive to small perturbations in the dimensions of individual actuation elements in the actuators developed in this work, where large vertical displacement is aggressively sought.

To deal with these uncertainties in other MEMS applications, robust controllers have been proposed, which are usually implemented on a simplified actuator model to regulate their motion [4.1-4.3]. While a robust controller with a simplified model is sufficient in some cases, there is a nearly direct trade-off between controller performance and the amount of uncertainty in the actuator model.

Modeling of a single beam within the actuation legs in this work has been reported before [2.1], while other similar multi-axis microactuators have to date been modeled using lumped parameter and finite element analysis (FEA) for design purposes [1.46, 4.4-4.6]. However, a complete structural model for an actuator with folded leg design to describe large vertical (z-axis) and rotational (about x and y axes) motion including multi-axis coupling effects has not been developed. Furthermore, previously presented models have not accounted for fabrication uncertainties such as residual stress or dimensional variances of the structure. The combination of parameter variation with multiple leg operation will be seen to be important for understanding the actuators' displacements.

Compared to bulk piezoelectric actuators, thin-film piezoelectric MEMS devices can produce much larger curvatures, influencing their dynamics. The dynamics of thin-film actuators can be also affected by unintended forces and moments generated due to asymmetric structural elements produced as a result of residual stress and dimensional variation. Effects of bonding materials in bulk piezoelectric beams are sometimes not negligible, but the adhesion layers in thin-film piezoelectrics beams so thin that they are usually lumped into the electrode layers.

More importantly, extremely large electric fields ($>100\text{kV/cm}$) are applied to piezoelectric thin-films even with modest operating voltages ($<15\text{V}$) due to their small thickness, and this can induce nonlinear material behaviors, especially in ferroelectric thin films such as PZT. In that case, nonlinear piezoelectric responses such as electrostriction, saturation effects, and domain wall motion need to be considered, in addition to linear piezoelectric response. One main cause of these nonlinearities is the existence of domain structures in ferroelectrics, which are absent in the polar materials such as ZnO and AlN [4.7-4.9].

In this chapter, a modeling technique that incorporates the effects of residual stress and dimensional variation of the structures from static motion measurements is introduced. The concept of this modeling technique can be also applied to other common types of MEMS actuators to obtain a more accurate analytic model. With this modeling technique, one can develop a MEMS actuator and its detailed model using the approach shown in Figure 4.2.

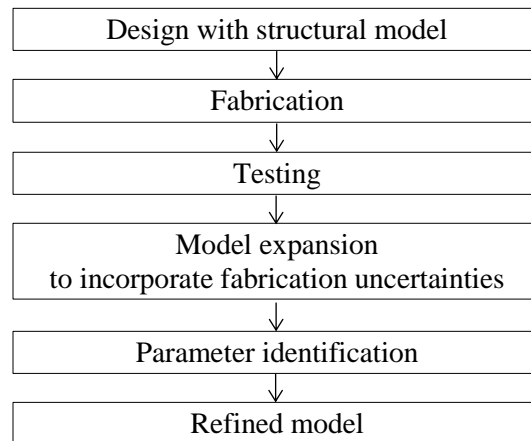


Figure 4.2. Schematic methodology for model development

Among MEMS devices, the most similar prior study to this present model identification quantified the effects of unknown factors existing in fabricated pressure sensor test structures, where measurements of dynamic behavior of the system were used in conjunction with an FEA model to find effective system parameters [4.10].

4. 1. 2. Model perturbation

If modeling the micro-actuator as designed, assuming perfect symmetry and homogenous material properties across the whole device, then in Eq. 2.13, which describes the static motion of the stage, 1) the stiffness matrix, K_n , becomes a diagonal matrix and 2) V_{coef_n} , the matrix mapping the input voltages to the piezoelectric forcing, has its elements such that each leg produces the same amount of forcing. Using this kind of ideal model, it is not possible to predict non-identical displacements of the four legs such as shown in Figures 2.11 and 2.14, which is caused most likely by structural asymmetry among the four legs, non-homogenous material properties, and non-uniform residual stresses. With current limitations of MEMS fabrication techniques, realizing perfectly symmetrical and homogenous structures is very challenging. The reasons include photolithography mask misalignment, non-uniform etching and deposition, and variation in local heating and residual stress. Thus, to predict experimentally observed behavior of the actuator more accurately, the nominal actuator model developed in Section 2.2.2 was modified to account for the variations in the segment and stage dimensions and film thicknesses as illustrated in Figures 4.3 and 4.4.

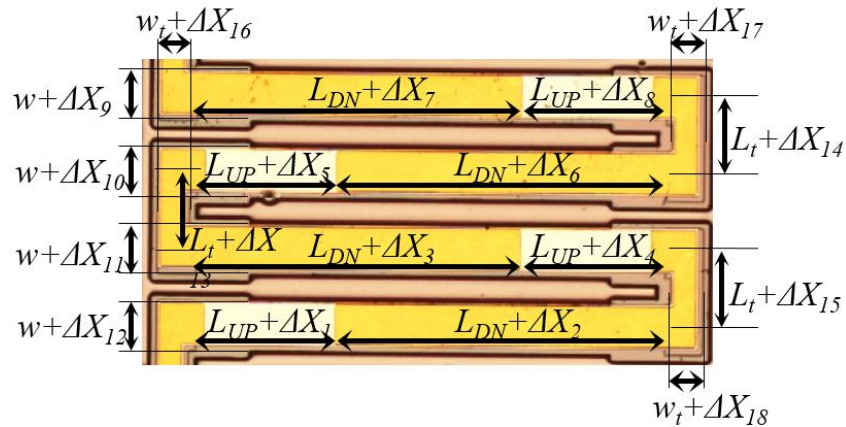


Figure 4.3. Optical microscope image of Leg labeled with allowed dimensional variation

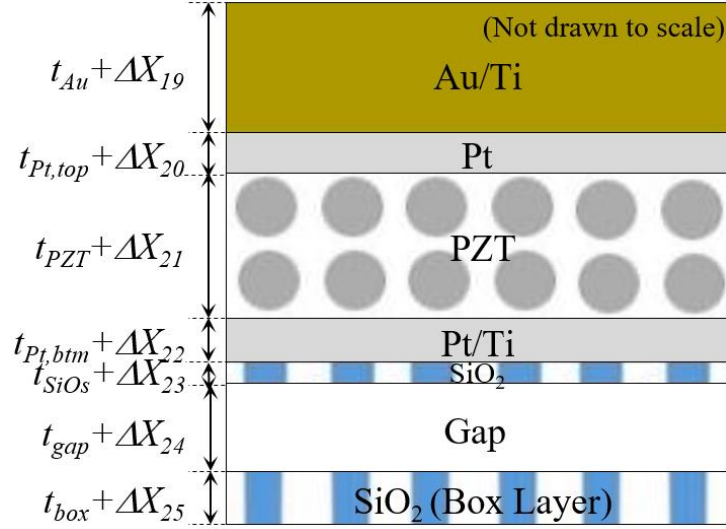


Figure 4.4. Schematic drawing of cross-section of unimorph labeled with allowed thickness variation, where Gap refers to the thickness of silicon device layer that was etched

In the perturbed model, the expression for the leg displacements, Eq. 2.8, can be rewritten as the following equation, which now represents that each leg has different compliance, piezoelectric forcing, and residual moment terms. The superscript i is used to denote each leg, and each matrix is defined in Appendix B.1. Similar to Eq. 2.8, ψ_{ext} and ψ_{int} matrices define beam compliance.

$$\bar{X}^i = \psi_{ext}^i \bar{F}^i + \psi_{int}^i d_{31,eff}(V) V^i + \bar{M}_R^i \quad (\text{Eq. 4.1})$$

When including the possible variation in the stage dimensions, Eq. 2.9 and Eq. 2.10 can also be rewritten in the same form as before but with slightly different coefficients. The equation of motion for the stage, Eq. 2.9, is modified as follows. The matrices are defined as same as those in Eq. 2.9 but with dimensional variations (*i.e.* $d = d + \Delta d$ and $w = w + \Delta w$ in the P^i matrices ($i=A, B, C, D$) that have stage dimensions as their elements as defined in Eq. 2.9).

$$J\ddot{\bar{X}} = P^A \bar{F}^A + P^B \bar{F}^B + P^C \bar{F}^C + P^D \bar{F}^D - \bar{W} \quad (\text{Eq. 4.2})$$

The physical constraints expression, Eq. 2.10, which relates the position of the center of the stage to that of each leg can be also rewritten as follows.

$$\bar{X}^i = \begin{bmatrix} \phi^i \\ \theta^i \\ z^i \end{bmatrix} = T^i \bar{X} + T_2 M_{R,\theta} + T_3^i M_{R,\phi} \quad (\text{Eq. 4.3})$$

Now following the same steps as in Section 2.2.2—that is, calculating the reaction force, moment, and torsion for each leg and plugging them into the equation of motion for the stage—the expression for the dynamic motion of the center of the stage can be obtained, assuming it can be described as a standard 2nd-order mass-spring-damper system:

$$J\ddot{\bar{X}} + C\dot{\bar{X}} + K\bar{X} = d_{31,eff}(V)V_{coef} \begin{bmatrix} V^A \\ V^B \\ V^C \\ V^D \end{bmatrix} + \bar{F}_{const} \quad (\text{Eq. 4.4})$$

The damping is assumed to be decoupled, and the gravity and residual stress terms are combined into a constant forcing term. While Eq. 4.3 and Eq. 4.4 incorporate the effects of variations in residual stress and structural dimensions so that they might be able to describe the motion of the prototype actuator more accurately, this system is largely underdetermined due to the many unknowns introduced when the model was perturbed.

The two matrix equations describing a three-degree-of-freedom system at 6 different voltage levels (0, 2, 5, 8, 11, 14V as experimentally applied for the differential-drive scanner) provide 18 equations. However, even when considering the static motion of the stage, there are a much larger number of unknowns: effective electro-active piezoelectric strain coefficient, $d_{31,eff}$, at each voltage (5 unknowns); tilting angles of the stage at each voltage (12 unknowns); residual stress term associated with each leg (8 unknowns per leg); variation in film thickness (28 unknowns per leg); variation in beam dimensions (18 unknowns per leg); variation in the stage dimensions (3 unknowns). From the experiments, only out-of-plane displacements of the stage (center and four corners) were measured at each voltage.

With knowledge about the physical system, especially fabrication tolerances, however, many of these unknowns can be bounded. For example, during the prototype fabrication sputtered or evaporated films were observed to have variations up to $\pm 20\%$ of the desired thickness. For the dimensional variations from lithography and etching processes, their bounds have been chosen to be up to $\pm 5 \mu\text{m}$. Many of the unknowns have their nominal (designed) values and their bounded minimum and maximum values as presented in Table 4.1.

Table 4.1. Nominal values of geometrical properties and their constraints and material properties for differential-drive scanner

Property	Notation	Nominal Value (x)	Constraint On $ \Delta x $
<i>Film Thickness</i>			
Au+Ti layer	t_{Au}	1 μm	$t_{Au} \times 0.2$
Top Pt layer	$t_{Pt,top}$	0.105 μm	$t_{Pt,top} \times 0.2$
PZT layer	t_{PZT}	0.8 μm	$t_{PZT} \times 0.2$
Bottom Pt+Ti layer	$t_{Pt,btm}$	0.08 μm	$t_{Pt,btm} \times 0.2$
SiO ₂ layer	t_{SiO_2}	0.17 μm	$t_{SiO_2} \times 0.2$
Buried SiO ₂ layer of SOI wafer	t_{Box}	2 μm	$t_{Box} \times 0.2$
<i>Elastic modulus of material [2.3-2.5]</i>			
Au+Ti	$E_{Au/Ti}$	86 GPa	-
Pt	E_{Pt}	170 GPa	-
PZT	E_{PZT}	70 GPa	-
SiO ₂	E_{SiO_2}	80 GPa	-
Si	E_{Si}	169 GPa	-
<i>Beam Property</i>			
Width of beam	w	100 μm	5 μm
L of segment w/o Au	L_{UP}	354 μm	5 μm
L of segment w/ Au	L_{DN}	823 μm	5 μm
GJ of beam	$(GJ)_{comp}$	76.41 $\mu\text{N}\cdot\text{mm}^2$	-
Width of torsional beam	W_t	80.5 μm	5 μm
L of torsional beam	L_t	170 μm	5 μm
GJ of torsional beam	$(GJ)_{t,comp}$	36.95 $\text{mN}\cdot\text{mm}^2$	-
<i>Stage Property</i>			
Width of stage	w_{stg}	1024 μm	5 μm
Length of stage	d	2764 μm	5 μm
Thickness of stage	t_{si}	30 μm	$t_{si} \times 0.2$
Mass of stage	m	162 μg	-

Rotational Inertia of stage (ϑ dir.)	J_{ϑ}	105.7 $\mu\text{g}\cdot\text{mm}^2$	-
Rotational Inertia of stage (φ dir.)	J_{φ}	14.7 $\mu\text{g}\cdot\text{mm}^2$	-

Other parameter values, when available, were determined as follows: The titanium layer, used as an adhesion layer for the gold layer, was very thin, compared to the gold layer, so its properties were lumped in those of gold. The bending stiffnesses of the segments, $(EI)_{UP}$ and $(EI)_{DN}$, were calculated based on the location of neutral axis of each film relative to the common neutral axis of the compound. The buried SiO_2 layer of a unimorph was treated as a spring in parallel with the PZT-Au stack. The mass properties were estimated using computer-aided design (CAD) software.

The product of shear modulus and polar moment of inertia, GJ , was obtained using linear finite element analysis (FEA) because of its nonuniform cross section along the length. As shown in Figure 4.5, three different cases were simulated to see the effects of the geomtry: 1) the buried silicon dioxide layer remains parallel to the PZT stack after releasing, 2) the buried silicon dioxide layer sticks to the PZT stack, and 3) the buried silicon dioxide breaks and is no longer present. Different amount of torsion was applied to each geometry, and the twist of the beam was measured as shown in Figure 4.6. If a linear relationship between the applied torsion and the twist is assumed, as expressed in Eq. 2.6., the torsional rigidity for each case can be obtained using the slope (Table 4.2). Generally speaking, different cases were observed, depending on the thickness of buried SiO_2 . For the devices that has the same box layer thickness as the tested device here, Case 1 was more commonly observed, so Case 1 was used for modeling.

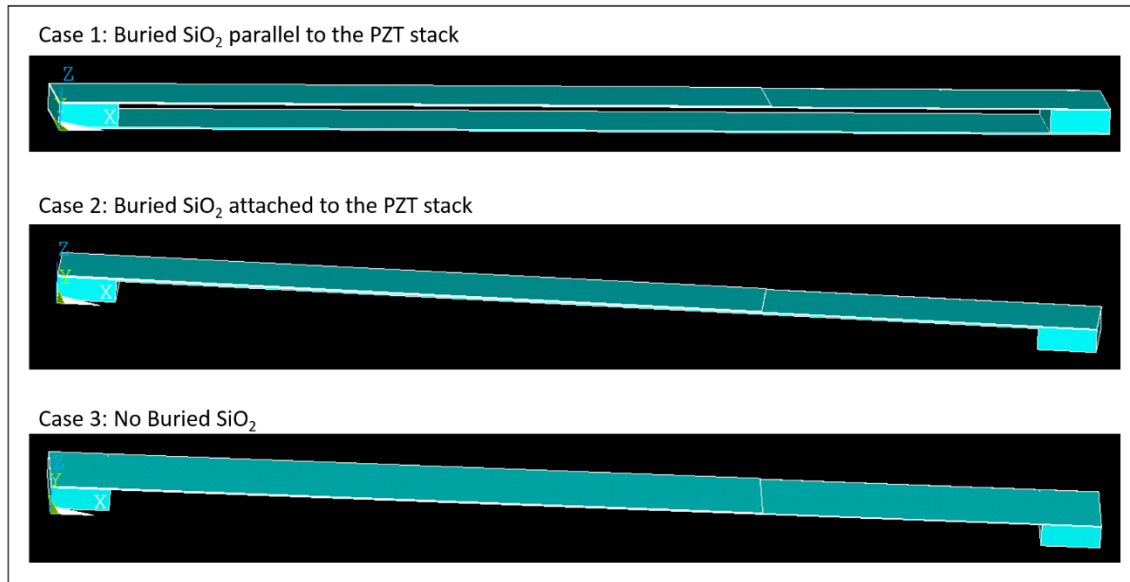


Figure 4.5. Different beam geometries used for FEA to obtain torsional stiffness of Beam

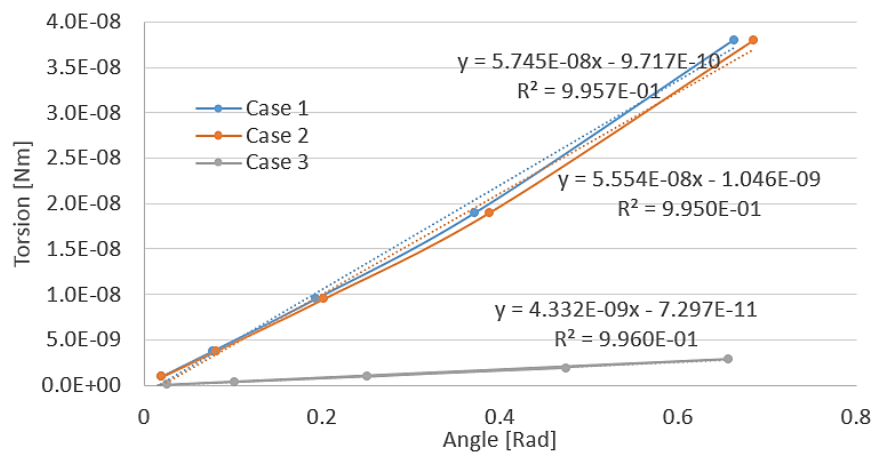


Figure 4.6. FEA results, where slopes represent torsional stiffness

Table 4.2. Obtained torsional stiffness for each geometry (Au coverage=70%)

	Slope (Torsion/angle) [Nm/rad]	Length of the beam (L) [m]	Torsional stiffness (GJ) [Nm ² /rad]
Case 1	5.7450E-08	1.3300E-03	7.6409E-11
Case 2	5.5540E-08	1.3300E-03	7.3868E-11
Case 3	4.3320E-09	1.3300E-03	5.7616E-12

4. 1. 3. Parameter fitting results

4. 1. 3. 1. Differential-drive scanner

To begin identifying the refined model of a fabricated actuator, the terms related to the residual stresses and initial stage tilting angles can be obtained using the experimentally measured stage displacements at 0V. Then, using experimental static displacements at non-zero voltages and the expressions for the motion of the legs and stage, Eq. 4.3 and Eq. 4.4, one can estimate the value of $d_{31,eff}$ at each voltage, and can compute the static displacements (z, z_A, z_B, z_C, z_D) at each voltage (2, 5, 8, 11, 14V) in each actuation mode (out-of-plane, tilting about x and y axes). The computed static displacements can be compared to experimentally measured displacements. Hence, this can be viewed as a bounded-input optimization problem written as follows.

$$\min_x \left\{ \sum_{\theta, \phi, z} \left(\sum_{\substack{i=2,5,8, \\ 11,14V}} \sum_{\substack{j=A,B,C,D, \\ center}} |z_{j,calculated}^i - z_{j,measured}^i| \right) \right\} \quad (\text{Eq. 4.5})$$

where x is a vector of the perturbed values of the geometrical properties of the scanner to be found.

This constrained nonlinear optimization problem was solved for the unknowns that can best predict the experimental static behavior of the stage in all three actuation modes simultaneously by sequential quadratic programming. As indicated in Table 4.1, the material and mass properties were not varied.

To see the effectiveness of modeling the variation, the optimization problem was also solved with different degrees of allowed variation, and the results are presented in Table 4.3. In the table, no variation refers to when all the parameters are assumed to be as designed; beam-wise global, when all the beams are constrained to have same properties so that the unknowns for only one global beam are solved; leg-wise global, when all the legs are constrained to have same

properties so that the unknowns for only one global leg are solved; local variation, when each beam has different properties.

Table 4.3. Errors in μm between the measured and computed displacements as the number of possible parameter variation is increased

		No Variation	Beam-wise global	Leg-wise global	Local Variation
# of variable optimized		0	14	45	171
Actuation Mode	z	16.75	16.75	16.75	12.34
	ϕ	24.10	24.08	24.07	11.45
	θ	42.26	40.68	19.83	19.89
Total average error		27.70	27.17	20.22	14.56

As expected, the greater the number of the beams and legs that are allowed to have their own uncertainties, the more accurately the model captures the static motion of the prototype actuator. In the case where each leg is allowed to have its own variation, the reason why as many as 171 optimized variables were not able to produce a smaller error may be attributed to what the model does not account for such as non-uniform $d_{31,eff}$ coefficient across the device at a fixed voltage (as it can also vary as a function of strain), higher order piezoelectric effects (e.g. electrostriction), non-linear beam bending, and discrepancy in material properties (as deposition process can change mechanical properties of thin-film material).

For visual representation of the results, they are plotted in Figures 4.7, 4.8, and 4.9. Further analysis shows that the variation in the film thicknesses contributes to the asymmetry of the actuator more than the variation in the beam dimensions—that is, the model predicts better with looser bounds on the film thicknesses than with looser bounds on the beam dimensions. Hysteresis behavior of PZT was modeled by allowing the effective electro-active piezoelectric strain coefficient, $d_{31,eff}$, to vary as a function of voltage, and the estimated $d_{31,eff}$ values are plotted in Figure 4.10.

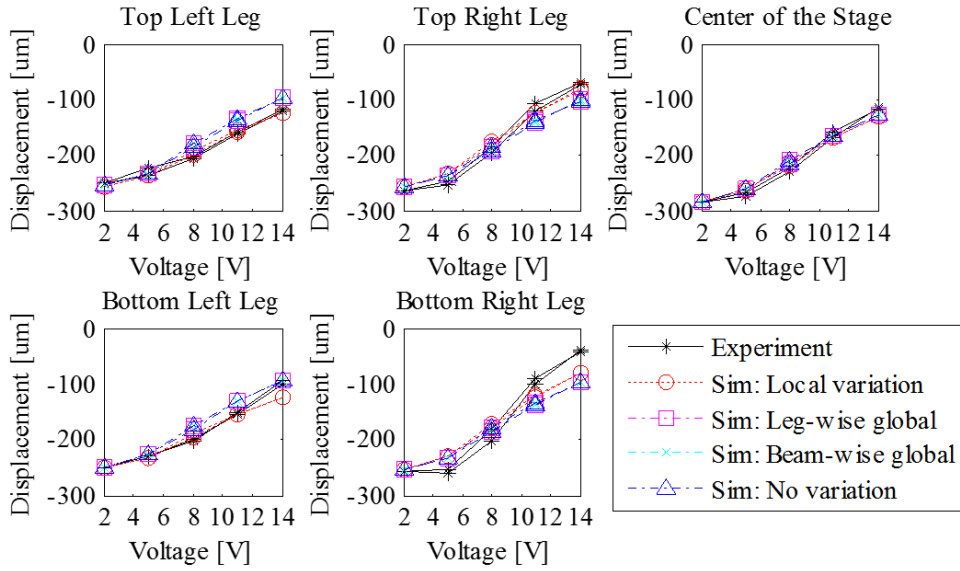


Figure 4.7. Parameter fitting results of static displacements when Legs A & D (translational Z) are actuated

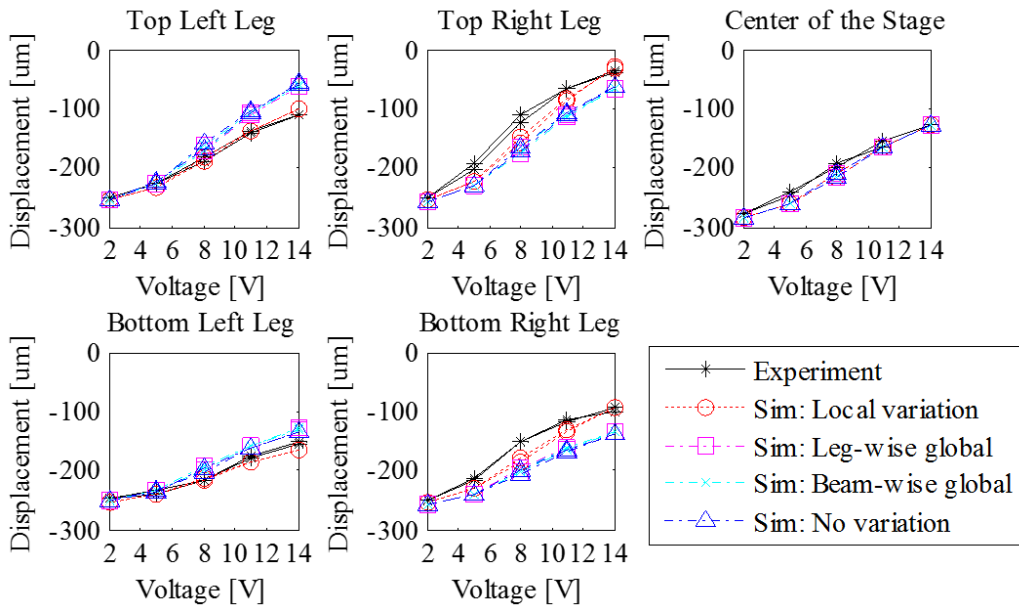


Figure 4.8. Parameter fitting results of static displacements when Legs A & B (rotational about Y; ϕ) are actuated

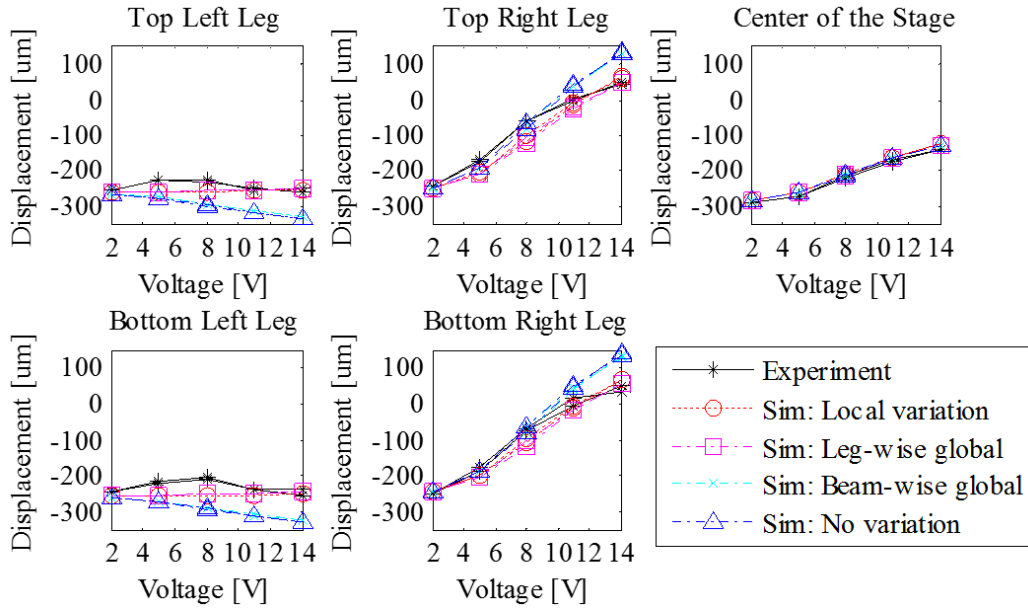


Figure 4.9. Parameter fitting results of static displacements when Legs B & D (rotational about x ; θ) are actuated

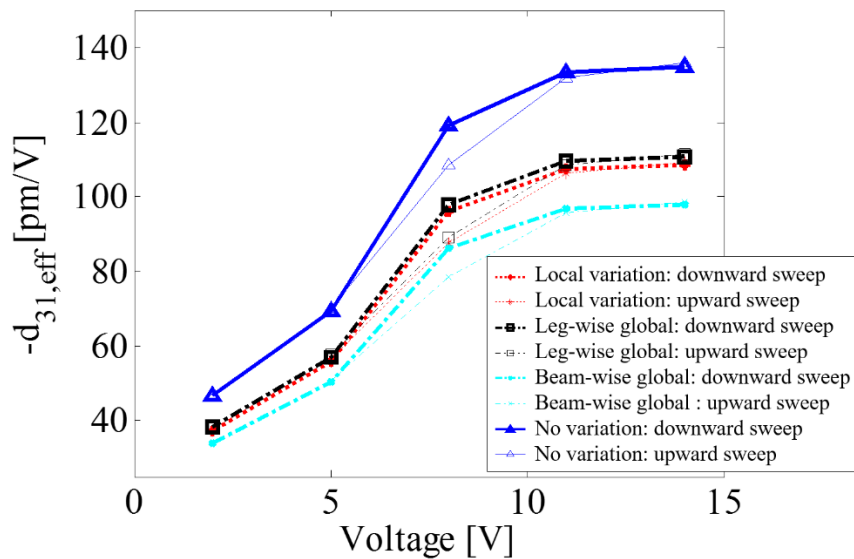


Figure 4.10. Estimated effective electro-active piezoelectric strain coefficient, $d_{31,eff}$

With the identified parameters of the static model above, a dynamic model can be obtained by simply finding the damping term in Eq. 3.16. Assuming a decoupled damping, the damping coefficients that give good agreements with experimental measurements A and B in Figure 2.16 were found by trial and error. Point A refers to the measurements taken at the center of the

stage at 11V, and Point B to those at the bottom left corner of the stage at 11V. Table 4.4 shows some characteristics of filtered transient response of both experimental and simulation results, where the local variation is referred to as a perturbed model and the no variation as a nominal model. The moving average filter in the experimental system could reduce observed overshoot by up to about 10 %, and increase the measured peak time and settling time by about 3 msec and 6 msec, respectively. In the experiments, it is observed that the transient response of the legs includes different modes of vibration, resulting in a shorter period when averaged than the period of the response at the center of the stage. Only the first vibration mode was considered because it was fast enough to achieve the bandwidth needed for real-time imaging without any motion artifacts.

Table 4.4. Transient response of the stage

In figure 3.4	Result	Avg period (ms)	Peak time (ms)	Over-shoot (%)	S.S. error (μm)	Settling Time, 5% (ms)	
Point A	Experiment	12.0	10.2	16.4	-	23.44	
	Sim	Perturbed	12.8	10.8	16.4	-0.5	17.98
		Nominal	10.4	9.9	15.2	-4.03	16.38
Point B	Experiment	11.2	13.0	12.8	-	43.1	
	Sim	Perturbed	10.0	9.9	10.4	1.15	39.6
		Nominal	10.4	9.9	15.2	-21.51	16.5

In general, the model accounting for parameter variation across the whole device captures the structural dynamic behavior of the center of the stage well, although it predicts the settling time to be faster than experimental results. In estimating the dynamic behavior of the legs, the perturbed model can represent the presence of other excited vibration modes better than the nominal model, although its averaged period is less accurate in comparison with the experimental result.

4. 1. 3. 2. Non-differential-drive scanner

In the same way that the parameter fitting technique was applied to the testing results of the differential-drive scanner, the method was applied to those of the non-differential-drive scanner. The prototype non-differential-drive scanner tested has slightly different geometrical properties from the differential-drive scanner analyzed in the previous section. The parameters used are listed in Table 4.5. Different from the case of the beams of differential-drive scanner, it was observed that the buried SiO₂ adheres to the base SiO₂ layer under the PZT stack. It is most likely because the gap between those two layers, *i.e.* the thickness of the silicon device layer, is smaller and the buried SiO₂ layer is thinner for the beams of the tested non-differential-drive scanner than those of the differential-drive scanner. Hence, those two layers were modeled as one layer. In addition, this type of scanner only actuates translationally during nominal motion, it was assumed that the torsional bending of the beams is small and thus neglected.

Table 4.5. Nominal values of geometrical properties and their constraints and material properties for non-differential-drive scanner

Property	Notation	Nominal Value (x)	Constraint on $ \Delta x $
<i>Film Thickness</i>			
Au+Ti layer	t_{Au}	1 μ m	$t_{Au} \times 0.35$
Top Pt layer	$t_{Pt,top}$	0.105 μ m	$t_{Pt,top} \times 0.35$
PZT layer	t_{PZT}	0.8 μ m	$t_{PZT} \times 0.35$
Bottom Pt+Ti layer	$t_{Pt,btm}$	0.08 μ m	$t_{Pt,btm} \times 0.35$
SiO ₂ layer	t_{SiO2}	0.5 μ m	$t_{SiO2} \times 0.35$
<i>Elastic modulus of Film material</i>			
Au+Ti	$E_{Au/Ti}$	86GPa	-
Pt	E_{Pt}	170GPa	-
PZT	E_{PZT}	70GPa	-
SiO ₂	E_{SiO2}	80GPa	-
<i>Beam Dimension</i>			
Width of beam	w	100 μ m	5 μ m
Length of segment w/o Au layer	L_1	540 μ m	5 μ m
Length of segment w/ Au layer	L_2	755 μ m	5 μ m
<i>Stage Property</i>			
Width of stage	w_{stg}	1024 μ m	5 μ m
Length of stage	d	2718 μ m	5 μ m

Thickness of stage	thk_{stg}	10 μm	3 μm
Mass of stage	m	44.5 μg	-
Rotational inertia of stage (ϑ direction)	J_{ϑ}	32 $\mu\text{g}\cdot\text{mm}^2$	-
Rotational inertia of stage (φ direction)	J_{φ}	4.06 $\mu\text{g}\cdot\text{mm}^2$	-

The parameter fitting results with local variation is presented in Figure 4.11. The average error in the calculated displacements of all the four corners of the stage over the whole range of the applied voltage compared to the measured displacements was found to be about 17.4 μm .

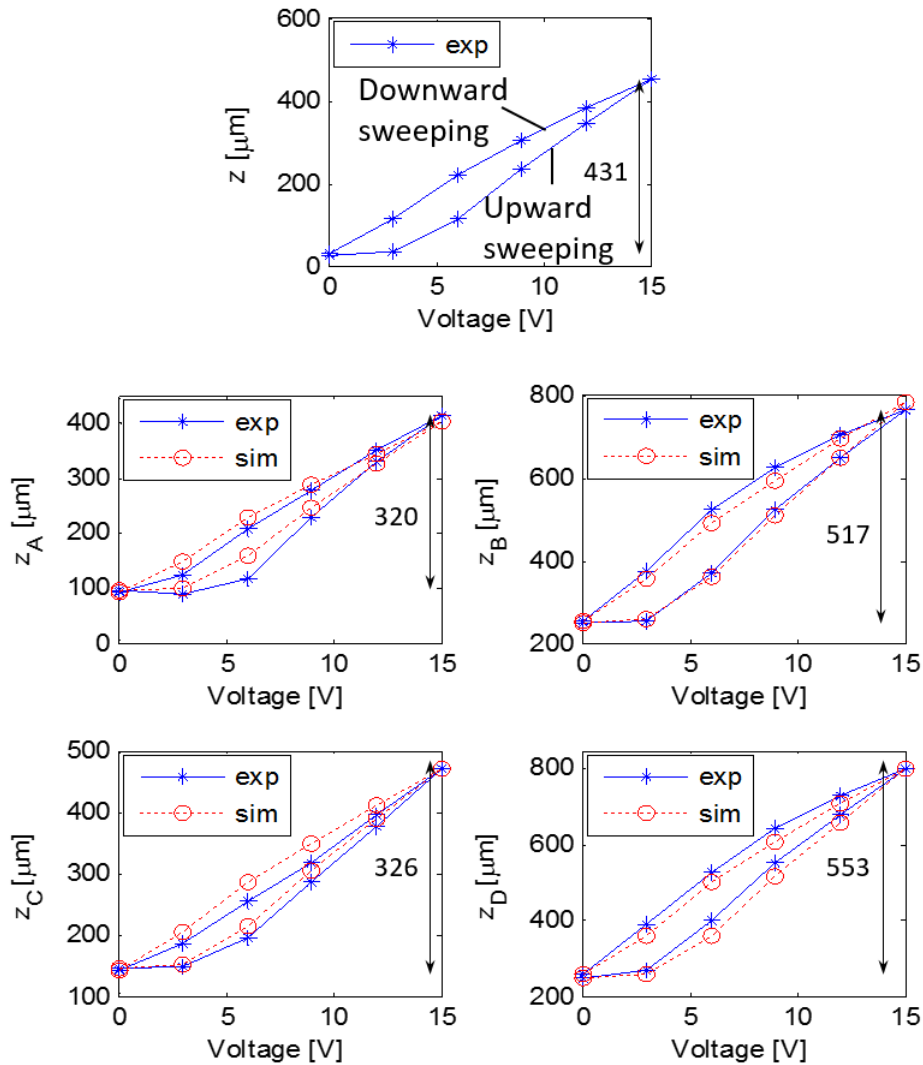


Figure 4.11. Parameter fitting results of static displacements of non-differentia-drive scanner

Again, the hysteresis observed in the static displacement tests was captured in the model by allowing the $d_{31,eff}$ value to vary. The estimated $d_{31,eff}$ values obtained by solving the optimization problem are shown in Figure 4.12. For accurate control of the motion of the stage, knowing the hysteresis behavior is important as it affects the system as an input as expressed in Eq. 3.12 and Eq. 3.16.

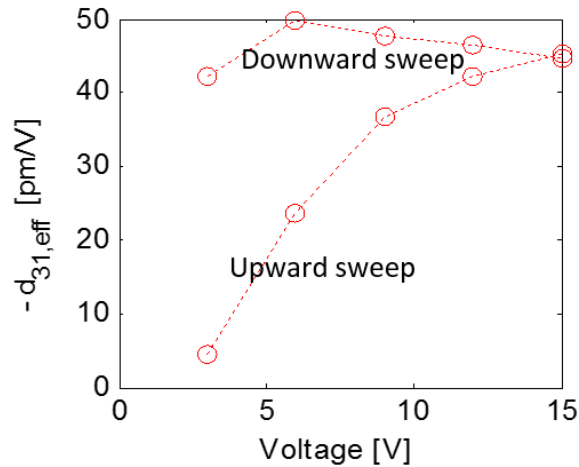


Figure 4.12. Estimated effective electro-active piezoelectric strain coefficient, $d_{31,eff}$

As before, a dynamic model of the prototype scanner has been obtained as shown in Figure 4.13. This also serves as a way of checking the validity of the obtained solution to the static model since solving problems such as this where the number of unknowns is greater than the number of the given equations there are more than one solution that satisfies the bounds. As mentioned earlier, the steady state displacement of dynamic testing ($\sim 30 \mu\text{m}$) is evidently smaller than the static displacement (z_0 : $\sim 80 \mu\text{m}$) at 5 V (Figure 2.12) because the thin-film PZT was not poled properly and a time varying input voltage was applied. Modifying the effective electro-active piezoelectric strain coefficient to match the steady state displacement and tuning the damping coefficients, a model that can fairly capture the dynamic response of the prototype has been obtained. The simulation result in the right graph was produced with $d_{31,eff} = -7.6239 \text{ pm/V}$ and the result in the left graph with $d_{31,eff} = -15 \text{ pm/V}$

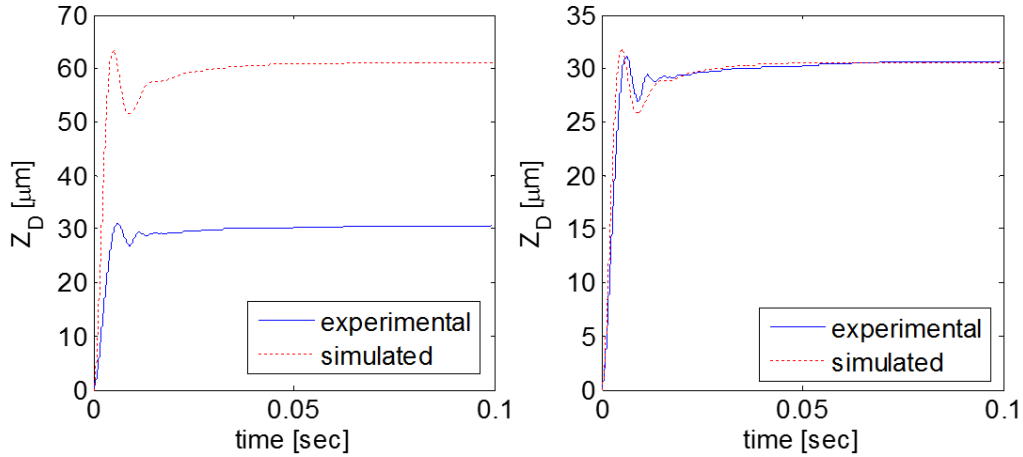


Figure 4.13. Transient response of the stage (left: $d_{31,eff}$ unadjusted; right: $d_{31,eff}$ adjusted)

4. 1. 4. Summary

Based on the experimental static displacements of the stage at various voltages, a parameter fitting technique was applied to the structural model in order to identify the effects of variation in structural dimensions and residual stress developed during the fabrication process. A reasonable agreement between the experimental and modeling results, both statically and dynamically, showed the effectiveness of the presented system identification method, where a large number of unknown parameters were identified using only a limited number of available measurements. The modeling results also show that non-uniform residual stress and variation in structural dimensions present across the prototype actuator significantly affects the system behavior. By including their effects the model captured the experimental motion of the actuator more accurately. This modeling technique can be used for other flexure-based MEMS devices to refine model accuracy, which will allow for the use of more aggressive control schemes.

4. 2. Dynamics Over Large Vertical Stroke

4. 2. 1. Background

MEMS based scanners that can provide large scan range with high dynamic bandwidth in small form factor have made substantial impact in various applications, such as biomedical imaging [1.33, 1.34, 4.11], portable projectors [4.12, 4.13], and high-resolution displays [4.14, 4.15]. Many of the MEMS scanners in these applications are designed to be operated at resonance to meet high performance requirements such as large and fast deflection [1.34, 4.11-4.15]. Better performance near resonance can also allow low voltage input or non-hermetic packaging. For proper resonant mode operation, the dynamic behavior of a device such as mode coupling and resonant frequencies needs to be characterized.

Due to their large energy densities, thin-film piezoelectric materials have potential to achieve similar performance to resonant optical scanners under static conditions, or to dramatically reduce voltage requirements for resonant operation. Static and resonant operation may even be mixed, targeting resonant motion in certain axes to complement specific static translations or rotations. To find the best operating strategy for large deflection scanning actuators capable of static or resonant operation, it is necessary to understand the influence of large translations or rotations on actuator dynamics.

This section reports the experimental observation and modeling of the shift of the natural frequency, due to the increase of a dc bias voltage, of a large displacement piezoelectric micro-scanner of this work (Figure 4.14) that has symmetric serpentine springs, one of the common spring designs in MEMS devices.

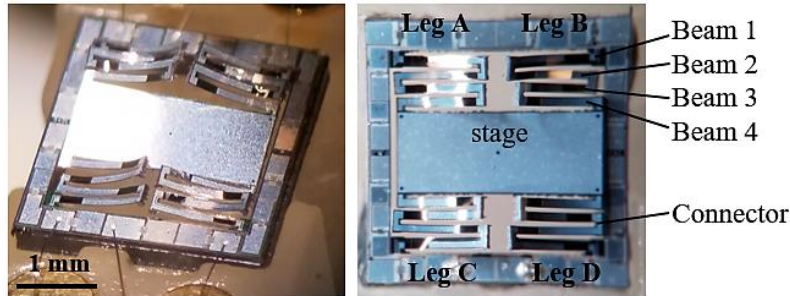


Figure 4.14. Optical Images of 2nd generation PZT scanners, labelled with definitions of legs and beams

Due to its symmetric design, these scanners are sensitive to non-ideal fabrication outcomes that cannot be perfectly eliminated, such as dimensional variation and non-uniform residual stress. This problem can be solved by using a differential drive, introduced in the previous chapter, with feedback control, or limiting actuation to individual frequencies where a combination of different modes produces a desired motion, such as pure vertical motion presented in Chapter 3.3.2. Resonant mode operation in one or more axes is often advantageous because large displacement can be obtained at even lower voltage, but the coupling of different vibration modes and shift of natural frequencies as static deflections and operating conditions change need to be characterized and understood.

The shift of the resonant frequencies of MEMS devices is not uncommon, and it has been a topic of interest for the researchers in the MEMS community. For example, the variation of the natural frequency of electrostatic actuators due to a peak-to-peak and dc bias voltage has been reported with a model that includes of nonlinear electrostatic force to explain the behaviors [4.16, 4.17]. Actuators that use the electrostatic force generated by asymmetric comb-drive designs and thus can tune their resonance by a dc bias have been developed [4.18, 4.19]. Detailed beam models were also presented to describe nonlinearities related to the stiffening and softening of the springs of electrostatic resonators [4.20-4.22]. Using beam models, Soma et al. proposed a method to measure residual stress on electrostatically actuated microbeams using frequency shift curves experimentally obtained at different dc bias voltages [4.23]. Among piezoelectric MEMS devices, vibration energy harvesters that can tune the resonance frequency by a preload [4.24] or nonlinear strain stiffening effect [4.25] have been developed.

An electrothermal actuator that has a similar design to the device of this work also showed a trend of decreasing resonant frequency with the increase of a bias voltage [1.33], and the authors stated that the shift was due to the temperature dependent property of Young's modulus and the stiffness change of the bimorphs, although no model was provided for the shift. A more pronounced decrease of the resonant frequencies as the offset voltage increases has been observed from the thin-film PZT micro-scanner of this work. The findings of the aforementioned studies on similar behaviors, such as frequency-dependent material properties and stiffened beams, could have caused the phenomena, but the shift observed here is too large to be solely explained by them, as some cases the natural frequency decreased more than 30%.

Instead of associating nonlinearities only with a single element such as a beam as in some of the previous work, a nonlinear change of the structural compliance during the motion of an actuator can be considered. For example, [4.26] investigated the variation of the rotation-mode resonant frequency of a two-axes piezoelectric actuator that can perform an active vertical (z-axis direction) and passive rotational (about y-axis) scan simultaneously with its inner and outer frames connected by a set of short cantilevers. In that paper, the coupling of the resonance of the inner frame with the lateral compliance of the outer frame as a function of the outer frame's vertical motion was modeled. Similar to many other works mentioned above, that model also assumed perfect symmetric spring structures and neglected the residual stress.

Relating nonlinearities to structural behavior at large displacements, this section analyzes how the stiffness of a large stroke scanner changes in multiple directions as its position changes and then examines the effects of the stiffness change on the resonant frequencies. Building on the model in the previous chapter that analyzed static behavior, individual beams within the legs of the micro-scanner are modeled in multiple axes to capture dynamics and coupled motion in different directions. Additionally, the effect of residual stress on resonant frequencies is studied.

4. 2. 2. Modeling of Multi-Axis Motion of Stage

The piezoelectric multi-axis stage of this work can be designed to emphasize pure vertical translation, or to produce multi-axis motion through differential actuation of legs or resonance selection or both. As can be visualized from Figure 2.2, the stiffness of the stage changes as the stage moves in the z-axis direction. In particular, the stiffness in the x-axis direction changes the most as an x-axis direction force on the stage will generate a torsional loading on the beams if the stage is at non-0V-position. The further the stage is away from its 0V-position, the larger the torsional loading the beams experience. A structural model that include this torsional loading has been developed. Using the expression for the deflection of a single beam developed in section 2.2.2.1 (Eq. 2.7), this section describes the development of the model that starts from the deflection analysis of a single leg.

4. 2. 2. 1. Vertical and Angular Displacements of Single Leg

Figure 4.15 shows the reaction forces and moments between a single leg of the scanner and the stage. The horizontal force, F_x , exists due to residual stress and is included because it generates an additional torsional loading on the beams and thus effectively changes their torsional stiffness. Three-dimensional analysis of the deflections of multiple beams connected in series quickly becomes considerably complicated. Thus, the following assumptions were made with the intention to develop a model that is not too complex to analyze but has important coupling terms, reasonably approximated, to adequately capture the stiffness change that occur during the motion.

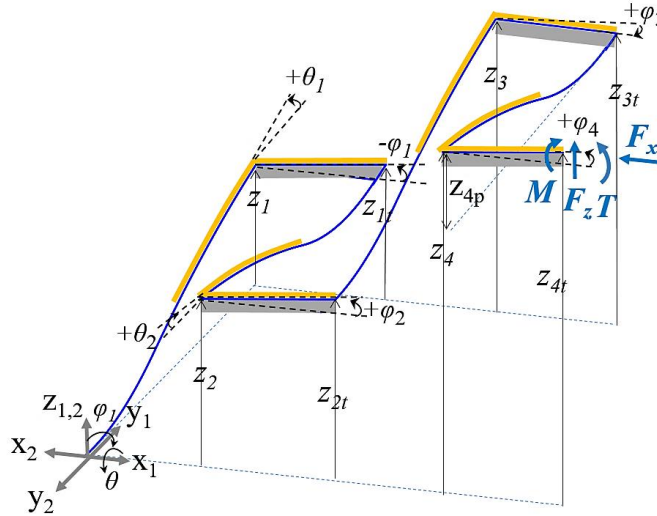


Figure 4.15. Definitions of the angles and displacements of a leg, and effective external forces and moments applied to its tip (not drawn to scale).

Assumption 1: Beams can be twisted by a torsion, but the effect of the twist on the vertical deflection of within that beam is neglected.

Assumption 2: The short beams, also referred to as connectors in Figure 4.14, that connect two longer beams, are too rigid to be bent or twisted, but they can rotate as beams are twisted (i.e. they are assumed to be rigidly connected to the beams).

Assumption 3: In calculating the torsion applied to each beam by the horizontal force, F_x , the rotation of each connector is assumed to be small. (e.g. $F_x \cdot z_{4p} \cdot \cos(\varphi_3) \approx F_x \cdot z_{4p}$ and $L_t \cdot F_x \cdot \sin(\varphi_4) \approx 0$, where z_{4p} is the vertical deflection of beam 4)

Assumption 4: In calculating the torsion applied to each beam by the vertical force, F_z , the rotation of each connector is assumed to be small. (e.g. $L_t \cdot F_z \cdot \cos(\varphi_4) \approx L_t \cdot F_z$)

Assumption 5: When beams are actuated, they bend such that the angle of each end is small, and thus the vertical force, F_z , is assumed to be applied to each end of the beam in the perpendicular direction to its base angle. (e.g. in calculating z_{4p} , the force that cause beam 4 deflect, $F_z \cdot \cos\vartheta_3$ is approximated by F_z)

In the following analysis, the translational and angular displacements of the beams are expressed using local coordinates. The deflections of beams 1 and 3 are expressed in the x_1 - y_1 - z_1 coordinates, and those of beams 2 and 4 in the x_2 - y_2 - z_2 coordinates shown in Figure 4.15. They are chosen such that the vertical displacement and slope of each beam are both positive as it moves upward. The end of a beam without the top gold layer is referred to as the base of a beam and the other end as the tip.

Using the assumptions and definitions above, the forces and moments at the tip of each beam due to the external forcing at the end of leg j , $F_{x,j}$, $F_{z,j}$, M_j , and T_j ($j=A, B, C, D$), can be approximated as follows for the deflection calculation of the individual beams:

$$\text{Moment at the tip of beam } i \text{ of leg } j \approx (-1)^i M_j - \frac{1+(-1)^{i+1}}{2} F_{z,j} L \quad (\text{Eq. 4.6})$$

$$\text{Force at the tip of beam } i \text{ of leg } j \approx F_{z,j} \quad (\text{Eq. 4.7})$$

$$\text{Torsion along beam } i \text{ of leg } j \approx (-1)^i \left\{ T_j + (5-i)(-1)^j F_{z,j} L_t + F_{x,j} \sum_1^{5-i} z_{ip,j} - F_{x,j} z_{ip,j}(y) \right\} \quad (\text{Eq. 4.8})$$

where $i = 1, 2, 3, 4$,

$$j = \begin{cases} 1 & \text{for leg B and C} \\ 2 & \text{for leg A and D} \end{cases}, \text{ and } z_{ip,j} \text{ is the vertical deflection of single beam } i \text{ of leg } j.$$

As the last term in Eq. (4.8) indicates, the magnitude of the torsion changes along the beam length because it is a function of the vertical displacement of the beams, so this equation can be integrated to find an expression for the torsional displacement, φ , of a beam of leg j under the external forces and moments, $F_{x,j}$, $F_{z,j}$, M_j , and T_j . Because of Assumption 1, the torsional displacement is not coupled with vertical displacement of a beam, and thus one can find the vertical displacement, z , and slope, θ , of a beam under the loading conditions expressed in equations (4.6) and (4.7) by simply using the mapping function between the force/moment and displacements obtained in section 2.2.2.1 (Eq. 2.7)

Then, deflections of individual beams can be added together to express the vertical and angular displacements, z_j , θ_j , and φ_j , of leg j as a function of the external forcing, $F_{x,j}$, $F_{z,j}$, M_j , T_j , applied

voltage, V_j , and effective residual moment on all the segments.

$$\varphi_j = f_{1,j}(F_{x,j}, T_j, M_j, F_{z,j}, V_j, M_{res,j}) \quad (\text{Eq. 4.9})$$

$$\theta_j = f_{2,j}(F_{x,j}, T_j, M_j, F_{z,j}, V_j, M_{res,j}) \quad (\text{Eq. 4.10})$$

$$z_j = f_{3,j}(F_{x,j}, T_j, M_j, F_{z,j}, V_j, M_{res,j}) \quad (\text{Eq. 4.11})$$

where $j=A, B, C, D$, and $M_{res,j}$'s is the effective residual stress applied on each segment of the leg j (i.e. $M_{res,up,1,j}$, $M_{res,dn,1,j}$, $M_{res,up,2,j}$, $M_{res,dn,2,j}$, $M_{res,up,3,j}$, $M_{res,dn,3,j}$, $M_{res,up,4,j}$, $M_{res,dn,4,j}$, where the subscripts k, i, j refer to segment, beam, and leg in the notation $M_{res,k,i,j}$, respectively). In this analysis, these angular and vertical displacements are expressed in the local coordinates of each leg's beam 4. Due to the coupling between bending and twisting, functions f_1, f_2, f_3 that map the external forcing, applied voltage, and effective residual moments on all the segments to a displacement in each direction are nonlinear.

4. 2. 2. 2. Horizontal Displacement of Single Leg

To obtain an expression for the tip displacement of leg j in the x-axis direction under the same loading conditions, it is key to capture the stiffness change in the x-axis direction as the legs deflect. Because of their low aspect-ratio cross-section, the bending stiffness of beams in the x-axis direction is much higher than other directions, so the deflection of the beams in the x direction by the horizontal force, F_x , is small and neglected. What is more significant is the motion of the tip of each beam due to its twist. One way to find the tip displacement of a leg in the x-axis direction using the obtained vertical and angular displacements of the beams is to define a vector from the base of beam 1 to the tip of beam 4, which can be expressed as follows:

$$\vec{r}_{4t/0}|_1 = \vec{r}_{4t/4}|_1 + \vec{r}_{4/3t}|_1 + \vec{r}_{3t/3}|_1 + \vec{r}_{3/2t}|_1 + \vec{r}_{2t/2}|_1 + \vec{r}_{2/1t}|_1 + \vec{r}_{1t/1}|_1 + \vec{r}_{1/0}|_1 \quad (\text{Eq. 4.12})$$

where $\vec{r}_{1/0}|_1$ is the physical vector representing the position of the tip of beam 1 relative to its base (the origin in Figure 4.15) with respect to Frame 1, the x_1 - y_1 - z_1 coordinate. Subscripts 1, 2, 3, 4 before and after the symbol '/' in Eq. 4.12 refer to the position of the tip of beam 1, 2, 3, 4,

while subscripts $1_t, 2_t, 3_t, 4_t$ refer to the position of the tip of connector 1, 2, 3, 4. Each vector in Eq. 4.12 can be rewritten using directional cosine matrices and body-fixed frames. For example,

$$\begin{aligned}\vec{r}_{4_t/4}|_1 &= O_{1/1_t} O_{1_t/2} O_{2/2_t} O_{2_t/3} O_{3/3_t} O_{3_t/4} O_{4/4_t} \vec{r}_{4_t/4}|_{4_t} \\ \vec{r}_{4/3_t}|_1 &= O_{1/1_t} O_{1_t/2} O_{2/2_t} O_{2_t/3} O_{3/3_t} O_{3_t/4} \vec{r}_{4/3_t}|_4\end{aligned}\quad (\text{Eq. 4.13})$$

where, for $i=1, 2, 3, 4$,

$$O_{i/i_t} = (O_2(\varphi_i) O_1(\theta_i))^T, \quad O_{i_t/(i+1)} = O_3(\pi)^T, \quad O_1(\theta_i) \triangleq \begin{bmatrix} 1 & 0 & 0 \\ 0 & \cos(\theta_i) & \sin(\theta_i) \\ 0 & -\sin(\theta_i) & \cos(\theta_i) \end{bmatrix},$$

$$O_2(\varphi_i) \triangleq \begin{bmatrix} \cos(\varphi_i) & 0 & -\sin(\varphi_i) \\ 0 & 1 & 0 \\ \sin(\varphi_i) & 0 & \cos(\varphi_i) \end{bmatrix}, \quad O_3(\pi) \triangleq \begin{bmatrix} -1 & 0 & 0 \\ 0 & -1 & 0 \\ 0 & 0 & 1 \end{bmatrix},$$

$$\vec{r}_{i/(i-1)_t}|_i = \begin{bmatrix} \cos(\varphi_i) & 0 & \sin(\varphi_i) \\ 0 & 1 & 0 \\ -\sin(\varphi_i) & 0 & \cos(\varphi_i) \end{bmatrix} \begin{bmatrix} 0 \\ L \\ z_{ip} \end{bmatrix}, \quad \vec{r}_{i_t/i}|_{i_t} = \begin{bmatrix} (-1)^{i+1} L_t \\ 0 \\ 0 \end{bmatrix}, \text{ and Frame } i \text{ is fixed on the}$$

base of beam i , while Frame i_t on the tip of beam i . L and L_t is the length of the beam and connector, respectively. z_{ip} is the vertical deflection of beam i alone, different from z_i , which is the vertical position of the tip of beam i measured from the base of beam 1. As an approximation, the length of connector is ignored and small angle assumptions are used in the analysis. Rewriting each term in Eq. (4.12) using Eq. (4.13), the x-component of $\vec{r}_{4_t/0}|_1$ is the displacement of the tip of the leg in the x-axis direction expressed in terms of vertical and angular displacements of all beams of leg j , $\varphi_{i,j}$, $\theta_{i,j}$, and $z_{i,j}$, with respect to the x_1 - y_1 - z_1 coordinates, and its sign can be reversed to express it in the x_2 - y_2 - z_2 coordinates, the local coordinates used for the deflection calculation of beam 4, or leg j .

Then, using equations (4.9)-(4.11), the horizontal displacement of the tip of leg j can also be written as a function of the external forcing terms, applied voltage, and effective residual moments on all the segments within leg j as follows, using the same notation as before:

$$x_j = f_{4,j}(F_{x,j}, T_j, M_j, F_{z,j}, V_j, M_{res,j}) \quad (\text{Eq. 4.14})$$

4. 2. 2. 3. Stage Motion

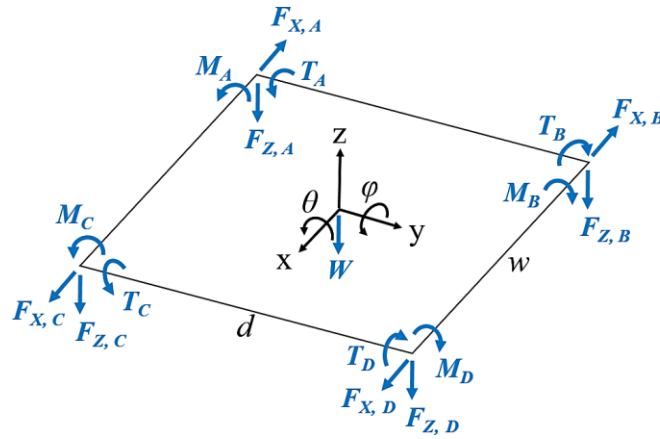


Figure 4.16. Free body diagram of the stage with definitions of reaction forces and moments (not drawn to scale)

Now the coupling between legs can be included through the equations describing the motion of the stage. Based on the free body diagram of the stage (Figure 4.16), the dynamic equation in the standard 2nd order mass-spring-damper form, assuming decoupled damping, is

$$m\ddot{x} = F_{x,A} - F_{x,B} + F_{x,C} - F_{x,D} - b_x\dot{x} \quad (\text{Eq. 4.15})$$

$$J_\varphi\ddot{\varphi} = T_A - T_B + T_C - T_D + (-F_{z,A} - F_{z,B} + F_{z,C} + F_{z,D})\frac{w}{2} + (F_{x,A} - F_{x,B} - F_{x,C} + F_{x,D})\frac{w}{2}\varphi - b_\varphi\dot{\varphi} \quad (\text{Eq. 4.16})$$

$$J_\theta\ddot{\theta} = M_A - M_B + M_C - M_D + (F_{z,A} - F_{z,B} + F_{z,C} - F_{z,D})\frac{d}{2} - b_\theta\dot{\theta} \quad (\text{Eq. 4.17})$$

$$m\ddot{z} = -F_{z,A} - F_{z,B} - F_{z,C} - F_{z,D} - mg - b_z\dot{z} \quad (\text{Eq. 4.18})$$

where m , J_φ , and J_θ are the mass and rotational inertias in the θ and φ direction of the stage, respectively, and g is the gravitational acceleration. The stage can be initially tilted due to residual stress on the legs. If so, the horizontal forces, $F_{x,j}$, also exerts moments on the stage.

Since the stage and legs are physically connected, the following geometric constraints exist:

$$\begin{bmatrix} x_j \\ \varphi_j \\ \theta_j \\ z_j \end{bmatrix} = \begin{bmatrix} (-1)^n & 0 & 0 & 0 \\ 0 & (-1)^n & 0 & 0 \\ 0 & 0 & (-1)^n & 0 \\ 1 & (-1)^m \frac{w}{2} & (-1)^n \frac{d}{2} & 1 \end{bmatrix} \begin{bmatrix} x \\ \varphi \\ \theta \\ z \end{bmatrix}$$

$$\triangleq \bar{X}_j = T_j \bar{X} \quad (j=A, B, C, D) \quad (\text{Eq. 4.19})$$

where $n=1$ for $j=A, C$, and $n=2$ for $j=B, D$,
 $m=1$ for $j=C, D$, and $m=2$ for $j=A, B$.

Nonlinear equations (4.15)-(4.18) along with (4.9)-(4.11), (4.14), and (4.19) describe the motion of the stage. One way to find the resonance of the stage at a given AC voltage input is to find its static position at a given dc bias voltage using the above nonlinear equations, and then consider a linear behavior about the equilibrium position. In other words, if the effective residual moments and input voltage on each leg are prescribed, one can numerically find static displacements of the stage, $\bar{X}_e = [x_e \ \theta_e \ \varphi_e \ z_e]^T$, and reaction forces and moments between the legs and stage, $\bar{F}_{j,e} = [F_{x,j,e} \ T_{j,e} \ M_{j,e} \ F_{z,j,e}]^T$, using equations (4.9-4.11, 4.14-4.19), which then can be linearized to construct a linear dynamic model.

One way to solve for the static displacements and reaction forces and moments at a given applied voltage and residual stress is to initially guess them and iterate to find a numerical solution where the geometric constraints between the center of the stage and each leg (Eq. 4.19) as well as static conditions (*i.e.* $\sum_{j=A,B,C,D} \bar{F}_j = 0$) are satisfied. The applied voltage and residual stress can be gradually increase from zero to find a numerical solution, or the solution of a linear model that assumes no coupling in the x-axis (*i.e.* the model of Chapter 4.1 with $x_j = f_{4,j}(F_{x,j})$ where $j=A, B, C, D$) can be used as an initial guess.

The eigenvalues of the linear model can be used to obtain the nominal resonant frequencies of the scanner at a given offset voltage. Linearizing the leg equations (4.9)-(4.11) and (4.14) about the equilibrium states found using the nonlinear equations above, they become:

$$\begin{bmatrix} \Delta x_j \\ \Delta \varphi_j \\ \Delta \theta_j \\ \Delta z_j \end{bmatrix} = \begin{bmatrix} \frac{\partial f_{4,j}}{\partial F_{x,j}} & \frac{\partial f_{4,j}}{\partial T_j} & \frac{\partial f_{4,j}}{\partial M_j} & \frac{\partial f_{4,j}}{\partial F_{z,j}} \\ \frac{\partial f_{1,j}}{\partial F_{x,j}} & \frac{\partial f_{1,j}}{\partial T_j} & \frac{\partial f_{1,j}}{\partial M_j} & \frac{\partial f_{1,j}}{\partial F_{z,j}} \\ \frac{\partial f_{2,j}}{\partial F_{x,j}} & \frac{\partial f_{2,j}}{\partial T_j} & \frac{\partial f_{2,j}}{\partial M_j} & \frac{\partial f_{2,j}}{\partial F_{z,j}} \\ \frac{\partial f_{3,j}}{\partial F_{x,j}} & \frac{\partial f_{3,j}}{\partial T_j} & \frac{\partial f_{3,j}}{\partial M_j} & \frac{\partial f_{3,j}}{\partial F_{z,j}} \end{bmatrix} \begin{bmatrix} \Delta F_{x,j} \\ \Delta T_j \\ \Delta M_j \\ \Delta F_{z,j} \end{bmatrix} + \begin{bmatrix} \frac{\partial f_{4,j}}{\partial V_j} \\ \frac{\partial f_{1,j}}{\partial V_j} \\ \frac{\partial f_{2,j}}{\partial V_j} \\ \frac{\partial f_{3,j}}{\partial V_j} \end{bmatrix} \Delta V_j$$

$$\triangleq \Delta \bar{X}_j = S_{ext,j} \Delta \bar{F}_j + S_{int,j} \Delta V_j \quad (j=A, B, C, D) \quad (\text{Eq. 4.20})$$

The linearized stage equations (4.15)-(4.18) is

$$M \Delta \ddot{\bar{X}} + B \Delta \dot{\bar{X}} = K_e \Delta \bar{X} - Q_A \Delta \bar{F}_A - Q_B \Delta \bar{F}_B - Q_C \Delta \bar{F}_C - Q_D \Delta \bar{F}_D \quad (\text{Eq.4.21})$$

where

$$M = \begin{bmatrix} m & 0 & 0 & 0 \\ 0 & J_\varphi & 0 & 0 \\ 0 & 0 & J_\theta & 0 \\ 0 & 0 & 0 & m \end{bmatrix}, B = \begin{bmatrix} b_x & 0 & 0 & 0 \\ 0 & b_\varphi & 0 & 0 \\ 0 & 0 & b_\theta & 0 \\ 0 & 0 & 0 & b_z \end{bmatrix},$$

$$K_e = \frac{w}{2} (F_{x,A,e} - F_{x,B,e} - F_{x,C,e} + F_{x,D,e}) \begin{bmatrix} 0 & 0 & 0 & 0 \\ 0 & 1 & 0 & 0 \\ 0 & 0 & 0 & 0 \\ 0 & 0 & 0 & 0 \end{bmatrix}, \text{ and}$$

$$Q_j = \begin{bmatrix} (-1)^n & 0 & 0 & 0 \\ (-1)^q \frac{w}{2} \varphi_e & (-1)^n & 0 & (-1)^m \frac{w}{2} \\ 0 & 0 & (-1)^n & (-1)^n \frac{d}{2} \\ 0 & 0 & 0 & 1 \end{bmatrix}$$

where $F_{x,j,e}$ is horizontal reaction force between the stage and leg j at equilibrium ($j=A, B, C, D$),

$n=1$ for $j=A, C$, and $n=2$ for $j=B, D$,

$m=1$ for $j=C, D$, and $m=2$ for $j=A, B$,

$q=1$ for $j=A, D$, and $q=2$ for $j=B, C$,

φ_e =stage tilt angle in the φ direction at equilibrium. The additional stiffness term, K_e , exists because the horizontal forces $F_{x,j,e}$, apply moments on the tilt stage.

Geometrical constraint Eq. 4.19 becomes

$$\Delta\bar{X}_j = T_j \Delta\bar{X} \quad (j=A, B, C, D) \quad (\text{Eq. 4.22})$$

Now that all the equations are linear, rewriting Eq. 4.21 using equations (4.20) and (4.22) and assuming a single input (i.e. same voltage on all legs) gives

$$M\Delta\ddot{\bar{X}} + B\Delta\dot{\bar{X}} + K\Delta\bar{X} = G_{voltage}\Delta V \quad (\text{Eq. 4.23})$$

where

$$K = K_e + \sum_{j=A,B,C,D} Q_j S_{ext,j}^{-1}$$

$$G_{voltage} = \sum_{j=A,B,C,D} Q_j S_{ext,j}^{-1} S_{int,j}$$

Equation (21) can also be written in the state-space form:

$$\begin{bmatrix} \Delta\dot{\bar{X}} \\ \Delta\ddot{\bar{X}} \end{bmatrix} = \begin{bmatrix} 0 & I \\ -M^{-1}K & -M^{-1}B \end{bmatrix} \begin{bmatrix} \Delta\bar{X} \\ \Delta\dot{\bar{X}} \end{bmatrix} + \begin{bmatrix} 0 \\ M^{-1}G_{voltage} \end{bmatrix} \Delta V$$

$$\triangleq A_{sys} \begin{bmatrix} \Delta\bar{X} \\ \Delta\dot{\bar{X}} \end{bmatrix} + B_{sys}\Delta V \quad (\text{Eq. 4.24})$$

Equations (4.23) & (4.24) describe the dynamic motion of the stage about an equilibrium position at a bias voltage. Different bias voltages result in different equilibrium positions, producing different values of K and $G_{voltage}$ in Eq. 4.23 and different values of A_{sys} and B_{sys} in Eq. 4.24. Computing the eigenvalues of A_{sys} gives the damped natural frequencies of the scanner, and the pairing of an eigenvalue with the right mode or state can be done by exciting one state at a time and analyzing bode plots.

4. 2. 3. Simulation Studies

With the model developed in the previous section, the effects of dc bias voltage on the system's resonant frequencies can be studied. First, an ideal case with the absence of residual stress, thus perfect symmetry, is simulated and plotted in Figure 4.17. For the simulation purpose, the damping constants that gives 3% damping ratio, observed experimentally, for the ideal case was found and used for the results in this section. The values of $d_{31,eff}$ was extracted from the experimental results that will be presented in the next section. If a system is linear and its structural stiffness does not change as a function offset voltage, all the damped natural frequencies should be constant, showing straight lines in Figure 4.17. As expected, the model shows a drastic change of the natural frequency in the x-axis direction as the bias voltage increases, reflected by the change of the horizontal stiffness as the stage moves vertically. In this ideal case, the simulation shows that the natural frequencies of other direction do not change much.

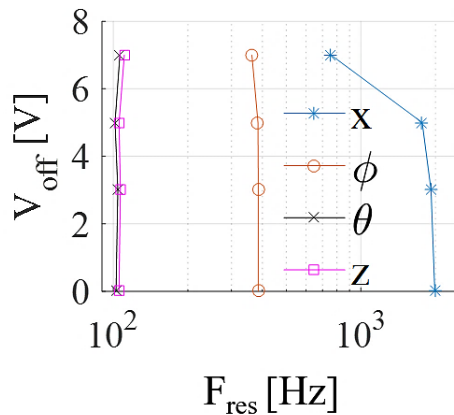


Figure 4.17. Simulated shift of resonant frequencies (F_{res}) as V_{off} changes in the ideal case (no residual stress & perfect symmetry)

In fabricated stages, the legs are bent initially due to residual stress, and the stage is tilt due to non-uniform residual stress across the device. To simulate the impacts of non-identical initial deflection of the legs, residual stress was applied to each leg. For the initial non-zero vertical displacement of the stage, the same amount of residual stress is applied to all the legs, and for

the initial tilt of the stage additional, different amount of residual stress is applied to the legs.

Figures 4.18 and 4.19 show the simulation results when nominal residual stress producing an initial stage deflection of $160\mu\text{m}$ is applied to all the legs with additional residual stress on legs B and D for initial stage tilting in the θ direction and on legs A and B in the ϕ direction, respectively. In both cases, the frequencies associated with the x-direction and ϕ direction decrease as the OV height of the stage increases, although the change in the x-direction is not as much as the ideal case because the stage is away from the zero-height position due to residual stress. Both scenarios show that the frequencies associated with the z direction and ϑ direction do not change much, although their trends are opposite.

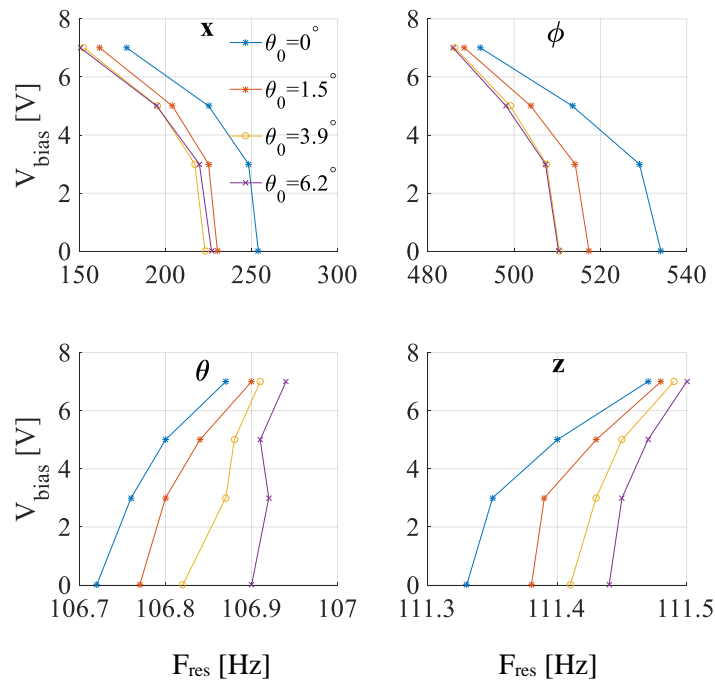


Figure 4.18. Simulated resonant frequency (F_{res}) shift as non-uniform residual stress increases initial stage tilt in ϑ direction ($z_0=160\ \mu\text{m}$)

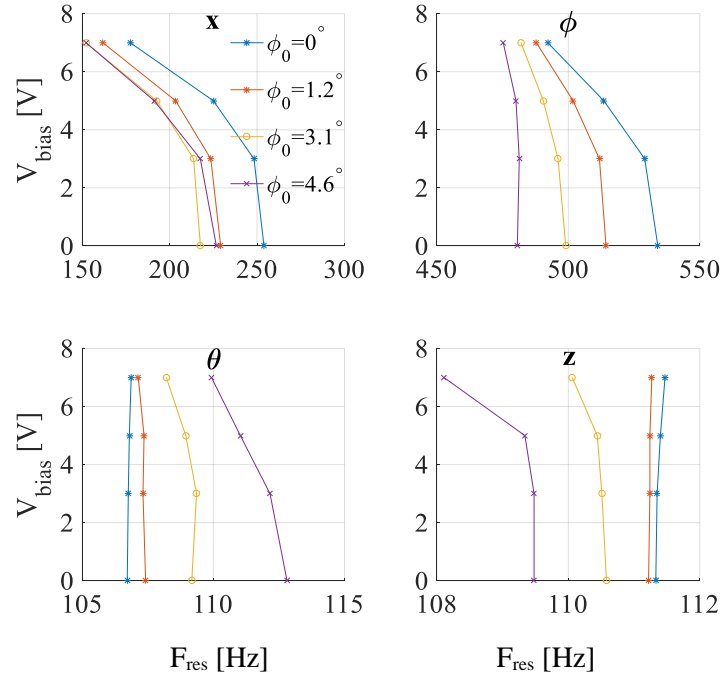


Figure 4.19. Simulated resonant frequency (F_{res}) shift as non-uniform residual stress increases initial stage tilt in ϕ direction ($z_0=160 \mu\text{m}$)

Additional simulation results where initial stage height is varied ($z_0=82, 160, 236\mu\text{m}$) and also separately where tilting angles in both directions are varied simultaneously ($\theta_0=0^\circ$ & $\phi_0=0^\circ$, $\theta_0=0.7^\circ$ & $\phi_0=0.8^\circ$, $\theta_0=1.5^\circ$ & $\phi_0=1.9^\circ$, $\theta_0=2.3^\circ$ & $\phi_0=3.0^\circ$) imply that the natural frequencies in the x- and ϕ -mode clearly decrease as the bias voltage increases (i.e. the stage height increase) regardless of the uniformity or the magnitude of residual stress on the device. The results also suggest that the bias voltage has less effect on the z- and θ -mode but their trends depend on the variation of residual stress across the device (i.e. the initial tilting of the stage due to residual stress).

4. 2. 4. Comparison with Experimental Results

So far, the effects of a dc bias voltage on the resonant frequency of each mode have been studied using the model developed in section 4.2.2. Experimental measurements, however, usually record some combination of different vibration modes. For example, if vertical displacement of each corner of the stage is measured experimentally, the measurements have the following

relationship with the states (x, ϕ, θ, z) of the stage:

$$z_j = z + (-1)^n \frac{d}{2} \theta + \left(\frac{w}{2} + (-1)^m x \right) (-1)^m \phi \quad (\text{Eq. 4.25})$$

where $j=A, B, C, D$, $n=1$ for $j= A, C$, $n=2$ for $j=B, D$, $m=1$ for $j=C, D$, and $m=2$ for $j=A, B$.

The linearization of Eq. (4.25) imparts:

$$\Delta z_j = \Delta z + (-1)^n \frac{d}{2} \Delta \theta + (x_e + (-1)^m \frac{w}{2}) \Delta \phi + \phi_e \Delta x \quad (\text{Eq. 4.26})$$

where ϕ_e and x_e are the equilibrium position of the stage at a bias voltage and other notations are the same as Eq. (4.25).

Using equations (4.24) and (4.26), one can run a simulation to predict the experimental observation shown in Figure 4.20. Comparative experimental results are taken from the vertical displacements of the four corners of a sample stage measured using Keyence's LK-G32 laser displacement sensor while a $6V_{pp}$ sinusoidal input signal was swept over 0 to 800 Hz with a step of 5 Hz at different dc bias voltages ($3V_{off}$, $5V_{off}$, $7V_{off}$). The measurements were taken after poling the PZT at 10V for 5mins.

The simulation results are plotted in Figure 4.21. The static position of the stage at 0V is used to estimate the residual stress on each leg, and the deflection of each leg at low frequency was used to estimate the value of effective electro-active piezoelectric strain coefficient, $d_{31,eff}$. The different magnitudes of the amplitude on the legs at each bias voltage are captured by adjusting the $d_{31,eff}$ values for the individual legs. After the values of $d_{31,eff}$ and effective residual moments are found, the damping coefficients are manually tuned to find the best match with the experimental results.

First of all, the decreasing trend of the natural frequencies in relation to the increasing bias voltage has been well captured by the model. Although there are discrepancies in the shape and magnitude of the 2nd peak around 200 Hz, the model shows good estimates of resonant frequencies compared to the experimental data.

A likely contribution to remaining discrepancies between model and experiment is that instead of measuring the initial deflections of individual legs to find the effective residual moment on all the beams, the initial tilting angles and vertical displacement of the stage was used to find equivalent residual moments on each leg that produce the initial position of the stage. Also, the magnitude of the piezoelectric strain coefficient and residual stress is observed to be different from leg to leg and beam to beam, but for simplicity they are lumped into one value for each leg (i.e. all the beams within a leg are simulated with the same values). When taken into account, these will change the magnitude of coupling terms and thus stage height, affecting the resonant frequencies and the peak magnitudes. Unmodeled hysteresis of PZT produces imperfect sine waves, and this means that the scanner is excited at multiple frequencies simultaneously. This could change the peak magnitudes as well.

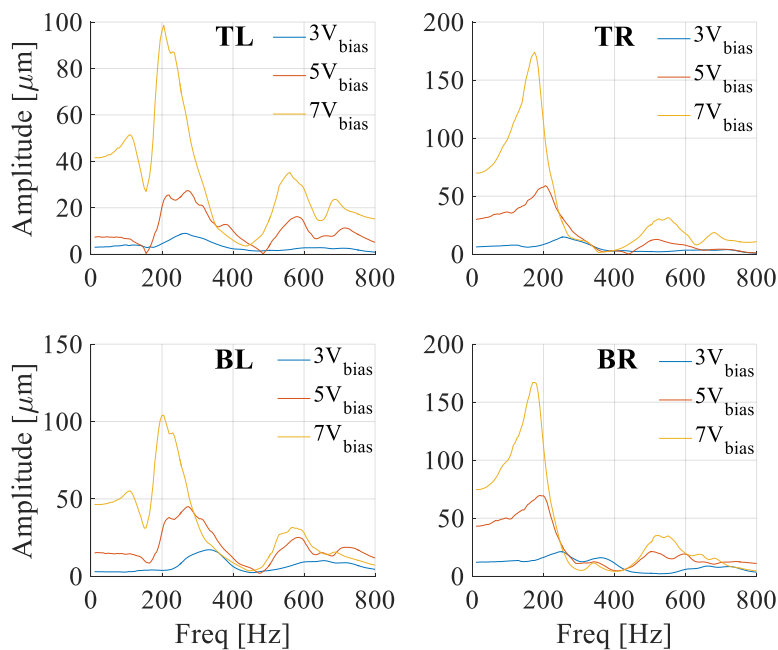


Figure 4.20. Experimental frequency response with constant $6V_{pp}$ and varying dc voltages, showing the measurements taken at the top left (TL), top right (TR), bottom left (BL), and bottom right (BR) corner of the stage

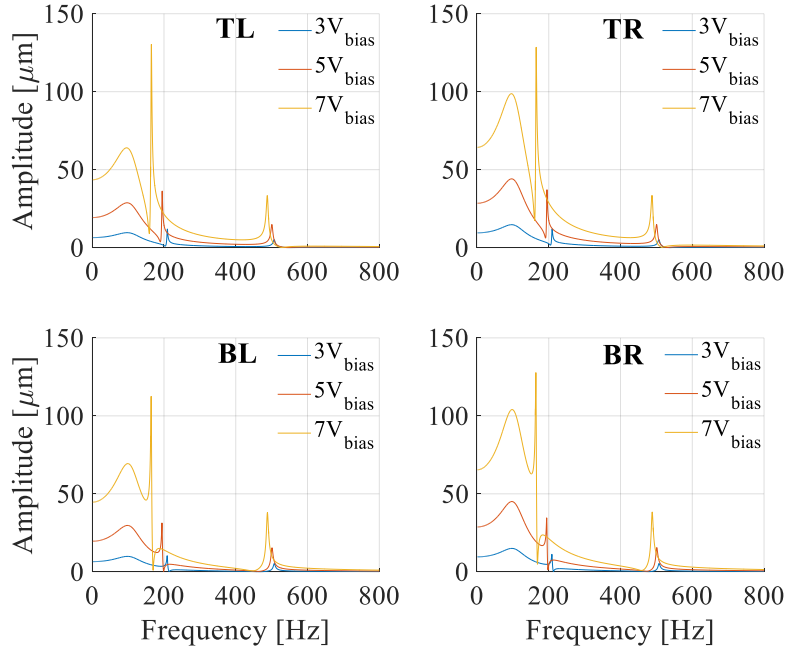


Figure 4.21. Model prediction of the experimental results with constant $6V_{pp}$ and varying dc voltages, showing the measurements taken at the top left (TL), top right (TR), bottom left (BL), and bottom right (BR) corner of the stage

4. 2. 5. Summary

The nonlinear dynamic behavior of the thin-film PZT scanner of this work has been studied. As presented in Section 2.4, this scanner had demonstrated more than $400\ \mu\text{m}$ of out-of-plane displacement under $15V_{DC}$ despite its small footprint (3.2mm by 3.2mm). An AC sinusoidal excitation can be used to make the input voltage even lower and to avoid producing unwanted motion that can be generated from a single DC voltage input due to residual stress-induced deflections (Section 3.3.2), which is important for successful image registration. In order to take advantages of these benefits of the AC operation, the shift of resonant frequencies of the scanner due to a dc bias voltage needs to be understood. Thus, a model has been developed that accounts for the stiffness change in multiple directions during the motion of the stage and thus the coupling between the position of the stage and its resonant frequencies. The model incorporates the effects of residual stress and its varying magnitude across the whole scanner structure.

The simulation studies have shown a noticeable decrease in the natural frequencies in x - and ϕ -directions as the stage moves up, regardless of the initial 0V position of the stage. In comparison, the natural frequencies in z - and θ -directions change more inconsiderably, but their trends change depending on the initial 0V position of the stage (i.e. more depend on the residual stress). Using the residual stress and piezoelectric coefficients extracted from the experimental measurements, the model adequately predicts the experimentally observed natural frequencies of the stage at each dc bias voltage.

Non-uniform residual stress and dimensional variations developed from the fabrication processes cause asymmetries in MEMS structures, which generate unintended internal stresses. For a device designed to generate a large motion, these stresses can significantly change its dynamic characteristics. The model presented in this work effectively describes the nonlinear dynamic behavior of a piezoelectric scanner by accounting for the effects of unintended internal stresses on the structural compliance. Measured residual stress on each beam and the addition of the characterized frequency-dependent piezoelectric properties and its hysteresis behavior can improve the model.

This model can be used to drive the piezoelectric scanner in a Lissajous scanning pattern in prototype endo-microscopic imaging systems for vertical cross-sectional imaging of tissue. For a robust control of the stage motion or the scanning pattern, embedded sensing elements can be characterized and used with a feedback control scheme.

4. 3. References

- [4.1] Yazdi, N., et al. Robust sliding-mode control of electrostatic torsional micromirrors beyond the pull-in limit. TRANSDUCERS, Solid-State Sensors, Actuators and Microsystems, 12th International Conference on, 2003. Vol. 2. IEEE, 2003.

- [4.2] De Volder M, Coosemans J, Puers R and Reynaerts D 2008 Characterization and control of a pneumatic microactuator with an integrated inductive position sensor, *Sensors and Actuators A: Physical* 141 192-200.
- [4.3] Choi S B, Kim H K, Lim S C and Kim J H 2000 Position tracking control of an optical pick-up device using piezoceramic actuator. In: *Smart Structures and Materials 2000 Conference*, (Newport Beach, CA, USA) pp 370-6.
- [4.4] Izhar U, Izhar A B and Tatic-Lucic S 2011 A multi-axis electrothermal micromirror for a miniaturized OCT system *Sensors and Actuators A: Physical* 167 152-61.
- [4.5] Tung Y C and Kurabayashi K 2005 A single-layer PDMS-on-silicon hybrid microactuator with multi-axis out-of-plane motion capabilities - Part I: Design and analysis *Journal of Microelectromechanical Systems* 14 548-57.
- [4.6] Liu W, Zhu Y, Jia K, Liao W, Tang Y, Wang B and Xie H 2013 A tip-tilt-piston micromirror with a double S-shaped unimorph piezoelectric actuator *Sensors and Actuators A: Physical* 193 121-8.
- [4.7] Damjanovic, D., 2006. Hysteresis in piezoelectric and ferroelectric materials. *The science of hysteresis*, 3, pp.337-465.
- [4.8] Hall, D.A., 2001. Review nonlinearity in piezoelectric ceramics. *Journal of materials science*, 36(19), pp.4575-4601.
- [4.9] Lu, W., Fang, D.N., Li, C.Q. and Hwang, K.C., 1999. Nonlinear electric-mechanical behavior and micromechanics modelling of ferroelectric domain evolution. *Acta Materialia*, 47(10), pp.2913-2926.
- [4.10] Ebert, M., Naumann, F., Gerbach, R. and Bagdahn, J., 2007, April. Measurement of dynamic properties of MEMS and the possibilities of parameter identification by simulation. In *2007 International Conference on Thermal, Mechanical and Multi-Physics Simulation Experiments in Microelectronics and Micro-Systems. EuroSime 2007* (pp. 1-6). IEEE.
- [4.11] Naono T, Fujii T, Esashi M, Tanaka S. A large-scan-angle piezoelectric MEMS optical scanner actuated by a Nb-doped PZT thin film. *Journal of Micromechanics and Microengineering*. 2013 Dec 9;24(1):015010.

- [4.12] Davis WO, Beard M, Jackson R. Trajectory precision of micromachined scanning mirrors for laser beam scanning pico-projector displays. InSPIE MOEMS-MEMS 2012 Feb 9 (pp. 825203-825203). International Society for Optics and Photonics.
- [4.13] Freeman M, Champion M, Madhavan S. Scanned laser pico-projectors: seeing the big picture (with a small device). Optics and Photonics News. 2009 May 1;20(5):28-34.
- [4.14] Baran U, Brown D, Holmstrom S, Balma D, Davis WO, Muralt P, Urey H. Resonant PZT MEMS scanner for high-resolution displays. Journal of microelectromechanical systems. 2012 Dec;21(6):1303-10.
- [4.15] Yalcinkaya AD, Urey H, Brown D, Montague T, Sprague R. Two-axis electromagnetic microscanner for high resolution displays. Journal of Microelectromechanical Systems. 2006 Aug;15(4):786-94.
- [4.16] Hong YK, Syms RR. Dynamic response modeling of MEMS micromirror corner cube reflectors with angular vertical combdrives. Journal of Lightwave Technology. 2007 Feb 1;25(2):472-80.
- [4.17] Zhang WM, Meng G. Nonlinear dynamic analysis of electrostatically actuated resonant MEMS sensors under parametric excitation. IEEE sensors journal. 2007 Mar;7(3):370-80.
- [4.18] Yeh JL, Hui CY, Tien NC. Electrostatic model for an asymmetric combdrive. Journal of Microelectromechanical systems. 2000 Mar;9(1):126-35.
- [4.19] Morgan B, Ghodssi R. Vertically-shaped tunable MEMS resonators. Journal of Microelectromechanical Systems. 2008 Feb;17(1):85-92.
- [4.20] Elshurafa AM, Khirallah K, Tawfik HH, Emira A, Aziz AK, Sedky SM. Nonlinear dynamics of spring softening and hardening in folded-MEMS comb drive resonators. Journal of Microelectromechanical Systems. 2011 Aug;20(4):943-58.
- [4.21] Mestrom RM, Fey RH, Phan KL, Nijmeijer H. Simulations and experiments of hardening and softening resonances in a clamped-clamped beam MEMS resonator. Sensors and Actuators A: Physical. 2010 Aug 31;162(2):225-34.
- [4.22] De SK, Aluru NR. Full-Lagrangian schemes for dynamic analysis of electrostatic MEMS. Journal of Microelectromechanical Systems. 2004 Oct;13(5):737-58.

- [4.23] Soma A, Ballestra A. Residual stress measurement method in MEMS microbeams using frequency shift data. *Journal of Micromechanics and Microengineering*. 2009 Sep 1;19(9):095023.
- [4.24] Leland ES, Wright PK. Resonance tuning of piezoelectric vibration energy scavenging generators using compressive axial preload. *Smart Materials and Structures*. 2006 Sep 8;15(5):1413.
- [4.25] Marzencki M, Defosseux M, Basrou S. MEMS vibration energy harvesting devices with passive resonance frequency adaptation capability. *Journal of Microelectromechanical Systems*. 2009 Dec;18(6):1444-53.
- [4.26] Rhee CH, Qiu Z, Choi J, Wang TD, Oldham KR. Dynamics of Thin-Film Piezoelectric Vertical-Rotational Scanning Actuator. In *ASME 2015 International Design Engineering Technical Conferences and Computers and Information in Engineering Conference 2015 Aug 2* (pp. V004T09A026-V004T09A026). American Society of Mechanical Engineers.

CHAPTER 5: CONCLUSIONS & FUTURE WORK

5. 1. Summary

Motivated by an urgent need for a new scanning mechanism for endoscopic imaging tools, a class of multi-axis thin-film PZT actuators have been developed for vertical cross-sectional imaging in endoscopy. The prototype actuators have demonstrated fast (bandwidth >100-200Hz) large vertical stroke length (>400 μ m) in a small footprint (3mm x 3mm) needed for real-time *in vivo* deep into-tissue imaging for early cancer detection. Compared to other actuation mechanisms, these piezoelectric actuators can additionally offer DC actuation capability, minimal heat dissipation, and low power requirement for *in vivo* imaging applications.

However, actuation elements designed to be symmetric showed non-uniform behavior even within single devices, degrading potential imaging quality. This non-ideal behavior is related to MEMS fabrication limitations, such as dimensional variation and residual stress, that cannot be perfectly eliminated. The influence of non-idealities on the static and dynamic behaviors of the actuators were characterized, and effort has been made to deal with imperfect motions of the actuators for improved imaging.

Static and transient models of the actuator have been developed that can capture the effects of fabrication uncertainties on the actuator behaviors. Also, the influence of large vertical translation on its dynamic behavior due to non-ideal fabrication outcomes was studied. These

models can be used for robust design, open-loop operations with multiple inputs, and feed-back control schemes with future integrated sensors.

As another approach to deal with the limitations of fabrication, a method to isolate a pure vertical motion among multiple close-proximity vibration modes only by using a single input was found and used to obtain real-time vertical sectional images of mouse tissue by a thin-film piezoelectric microactuator. Compared to previous endoscopic instruments that can only perform very slow or shallow into-tissue scanning, the benchtop multi-photon system presented in this work has demonstrated fast and deep vertical scanning for the first time thanks to the vertical thin-film PZT actuator. The benchtop system also showed high resolution (from $7\mu\text{m}$ to $4.7\mu\text{m}$ over the vertical scanning range), and its scanning architecture can be packaged into a compact handheld form factor. Fabrication and assembly processes have been also developed to support integration into small optical imaging instruments.

As it was found difficult to manually mount a mirror chip to the mirror platform, the thickness of the embedded scanning mirror surface can be optimized for the best reflectivity. The main limitation of the current actuators is the need for calibration to compensate for any static tilt due to non-uniform initial deflections of the bending legs. Feedback controllers can be implemented using the presented models to increase robustness against disturbances such as external vibrations.

5. 2. Contributions

The main contributions of this dissertation work are summarized as follows:

1. Demonstrated very large ($>400\mu\text{m}$) out-of-plane displacement under $15V_{\text{DC}}$ with relatively high bandwidth ($100\sim 200\text{Hz}$) in a small footprint of 3.2mm by 3.2mm using thin-film PZT, which can

enable real-time *in vivo* vertical cross-sectional imaging for early cancer detection in endomicroscopy

2. Developed scalable fabrication process steps for high performance piezoelectric MEMS devices
3. Introduced a method to develop an analytical model for MEMS devices subject to fabrication uncertainty such as residual stress and dimensional variation
4. Developed an analytical model that captures nonlinear changes in the dynamic behaviors of multi-axis actuators over large vertical stroke
5. Introduced a method to select an operation frequency to obtain a motion of interest for MEMS devices with multiple vibration modes in close proximity, even in the presence of substantial fabrication non-idealities.
6. Achieved vertical multi-photon cross-sectional imaging of biological tissue using a thin-film piezoelectric microactuator for the first time

The results above and other related work are published in the following peer-reviewed journals and conferences.

Refereed Journal Publications

- **J. Choi**, X. Duan, H. Li, T. Wang, K. Oldham, “**Multi-photon vertical cross-sectional imaging with a thin-film lead-zirconate-titanate z-axis microactuator,**” *Journal of Microelectromechanical System*, 2016, In preparation.
- **J. Choi**, T. Wang, K. Oldham, “**Dynamics and Resonance Shifting in Multi-Axis Thin-film Piezoelectric Microactuators Over Large Vertical Stroke,**” *Journal of Micromechanics and Microengineering*, 2016, In preparation.

- **J. Choi**, M. Shin, R. Rudy, C. Kao, J. Pulskamp, R. Polcawich, K. Oldham, “**Thin-film piezoelectric and high-aspect ratio polymer leg mechanisms for millimeter-scale robotics,**” *International Journal of Intelligent Robotics and Applications*, 2016, Submitted.
- **J. Choi**, Z. Qiu, C.-H. Rhee, T. Wang, K. Oldham, “**A three-degree-of-freedom thin-film PZT-actuated microactuator with large out-of-plane displacement,**” *Journal of Micromechanics and Microengineering*, 2014.
- Z. Qiu, C.-H. Rhee, **J. Choi**, T. Wang, K. Oldham, “**Large Stroke Vertical PZT Microactuator with High-Speed Rotational Scanning,**” *Journal of Microelectromechanical System*, 2013.

Refereed Conference Proceedings

- C.-H. Rhee, Z. Qiu, **J. Choi**, T. Wang, K. Oldham, “**Dynamics of Thin-film Piezoelectric Vertical-Rotational Scanning Actuator,**” *Proceedings of the 2015 International Design Engineering Technical Conferences & Computers and Information in Engineering Conference*, 2015.
- M. Shin, **J. Choi**, C. Kao, K. Oldham, “**Micro-robotic Actuation Units Based On Thin-film Piezoelectric and High-aspect Ratio Polymer Structures,**” *Proceedings of the 2014 International Design Engineering Technical Conferences & Computers and Information in Engineering Conference*, 2014.
- Z. Qiu, C.-H. Rhee, **J. Choi**, T. Wang, K. Oldham, “**Thin-film PZT Based Monolithic Translational/Tilt Micro-scanner For Vertical Cross-sectional Imaging With Dual Axes Confocal Endomicroscope,**” *Digest of the Solid-State Sensors, Actuators and Microsystems Workshop*, 2014.
- **J. Choi**, C.-H. Rhee, Z. Qiu, T. Wang, K. Oldham, “**Static and Dynamic Modeling of a Multi-Axis Thin-Film Piezoelectric Micro-Actuator,**” *Proceedings of ASME 2013 Dynamic Systems and Control Conference*, 2013.

5. 3. Future Work

Residual stress was found to be a main source that causes asymmetry in the sample devices and generates unwanted motion. However, residual stress was not characterized. It would be helpful

to keep track of the residual stress throughout the fabrication process. The residual stress appears to vary both in the x- and y-axis directions. However, some residual stress measurements tools provide only average values in one or two directions, and it is difficult to obtain an accurate measurement on patterned films. Test structures composed of different combinations of films can be placed in various locations in wafers for the measurements. If any film or step is found to significantly contribute to the residual stress, design optimization using the models developed in this work can be performed to further reduce actuator sensitivity to processing variation.

Similar test structures for measuring material properties such as Young's modulus of films can be also added to obtain more accurate models. Cantilevers made of different materials and in different lengths can be excited to find their resonant frequencies, and material properties can be back calculated. Or one can perform a static bending tests on the test cantilevers using atomic force microscopy.

As reported, a good number of parylene/aluminum jumpers were found to be defective after the release, although almost all were confirmed to be working right after they were completed. The jumpers could be sealed with another layer of parylene right after they are completed. Short etching before deposition to roughen the surface might improve adhesion. These add more steps to the fabrication, but reliable jumpers can increase the device yield and ease the assembly steps.

Due to the unavailability of multiple input channels for the PZT actuator in the imaging system, differential operation with the calibrated model of Chapter 4.1 was not performed during the imaging tests. When the imaging system is expanded to take more input channels, open loop operation with multiple inputs can be performed, but for more robustness feedback control systems can be implemented using embedded sensing elements or optical image features or both, which can compensate for disturbances and changes in actuator behavior over time. The sensors can be integrated along the bending legs, only using a small footprint as shown in Figures 5.1 and 5.2. Two types of on-chip sensors are proposed. One is using platinum for piezoresistive sensing (Figure 5.1), and the other is using PZT for piezoelectric sensing (Figure 5.2).

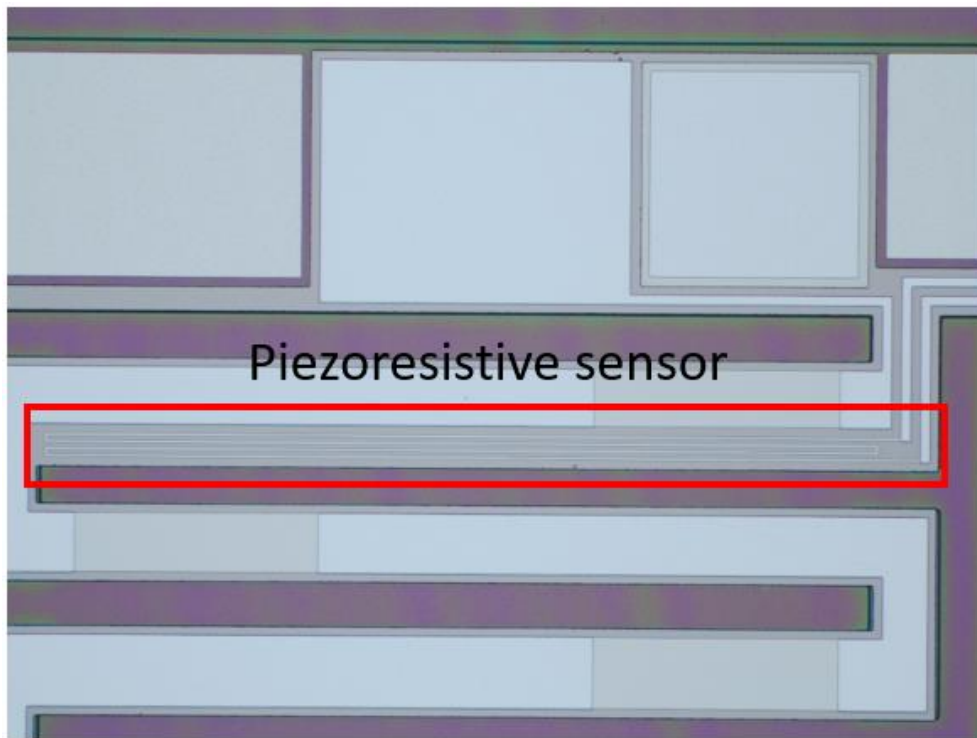


Figure 5.1. Microscope image of embedded piezoresistive sensing element

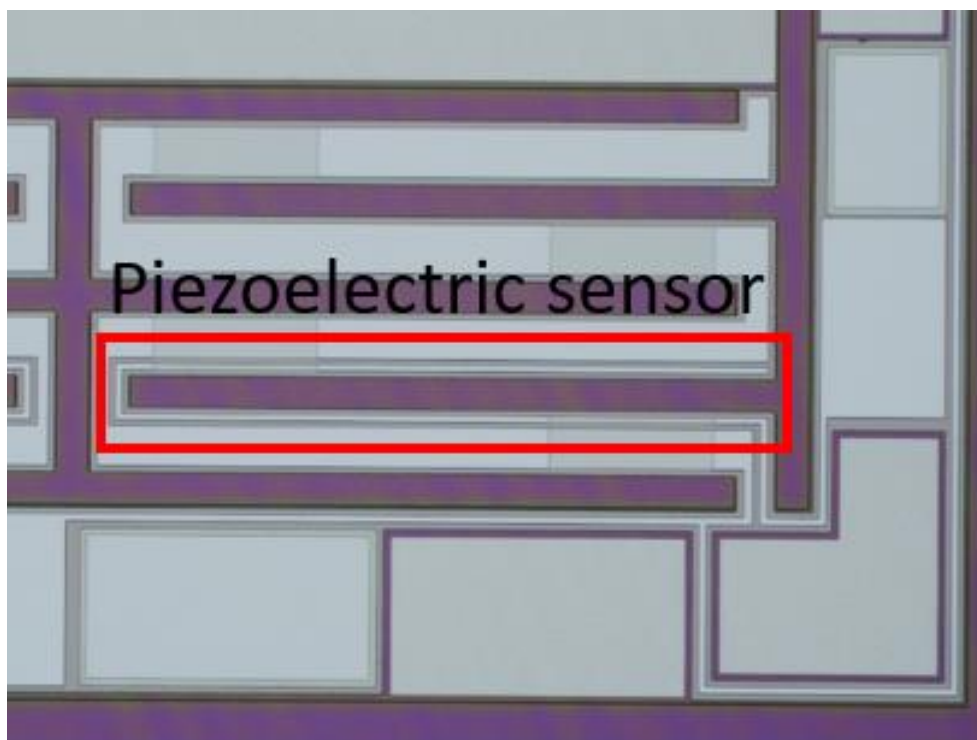


Figure 5.2. Microscope image of on-chip piezoelectric sensing element

For early diagnosis of cancers in the digestive tract, *in vivo* vertical cross-sectional imaging needs to be achieved. However, packaging all optical components and MEMS scanners in a millimeter scale catheter is very challenging. Thus, it is very helpful to first develop a slightly larger system as the next step to develop assembly and alignment procedures before further miniaturization. Attempts were made to integrate the prototype actuators into a handheld dual axes confocal imaging system with a 10-mm outer-diameter scan head (Figure 5.3) that uses the optical components and vertical micro-scanner fitting a 5mm scanning probe. Although one probe was successfully assembled and the beam was tested as shown in Figure 5.3 (c), due to the actuator reliability issue, imaging was not performed. Suggestions in this section can be useful in providing more robust scanners in more quantity to support the continual effort to develop vertical sectioning capable endoscopic tools for detection of mucosal diseases.

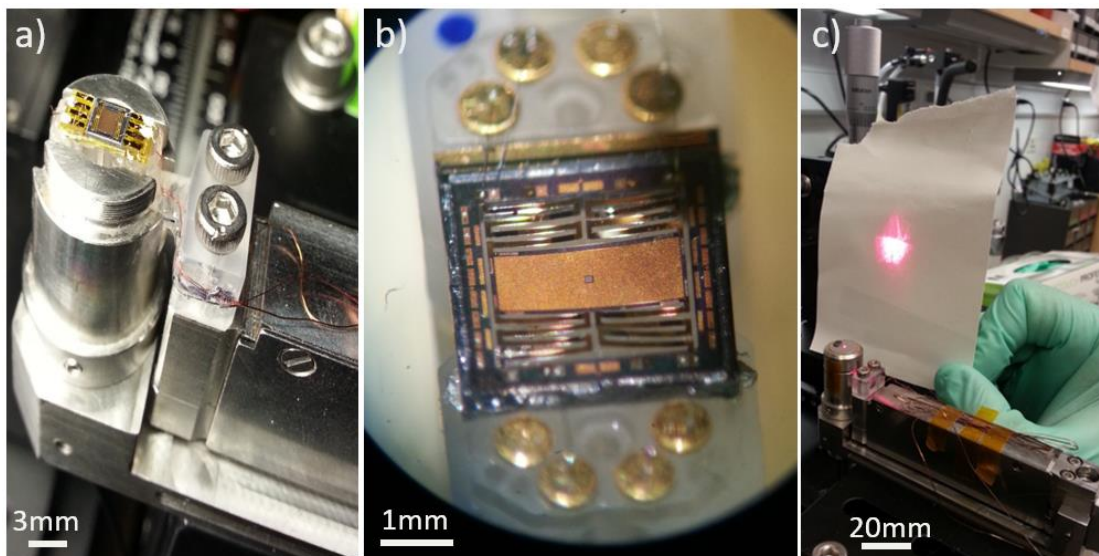


Figure 5.3. Scanner integration into handheld dual axes confocal instrument: (a) before closed with a cap with objective lens; (b) zoomed in microscope picture of integrated scanner; (c) beam test with assembled instrument

APPENDICES

Appendix A: Nominal Model

A. 1. Displacement of Single Beam

Obtained using beam theory, Eq. (3.6) describes the displacements of a single beam in three direction. The $\tilde{\mathbf{S}}$ matrices represent compliance for external and internal loading. $\tilde{\mathbf{P}}$ and $\tilde{\mathbf{R}}$ matrices map initial deflection and effective residual moments to the tip displacements, respectively.

$$\tilde{\mathbf{S}}_{ext} := \begin{bmatrix} \frac{L_{UP} + L_{DN}}{(GJ)_{comp}} & 0 & 0 \\ 0 & \frac{L_{UP}}{(EI)_{UP}} + \frac{L_{DN}}{(EI)_{DN}} & \frac{L_{UP}}{2(EI)_{UP}}(L_{UP} + 2L_{DN}) + \frac{L_{DN}^2}{2(EI)_{DN}} \\ 0 & \frac{L_{UP}}{(EI)_{UP}}\left(\frac{L_{UP}}{2} + L_{DN}\right) + \frac{L_{DN}^2}{2(EI)_{DN}} & \frac{L_{UP}}{(EI)_{UP}}\left(\frac{1}{3}L_{UP}^2 + L_{DN}^2 + L_{UP}L_{DN}\right) + \frac{L_{DN}^3}{3(EI)_{DN}} \end{bmatrix}$$

$$\tilde{\mathbf{S}}_{int} := \begin{bmatrix} 0 \\ \frac{L_{UP}}{(EI)_{UP}}M_{coef,UP} - \frac{L_{DN}}{(EI)_{DN}}M_{coef,DN} \\ \frac{L_{UP}}{(EI)_{UP}}\left(\frac{L_{UP}}{2} + L_{DN}\right)M_{coef,UP} + \frac{L_{DN}^2}{2(EI)_{DN}}(-M_{coef,DN}) \end{bmatrix}$$

$$\tilde{P} := \begin{bmatrix} 1 & 0 & 0 \\ 0 & 1 & 0 \\ 0 & L_{UP} + L_{DN} & 1 \end{bmatrix}, \quad \tilde{R} := \begin{bmatrix} 0 & 0 \\ \frac{L_{UP}}{(EI)_{UP}} & \frac{L_{DN}}{(EI)_{DN}} \\ \frac{L_{UP}}{(EI)_{UP}} \left(\frac{L_{UP}}{2} + L_{DN} \right) & \frac{L_{DN}^2}{2(EI)_{DN}} \end{bmatrix}$$

Where $(EI)_{UP}$ and $(EI)_{DN}$ are flexural rigidities of the upward bending segment and the downward bending segment, respectively.

A. 2. Displacement of Leg

Displacements of four beams are combined to describe that of a single leg (Eq. 3.7), with S_{ext} and S_{int} matrices defining beam compliance, I matrices the effects of initial deflections, and S matrices the directionality of the tip forces. \tilde{S}_{ext} , \tilde{S}_{int} , \tilde{P} , \tilde{R} matrices are defined as before.

$$S_{ext} := \tilde{S}_{ext} + I_2 S_{1t} + I_{1t} I_2^2 S_{2t} + I_{1t} I_2 \tilde{S}_{ext} S_\gamma + I_{1t} I_2^3 I_{2t} S_{1t} + I_{1t} I_2^2 I_{2t} \tilde{S}_{ext} S_\beta + I_{1t}^2 I_2^3 I_{2t} \tilde{S}_{ext} S_\alpha$$

$$S_{int} := I_{2t} \tilde{S}_{int} I_{1t}^2 I_2^3 + I_{2t} \tilde{S}_{int} I_{1t} I_2^2 + \tilde{S}_{int} I_{1t} I_2 + \tilde{S}_{int}$$

$$S_{1t} := \begin{bmatrix} 0 & 0 & 0 \\ 0 & \frac{-L_t}{(GJ)_{t,comp}} & \frac{-LL_t}{(GJ)_{t,comp}} \\ 0 & 0 & 0 \end{bmatrix}, S_{2t} := \begin{bmatrix} 0 & 0 & 0 \\ 0 & \frac{L_t}{(GJ)_{t,comp}} & 0 \\ 0 & 0 & 0 \end{bmatrix}$$

$$I_2 := \begin{bmatrix} -1 & 0 & 0 \\ 0 & -1 & 0 \\ 0 & -L & 1 \end{bmatrix}, I_{1t} := \begin{bmatrix} 1 & 0 & 0 \\ 0 & 1 & 0 \\ (-1)^n L_t & 0 & 1 \end{bmatrix}, I_{2t} := \begin{bmatrix} 1 & 0 & 0 \\ 0 & 1 & 0 \\ (-1)^{n+1} L_t & 0 & 1 \end{bmatrix}$$

$$S_\alpha := \begin{bmatrix} -1 & 0 & (-1)^n 3L_t \\ 0 & -1 & -L \\ 0 & 0 & 1 \end{bmatrix}, S_\beta := \begin{bmatrix} 1 & 0 & (-1)^{n+1} 2L_t \\ 0 & 1 & 0 \\ 0 & 0 & 1 \end{bmatrix}, S_\gamma := \begin{bmatrix} -1 & 0 & (-1)^n L_t \\ 0 & -1 & -L \\ 0 & 0 & 1 \end{bmatrix}$$

$n=1$ for legs A and D, $n=2$ for legs B and C.

$L=L_{UP}+L_{DN}$; L_t is the length of the torsional beam.

Appendix B: Perturbed Model

B. 1. Displacement of Leg

Similar to Eq. (2.8), Eq. (3.1) expresses the displacements of a single leg, but it describes a case where all the beams have different structural dimensions. Each matrix is defined as follows.

$$\psi_{ext}^i := \tilde{S}_{ext,4}^i + I_4^i S_{3t}^i + I_4^i I_{3t}^i \tilde{S}_{ext,3}^i S_{\gamma}^i + I_4^i I_{3t}^i I_{3t}^i S_{2t}^i + I_4^i I_{3t}^i I_{3t}^i I_{2t}^i \tilde{S}_{ext,2}^i S_{\beta}^i + I_4^i I_{3t}^i I_{3t}^i I_{2t}^i I_{2t}^i I_{1t}^i \tilde{S}_{ext,1}^i S_{\alpha}^i + I_4^i I_{3t}^i I_{3t}^i I_{2t}^i S_{1t}^i$$

$$\psi_{int}^i := \tilde{S}_{int,4}^i + I_4^i I_{3t}^i \tilde{S}_{int,3}^i + I_4^i I_{3t}^i I_{3t}^i I_{2t}^i \tilde{S}_{int,2}^i + I_4^i I_{3t}^i I_{2t}^i I_{2t}^i I_{1t}^i \tilde{S}_{int,1}^i$$

$$\tilde{S}_{ext,j}^i := \begin{bmatrix} \frac{L_{UPj}^i + L_{DNj}^i}{(GJ)_{comp}} & 0 & 0 \\ 0 & \tilde{S}_{ext,j}^i(2,2) & \tilde{S}_{ext,j}^i(2,3) \\ 0 & \tilde{S}_{ext,j}^i(3,2) & \tilde{S}_{ext,j}^i(3,3) \end{bmatrix}$$

$$\tilde{S}_{ext,j}^i(2,2) = \frac{L_{UPj}^i}{(EI)_{UPj}^i} + \frac{L_{DNj}^i}{(EI)_{DNj}^i}$$

$$\tilde{S}_{ext,j}^i(2,3) = \frac{L_{UPj}^i}{2(EI)_{UPj}^i} (L_{UPj}^i + 2L_{DNj}^i) + \frac{(L_{DNj}^i)^2}{2(EI)_{DNj}^i}$$

$$\tilde{S}_{ext,j}^i(3,2) = \frac{L_{UPj}^i}{(EI)_{UPj}^i} \left(\frac{L_{UPj}^i}{2} + L_{DNj}^i \right) + \frac{(L_{DNj}^i)^2}{2(EI)_{DNj}^i}$$

$$\tilde{S}_{ext,j}^i(3,3) = \frac{L_{UPj}^i}{(EI)_{UPj}^i} \left(\frac{1}{3} (L_{UPj}^i)^2 + (L_{DNj}^i)^2 + L_{UPj}^i L_{DNj}^i \right) + \frac{(L_{DNj}^i)^3}{3(EI)_{DNj}^i}$$

$$I_j^i := \begin{bmatrix} -1 & 0 & 0 \\ 0 & -1 & 0 \\ 0 & -L_j^i & 1 \end{bmatrix} \quad (i=A,B,C,D \text{ and } j=2,3,4)$$

$$S_{1t}^i := \begin{bmatrix} 0 & 0 & 0 \\ 0 & \frac{-L_{t1}^i}{(GJ)_{t,comp}} & \frac{-(L_4^i - L_3^i + L_2^i)L_{t1}^i}{(GJ)_{t,comp}} \\ 0 & 0 & 0 \end{bmatrix}$$

$$S_{2t}^i := \begin{bmatrix} 0 & 0 & 0 \\ 0 & \frac{L_{t2}^i}{(GJ)_{t,comp}} & \frac{L_{t2}^i(L_4^i - L_3^i)}{(GJ)_{t,comp}} \\ 0 & 0 & 0 \end{bmatrix}, S_{3t}^i := \begin{bmatrix} 0 & 0 & 0 \\ 0 & \frac{-L_{t3}^i}{(GJ)_{t,comp}} & \frac{-L_4^i L_{t3}^i}{(GJ)_{t,comp}} \\ 0 & 0 & 0 \end{bmatrix}$$

$$I_{1t}^i := \begin{bmatrix} 1 & 0 & 0 \\ 0 & 1 & 0 \\ (-1)^n L_{t1}^i & 0 & 1 \end{bmatrix}, I_{2t}^i := \begin{bmatrix} 1 & 0 & 0 \\ 0 & 1 & 0 \\ (-1)^{n+1} L_{t2}^i & 0 & 1 \end{bmatrix}$$

$$I_{3t}^i := \begin{bmatrix} 1 & 0 & 0 \\ 0 & 1 & 0 \\ (-1)^n L_{t3}^i & 0 & 1 \end{bmatrix}, S_{\alpha}^i := \begin{bmatrix} -1 & 0 & (-1)^n(L_{t1}^i + L_{t2}^i + L_{t3}^i) \\ 0 & -1 & -(L_4^i - L_3^i + L_2^i) \\ 0 & 0 & 1 \end{bmatrix}$$

$$S_{\beta}^i := \begin{bmatrix} 1 & 0 & (-1)^{n+1}(L_{3t}^i + L_{2t}^i) \\ 0 & 1 & (L_4^i - L_3^i) \\ 0 & 0 & 1 \end{bmatrix}, S_{\gamma}^i := \begin{bmatrix} -1 & 0 & (-1)^n L_{t3}^i \\ 0 & -1 & -L_4^i \\ 0 & 0 & 1 \end{bmatrix}$$

$$L_j^i = L_{UPj}^i + L_{DNj}^i \quad (i=A, B, C, D \text{ and } j=1, 2, 3, 4)$$

n=1 for legs A and D, n=2 for legs B and C.